

Chapter 5

5 DEMONSTRATION OF THE OPTIMUM EXECUTION OF REPRESENTATIVE PRESCRIBED MACHINING PATHS

5.1 Introduction

In this chapter, optimum platform geometries of the re-configurable planar Gough-Stewart platform test-model are determined for different prescribed machining tasks.

The determination of the optimum platform geometries is done using the *simulation-based* optimization methodology developed in **Chapter 4**. The feasibility of this approach was illustrated in **Chapter 4** by optimizing the geometry of a *hypothetical* planar Gough-Stewart platform for a simple straight-line prescribed path, taking into consideration the mechanism's configurational constraints. In applying the methodology to a *physically real* platform, however, the physical operational constraints specified in Section D.3 are required to prevent mechanical interference. The respective masses and moments of inertia of the seven bodies comprising the physical test-model are also determined in **Appendix D** (Section D.2.3). These seven bodies are numbered below in Figure 5.1 which corresponds to Figure 2.5 and Figure D.2.

5.4.4 Execution of the circular tool path

The series of photographs shown in Figure 5.18 is of different instants during the execution of the first revolution of the circular tool path.

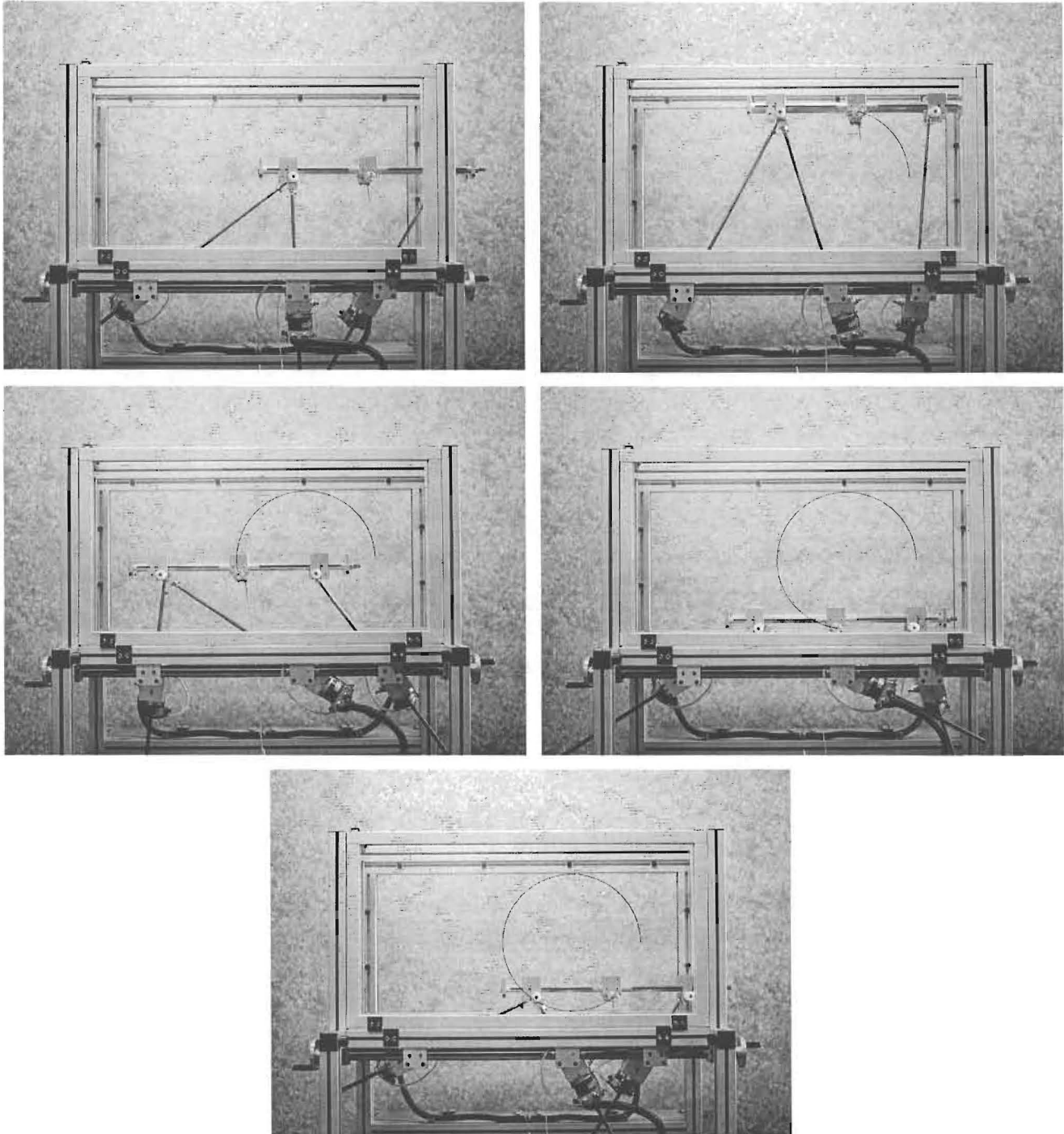


Figure 5.18: Execution of the circular tool path.

Figure 5.19 is a close-up of the traced circular tool path, showing that the diameter of the traced circle is approximately 350 mm (35 cm), and that the circle is smoothly traced.

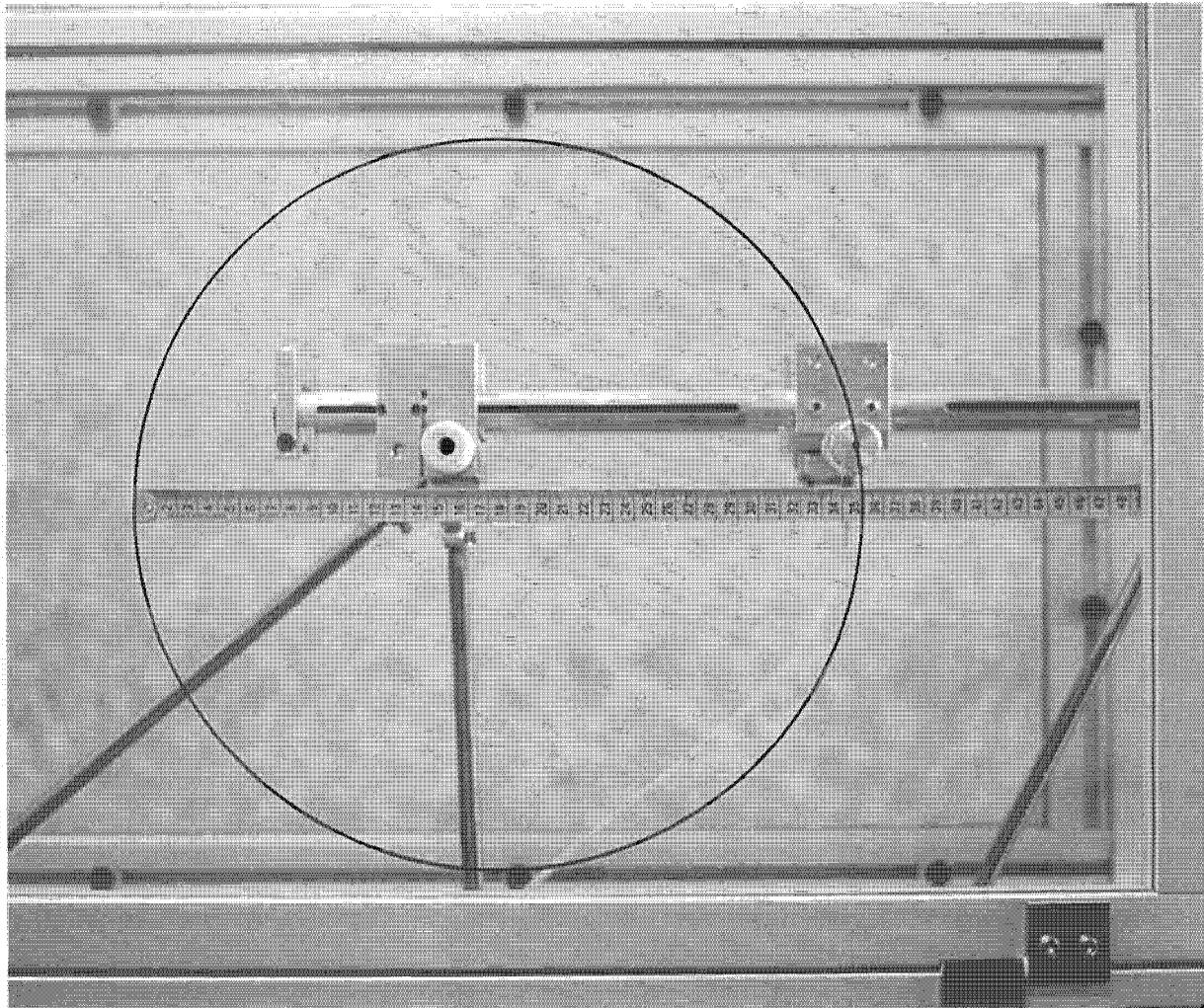


Figure 5.19: Close-up view of the executed circular tool path.

5.5 Spiral tool path

5.5.1 Nodal points and orientation angle

The spiral tool path is a scaled version of the logarithmic spiral test curve $\rho = e^{0.1\theta}$ of Section 3.5.4. Using a scale factor of 0.285, the 79 spiral tool path nodal points are as shown in Figure 5.20.

The motion time along the spiral tool path is 93.24 seconds with the specification of $\ddot{s}_{\text{ALLOW}} = 0.01 \text{ m/s}^2$, $v^* = 1.0 \text{ m/min}$ and $n_{\text{time}} = 5$ for the use of the OCAS trajectory-planning algorithm.

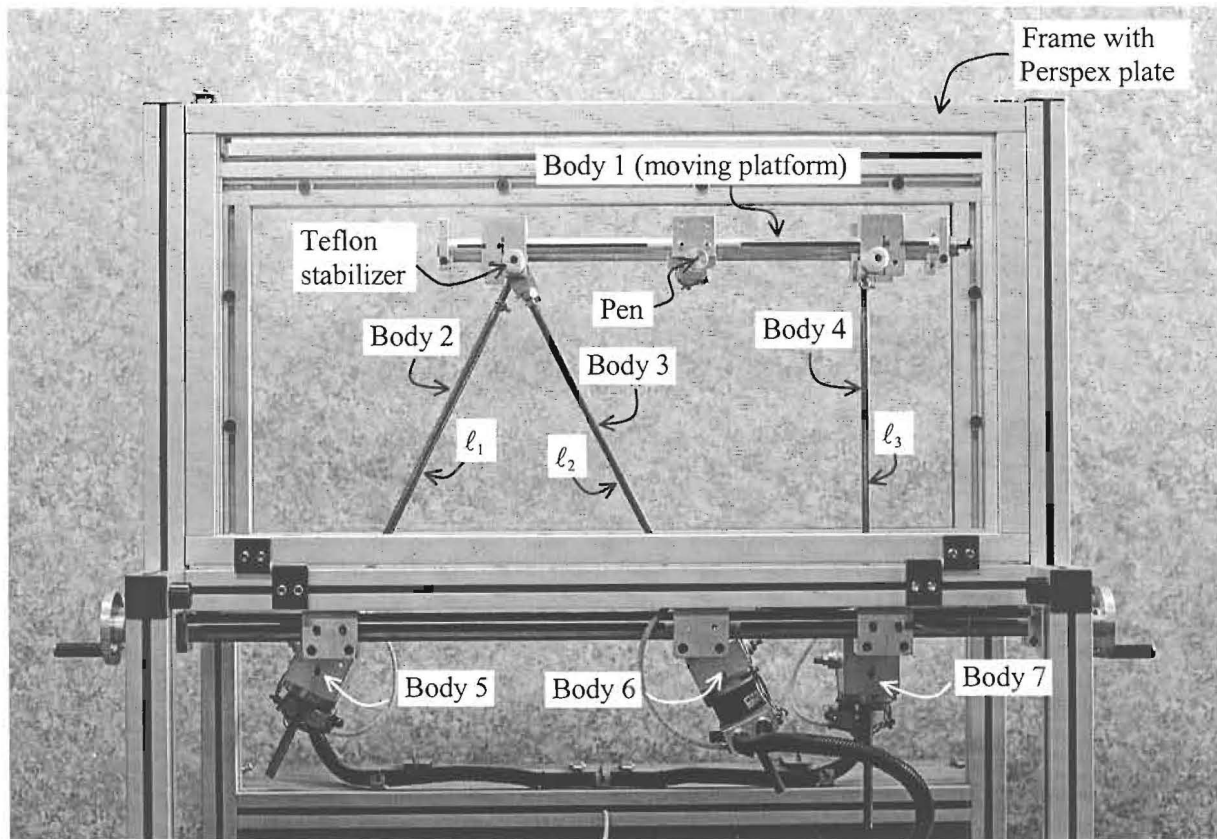


Figure 5.1: Photograph of the physical planar Gough-Stewart platform test-model.

The moving platform is in contact with the Perspex side panels via the Teflon stabilizers and the pen shown in Figure 5.1. Section D.2.3 shows how the resulting *frictional* force was experimentally determined. This external frictional force represents the *cutting force* incorporated in the kinematic and kinetic model of the planar Gough-Stewart machining platform. In fact, the test-model is used here to demonstrate the “fixed workpiece scenario” (see Sections 2.4.1 and 2.6.4.2.1), with specifically a *zero tool length* ($\eta_1^p = 0$), since the pen is mounted to coincide with the *assumed* center of mass of the moving platform.

Furthermore, in this chapter, non-trivial prescribed paths are specified for the physical test-model using the OCAS trajectory-planning technique described in **Chapter 3**. The five different test functions discussed in Section 3.5 are used as prescribed tool paths, to illustrate the application of the proposed optimization methodology to obtain optimum operational geometries.

Once the *simulation-based* numerical optimization of the physical test-model is done for each prescribed path, the *execution* of each path follows through the control commands generated by the computer simulation for controlling the required variation of the actuator leg lengths. These lengths are found by solving the three closed-form inverse kinematic equations relating the position and orientation of the moving platform to the actuator leg lengths. The position and orientation of the moving platform follows

directly from the prescribed trajectory, and hence the required actuator leg lengths may easily be determined (see expression (4.10)).

Since the purpose of the test-model is only to demonstrate the new technology, visual inspection is used to verify that each executed path indeed corresponds to the prescribed path. Photographs are included in this chapter to show the successful execution of the prescribed paths, for the respective optimum and feasible settings of the planar machine.

Sections 5.2 – 5.6 respectively deal with the five different prescribed paths all of which are scaled for *continuous* execution. Section 5.7 shows how the proposed optimization methodology may be applied in the *piece-wise* execution of the “bigger parabolic tool path”.

5.2 Parabolic tool path

5.2.1 Nodal points and orientation angle

The parabolic test function used in Section 3.5.1, $y(x) = \frac{x^2}{2}$, was approximated over the x -interval, $x \in [-2, 2]$, using 29 nodal points as shown in Figure 3.16. Here a *scaled mirror image* of this quadratic function is used as prescribed path. The *mirror image* of the original parabola (expression (3.66)) is given by

$$y(x) = -\frac{x^2}{2} \quad (5.1)$$

over the x -interval, $x \in [-2, 2]$. Substituting the *unscaled* x -values into (5.1) gives the *unscaled* y -values. The scale factor used here is 0.075, and the resulting 27 nodal points are shown in Figure 5.2.

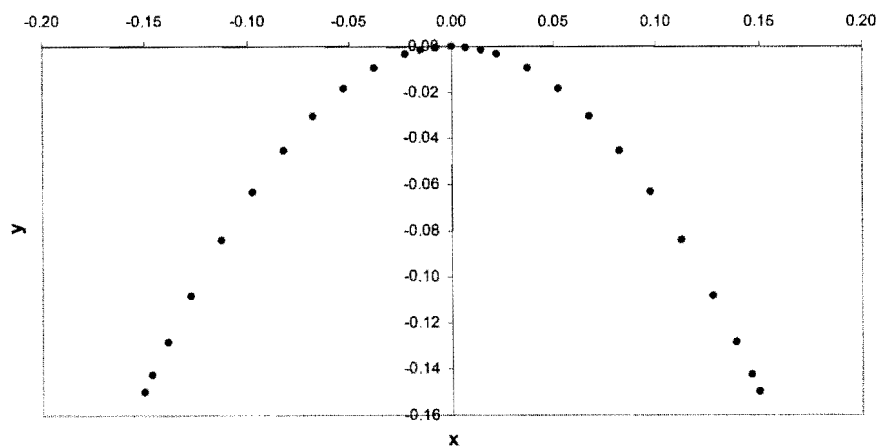


Figure 5.2: Nodal points used to approximate the parabolic tool path.

For the OCAS trajectory-planning methodology (**Chapter 3**), the maximum allowable acceleration is limited to 0.01 meter per second square ($\ddot{s}_{\text{allow}} = 0.01 \text{ m/s}^2$), and a cutting speed of 1.0 m/min ($v^* = 1.0 \text{ m/min}$) is specified. With these specifications, the *simulated* prescribed motion is completed in 29.46 s. The simulation is furthermore carried out with the number of additional intermediate time instants, $n_{\text{time}} = 5$ (see **Appendix B**).

It is also required that the moving platform of the test-model be tangentially orientated with respect to the prescribed curve. With this specification the moving platform orientation angle varies from 63.43° at the starting point $(-0.15, -0.15)$, to -63.43° at the end point $(0.15, -0.15)$ (see **Figure 5.3**).

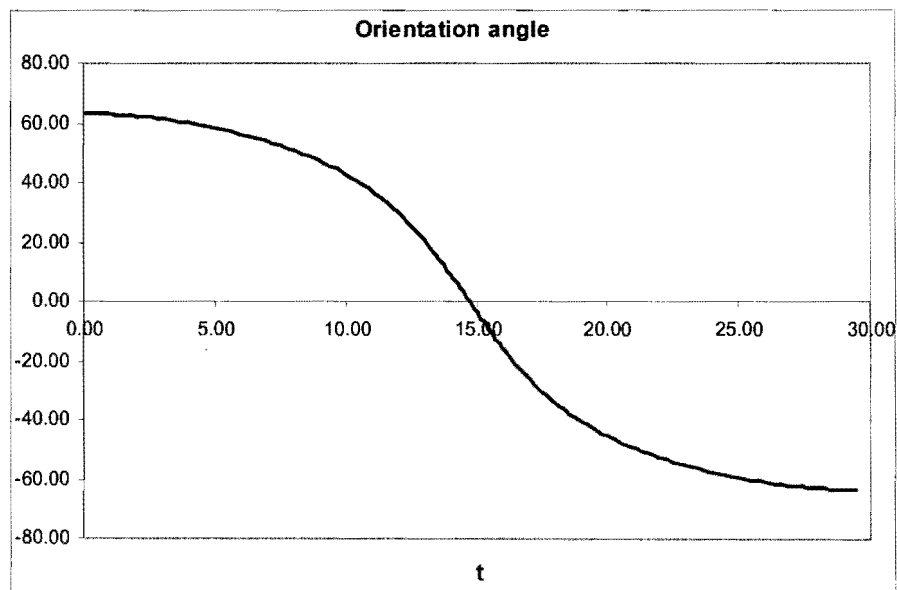


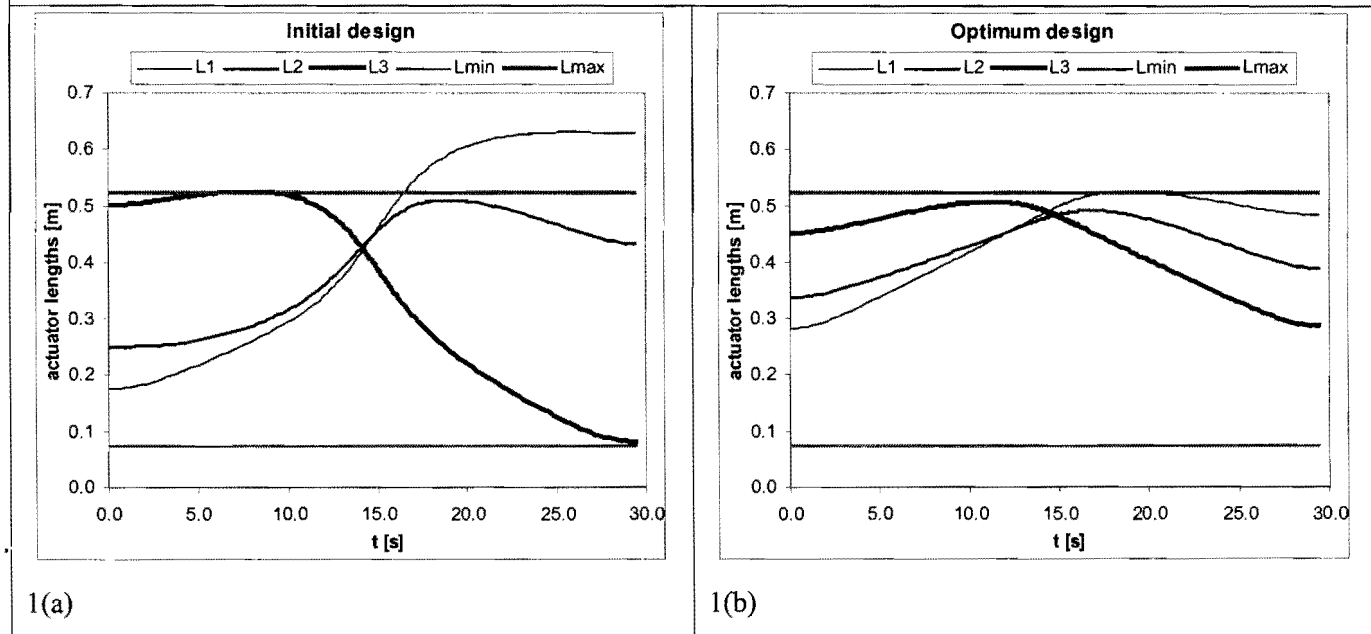
Figure 5.3: Variation in the orientation angle for the parabolic tool path.

5.2.2 Optimization results

A comparison between the initial test-model design and optimum test-model design for the parabolic prescribed tool path is given in **Table 5.1**, with figure insets 1(a) – 1(d).

Initial design		Optimum design	
$\mathbf{X}^0 = [0.4, 0.4, -0.4, -0.4, 0.2]^T$		$\mathbf{X}^* = [0.1, 0.19387, -0.47769, -0.18012, 0.113]^T$	
Inequality constraint values (see Section D.3):			
$C_1(\mathbf{X}^0) = -0.05$	$C_2(\mathbf{X}^0) = -0.3$	$C_1(\mathbf{X}^*) = -0.35$	$\Rightarrow C_2(\mathbf{X}^*) = -0.363 \times 10^{-6}$
$C_3(\mathbf{X}^0) = -0.065$	$C_4(\mathbf{X}^0) = -0.287$	$C_3(\mathbf{X}^*) = -0.27113$	$C_4(\mathbf{X}^*) = -0.08087$
$C_5(\mathbf{X}^0) = -0.07$	$C_6(\mathbf{X}^0) = -0.087$	$C_5(\mathbf{X}^*) = -0.157$	$\Rightarrow C_6(\mathbf{X}^*) = 0.624 \times 10^{-6}$
$\rightarrow C_7(\mathbf{X}^0) = 0.10533$	$C_8(\mathbf{X}^0) = -0.01481$	$\Rightarrow C_7(\mathbf{X}^*) = -0.784 \times 10^{-6}$	$C_8(\mathbf{X}^*) = -0.03374$
$\rightarrow C_9(\mathbf{X}^0) = 0.00045$	$\rightarrow C_{10}(\mathbf{X}^0) = 0.07769$	$C_9(\mathbf{X}^*) = -0.01780$	$\Rightarrow C_{10}(\mathbf{X}^*) = -0.616 \times 10^{-6}$
$\rightarrow C_{11}(\mathbf{X}^0) = 0.07769$	$C_{12}(\mathbf{X}^0) = -0.34542$	$\Rightarrow C_{11}(\mathbf{X}^*) = -0.616 \times 10^{-6}$	$C_{12}(\mathbf{X}^*) = -0.39888$
$C_{13}(\mathbf{X}^0) = -0.14542$	$\rightarrow C_{14}(\mathbf{X}^0) = 0.00109$	$C_{13}(\mathbf{X}^*) = -0.22639$	$C_{14}(\mathbf{X}^*) = -0.04907$
$C_{15}(\mathbf{X}^0) = -0.00493$	$\rightarrow C_{16}(\mathbf{X}^0) = 0.01619$	$C_{15}(\mathbf{X}^*) = -0.22745$	$C_{16}(\mathbf{X}^*) = -0.05909$
$\rightarrow C_{17}(\mathbf{X}^0) = 0.01727$	$\rightarrow C_{18}(\mathbf{X}^0) = 0.04250$	$C_{17}(\mathbf{X}^*) = -0.01676$	$C_{18}(\mathbf{X}^*) = -0.05310$
$C_{19}(\mathbf{X}^0) = -0.06220$	$C_{20}(\mathbf{X}^0) = -0.08449$	$C_{19}(\mathbf{X}^*) = -0.05754$	$C_{20}(\mathbf{X}^*) = -0.15073$
$C_{21}(\mathbf{X}^0) = -0.07149$	$\rightarrow C_{22}(\mathbf{X}^0) = 0.03098$	$C_{21}(\mathbf{X}^*) = -0.05200$	$C_{22}(\mathbf{X}^*) = -0.11672$
\rightarrow constraint violation		\Rightarrow constraint active	

Variation of actuator leg lengths along the parabolic tool path:



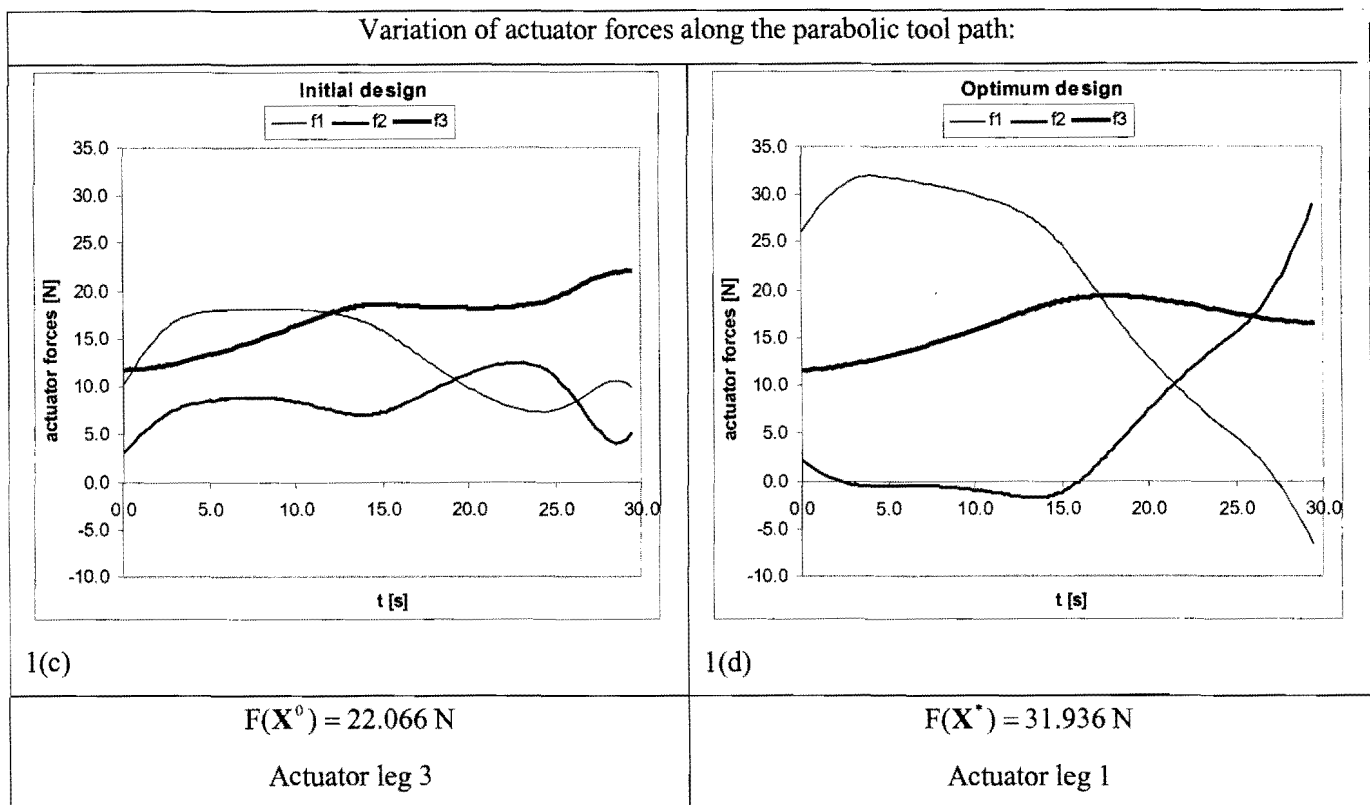


Table 5.1: Comparison between the initial and optimum designs for the parabolic tool path.

Although the initial objective function value $F(\mathbf{X}^0) = 22.066 \text{ N}$ is lower than the optimum objective function value $F(\mathbf{X}^*) = 31.936 \text{ N}$, the *initial design is infeasible*. In fact, nine of the 22 inequality constraints are *violated* when the parabolic test function is traced with the initial design \mathbf{X}^0 . Table 5.1 lists the initial values of the inequality constraint functions $C_i(\mathbf{X}^0)$, $i = 1, 2, 3, \dots, 22$, as well as their optimum values $C_i(\mathbf{X}^*)$, $i = 1, 2, 3, \dots, 22$. The violated inequality constraints associated with the initial design \mathbf{X}^0 have function values greater than zero, and are indicated by a *single arrow* \rightarrow in Table 5.1. Similarly, the *active* inequality constraints associated with the optimum design \mathbf{X}^* have *approximately* zero function values, and are indicated by a *double arrow* \Rightarrow in Table 5.1.

The variation in the actuator leg lengths depicted in figure inset 1(a) clearly show that both actuator legs ℓ_1 and ℓ_3 initially violate the allowable maximum leg length, explaining the positive constraint function values of C_7 and C_9 (expression (D.11)). Inequality constraints corresponding to C_{10} and C_{11} (expression (D.12)) are violated even though the allowable minimum leg length is not violated (see figure inset 1(a)). Indeed, these two inequality constraints are violated as a result of the specification of tangential orientation of the moving platform with respect to the parabolic tool path (see Figure 5.3). The remaining violated inequality constraints, corresponding to the positive function values of C_{14} , C_{16} ,

C_{17} , C_{18} and C_{22} , indicate that the parabolic tool path cannot be followed with the initial design \mathbf{X}^0 , due to mechanical interference (see respective expressions (D.15), (D.17), (D.18), (D.19) and (D.23)).

On the other hand, figure inset 1(b) clearly shows that for the optimum design \mathbf{X}^* , the variation in actuator leg lengths as the parabolic tool path is followed, lies within the minimum and maximum allowable lengths. The *feasibility* of the optimum design \mathbf{X}^* is further borne out by the fact that the optimum inequality constraint function values $C_i(\mathbf{X}^*)$, $i = 1, 2, 3, \dots, 22$ are all less than, or approximately equal to zero. In particular, the inequality constraints corresponding to C_2 , C_6 , C_7 , C_{10} and C_{11} are considered to be *active* (see expressions (D.10), (D.11) and (D.12)). The optimum solution is found after 227 optimization iterations and utilizing 6 minutes and 58 seconds computational time on a Pentium IV 1.5 GHz computer with 640 MB DDRAM. LFOPC terminated on criterion 2 ($\epsilon_x \leq 10^{-5}$) listed in Section 4.4.

5.2.3 Analysis of convergence to optimum

Figure 5.4 shows the convergence history of the objective function.

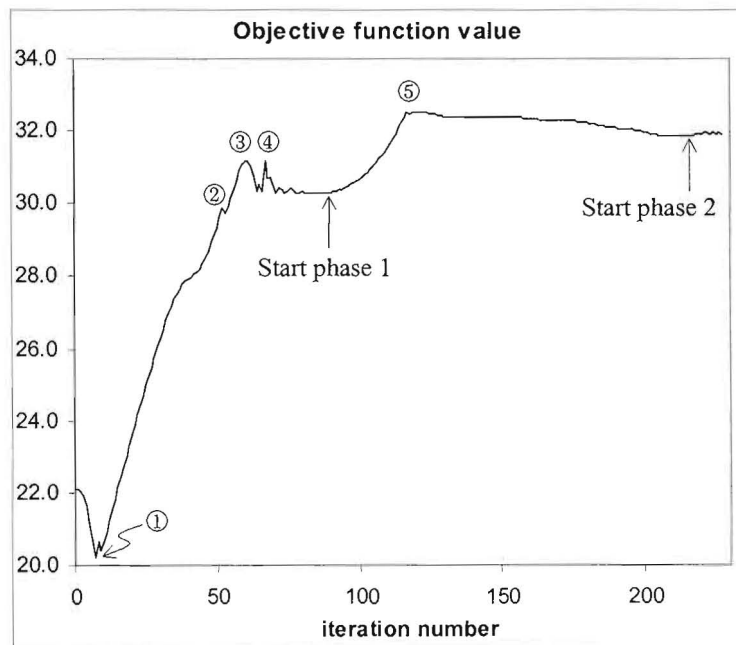


Figure 5.4: Convergence history of the objective function for the parabolic tool path.

The behavior of the above objective function vs. iteration number curve is of course dependent on the iterative search generated by the LFOPC algorithm in the five dimensional design space (see Figure 4.10). The choice of the initial design \mathbf{X}^0 obviously plays an important role in the nature of the convergence history of the objective function. In correspondence with Section 4.5, the initial configuration of the planar machining center is chosen as $\mathbf{X}^0 = [0.4, 0.4, -0.4, -0.4, 0.2]^T$ for all the

machining paths investigated in this chapter. Initial design variable values $X_1^0 = 0.4 \text{ m}$, $X_2^0 = 0.4 \text{ m}$ and $X_5^0 = 0.2 \text{ m}$ are in scaled agreement with the geometry of Haug et al.'s [73] planar Gough-Stewart platform. Setting design variables $X_4^0 = -0.4 \text{ m}$ and $X_3^0 = -0.4 \text{ m}$ corresponds to a random choice for the position of the origin of the global $0xy$ -coordinate system, relative to which the tool path is described, and the kinematic and kinetic analysis (**Chapter 2**) is done.

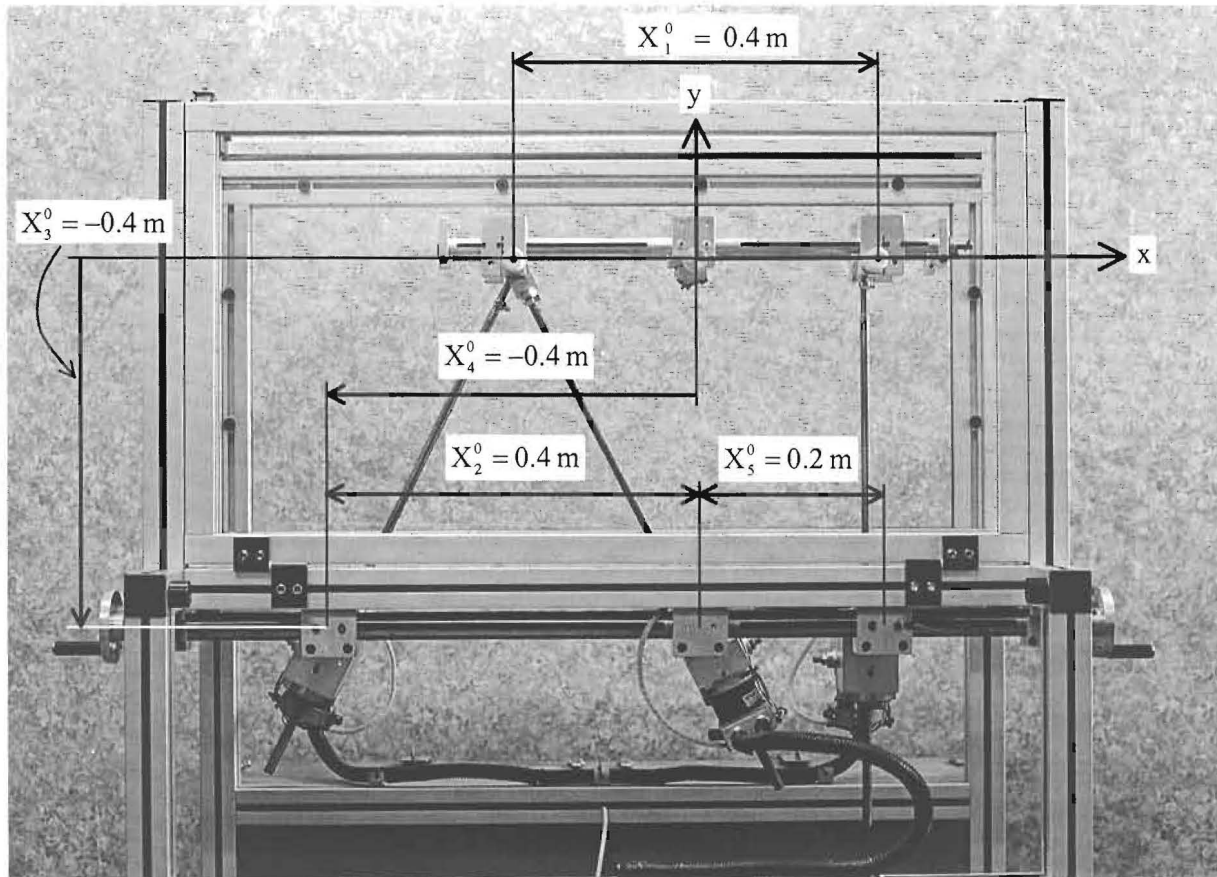


Figure 5.5: Photograph of the initial test-model design $X^0 = [0.4, 0.4, -0.4, -0.4, 0.2]^T$.

With specific reference to Figure 5.4, the labels ① – ⑤ are used in Table 5.2 to relate the *iteration number* and *phase* of the LFOPC-algorithm (see **Appendix C**) to the actuator leg responsible for the *maximum magnitude actuator force* (see Section 4.2.2) and the violated inequality constraints at the indicated regions of the convergence curve.

Labels	Iter. No.	LFOPC-Phase	Act. leg	Violated Inequality Constraints
X^0	0	0	l_3	C_7 C_9 C_{10} C_{11} C_{14} C_{16} C_{17} C_{18} C_{22}
①	7	0	l_3	C_7 C_8 C_9 C_{10} C_{11} C_{16} C_{18} C_{22}
	8	0	l_1	C_7 C_8 C_9 C_{10} C_{11} C_{18} C_{22}
	9	0	l_1	C_7 C_8 C_9 C_{10} C_{11} C_{16} C_{18} C_{22}
②	52	0	l_1	C_6 C_7 C_{10} C_{11} C_{17}
	53	0	l_1	C_6 C_7 C_{10} C_{11} C_{17}
	54	0	l_1	C_6 C_7 C_{10} C_{11} C_{17}
③	60	0	l_1	C_7 C_{10} C_{11}
	61	0	l_1	C_7 C_{10} C_{11}
④	63	0	l_1	C_7 C_{10} C_{11}
	64	0	l_2	C_7 C_{10} C_{11}
	65	0	l_1	C_7 C_{10} C_{11}
	66	0	l_1	C_7 C_{10} C_{11}
	67	0	l_2	C_7 C_{10} C_{11}
	68	0	l_2	C_7 C_{10} C_{11}
LFOPC phase-change	69	0	l_1	C_7 C_{10} C_{11}
	86	0	l_1	C_7 C_{10} C_{11}
	87	0	l_2	C_7 C_{10} C_{11} maximum violated constraint value $C_7(X^{87}) = 0.00496$
	87	1	l_2	C_7 C_{10} C_{11}
⑤	88	1	l_1	C_7 C_{10} C_{11}
	121	1	l_1	none
	122	1	l_1	none
LFOPC phase-change	123	1	l_1	C_2 C_7
	215	1	l_1	C_2 C_6 C_7 C_{10} C_{11}
LFOPC phase-change	215	2	l_1	C_2 C_6 C_7 C_{10} C_{11}
	X^*	227	2	l_1 C_2 C_6 C_7 C_{10} C_{11} (active)

Table 5.2: Comparative table for the parabolic tool path objective function vs. iteration number curve (see Figure 5.4).

The increase in the objective function value between labels ④ and ⑤ in Figure 5.4 is a result of the LFOPC phase-change occurring at iteration number 87 (see **Appendix C**) at which point the penalty parameter is increased. Furthermore, Table 5.2 shows that the actuator leg responsible for the maximum magnitude actuator force switches from actuator leg ℓ_3 to ℓ_1 at label ①. It was shown in Section 4.3.1 that a switch in the actuator legs responsible for the maximum magnitude actuator force is associated with a kink in the objective function, and hence a discontinuity in its slope. This results in the spiky behavior of the objective function in these regions.

The switches involving actuator legs ℓ_1 and ℓ_2 that occur as the LFOPC-algorithm changes from phase 0 to phase 1 show that the associated design is close to the optimum. Consider figure inset 1(d) showing the variation in actuator forces associated with the optimum design \mathbf{X}^* . The maximum magnitude of the force in actuator leg ℓ_1 , $f_1 = 31.936$ N occurring at time instant $t = 3.97$ s, is only slightly larger than the maximum magnitude of the force in actuator leg ℓ_2 , $f_2 = 28.774$ N occurring at time instant $t = 29.46$ s.

The fact that the final design of phase 0 (iteration number 87 in Table 5.2) is indeed relatively close with respect to feasibility to the optimum design, is evident from the convergence histories of the respective design variables X_i , $i = 1, 2, \dots, 5$ as shown in Figure 5.6. It is of interest to note that for the design variables the convergence is considerably smoother. In practical terms, convergence is effectively achieved at the end of phase 0 after only 87 iterations where the maximum violated constraint is C_7 with a function value of $C_7(\mathbf{X}^{87}) = 0.00496$ m = 4.96 mm.

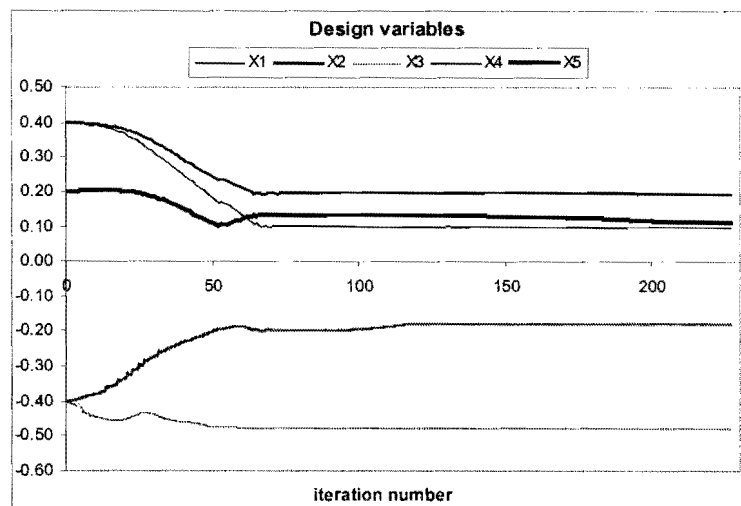


Figure 5.6: Convergence histories of design variables X_i , $i = 1, 2, \dots, 5$ for the parabolic tool path.

5.2.4 Execution of parabolic tool path

Figure 5.7 shows a series of photographs taken at different time instants as the parabolic tool path is traced. The tangential orientation of the moving platform along the curve is clearly visible from the photographs.

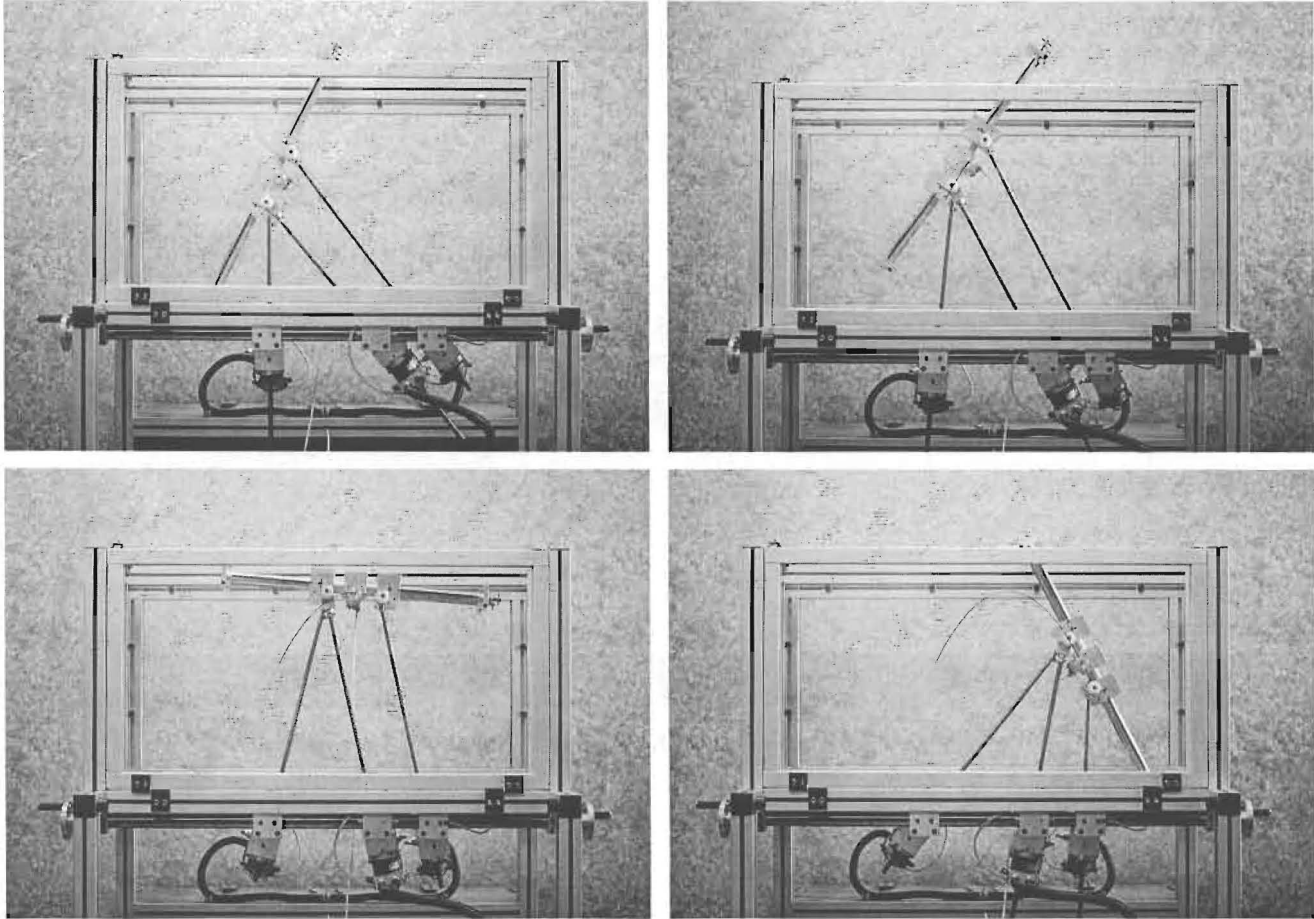


Figure 5.7: Execution of parabolic tool path.

A close-up view of the executed parabolic tool path is shown in Figure 5.8. Inspection shows that the actual executed tool path accurately resembles the prescribed tool path (see Figure 5.2). It is evident that the distance between the end points of the traced parabolic tool path is approximately 300 mm (30 cm) and that the traced parabolic tool path is proportionally shaped and smooth in agreement with the prescribed path specified by Figure 5.2.

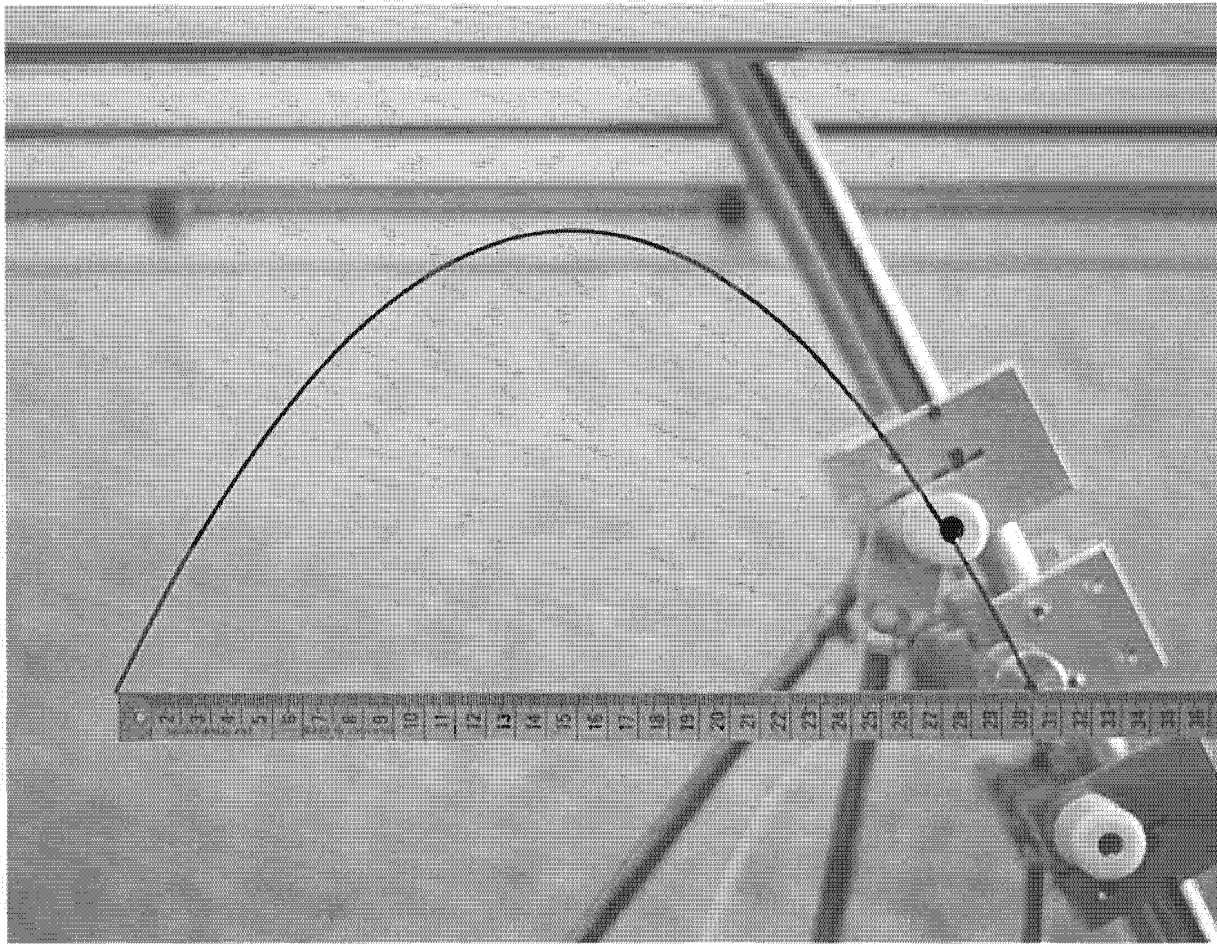


Figure 5.8: Close-up view of the executed parabolic tool path.

5.3 Spike tool path

5.3.1 Nodal points and orientation angle

The spike test function of Section 3.5.2, $y(x) = \frac{1}{1+x^2}$ (see expression 3.67) was approximated over the x -interval, $x \in [-2, 2]$, using 27 nodal points. Note that the initial and final nodal points are $P_0 = (x_0, y_0) = (2, 0.2)$ and $P_N = (x_N, y_N) = (-2, 0.2)$ respectively.

The spike tool path is a *scaled* version of the original spike test function using a scale factor of 0.15. In particular, the initial and final nodal points are thus $P_0 = (x_0, y_0) = (0.3, 0.03)$ and $P_N = (x_N, y_N) = (-0.3, 0.03)$ respectively. Figure 5.9 shows the 27 nodal points used to approximate the spike tool path.

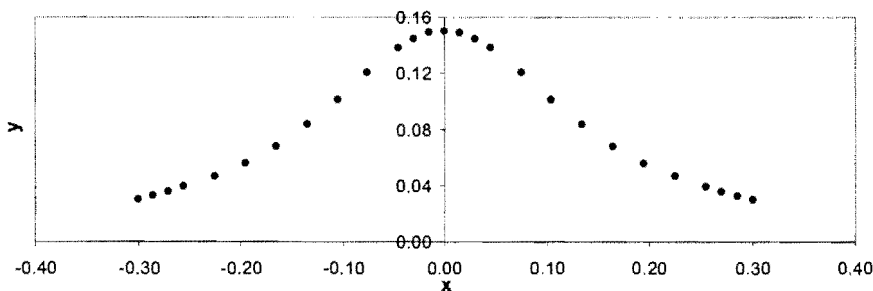


Figure 5.9: Nodal points used to approximate the spike tool path.

The OCAS trajectory-planning methodology (**Chapter 3**) is again used to approximate the spike tool path with $\ddot{s}_{allow} = 0.01 \text{ m/s}^2$ and $v^* = 1.0 \text{ m/min}$ resulting in a total motion time of 41.95 s. The simulation is again done with $n_{time} = 5$.

As in the case of the parabolic tool path, the moving platform of the test-model must maintain a tangential orientation with respect to the prescribed spike tool path. The variation of the orientation angle [degrees] as the moving platform traces the spike tool path, is depicted in Figure 5.10.

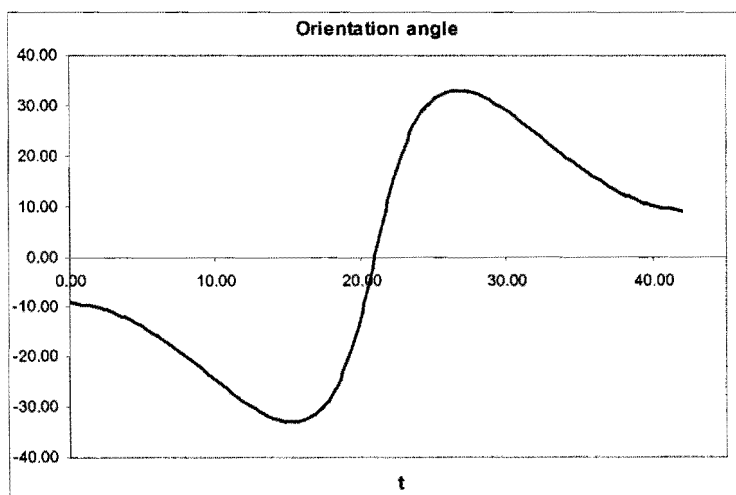
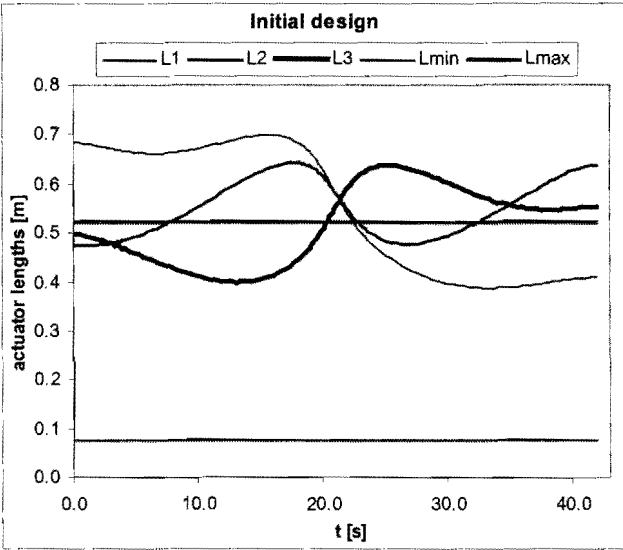
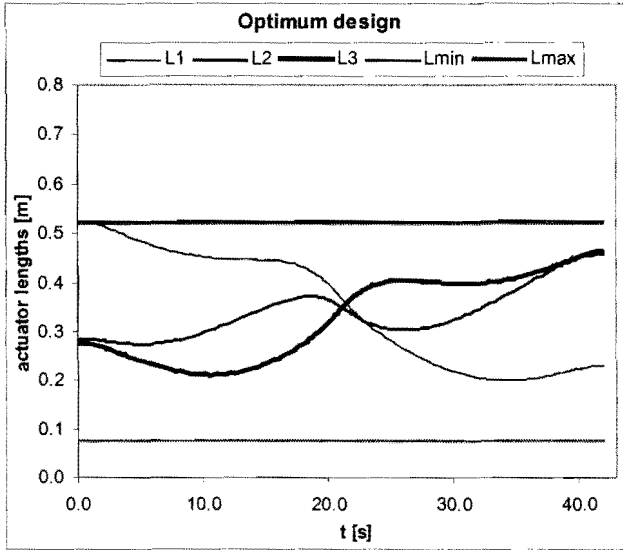


Figure 5.10: Variation in the orientation angle for the spike tool path.

5.3.2 Optimization results

The initial and optimum test-model designs for the spike tool path are compared in Table 5.3, with graphical insets 2(a) – 2(d).

Initial design	Optimum design
$\mathbf{X}^0 = [0.4, 0.4, -0.4, -0.4, 0.2]^T$	$\mathbf{X}^* = [0.21174, 0.29788, -0.17937, -0.27835, 0.18509]^T$
Inequality constraint values (see Section D.3):	
$C_1(\mathbf{X}^0) = -0.05$ $C_2(\mathbf{X}^0) = -0.3$ $C_3(\mathbf{X}^0) = -0.065$ $C_4(\mathbf{X}^0) = -0.287$ $C_5(\mathbf{X}^0) = -0.07$ $C_6(\mathbf{X}^0) = -0.087$ $\rightarrow C_7(\mathbf{X}^0) = 0.17403$ $\rightarrow C_8(\mathbf{X}^0) = 0.11745$ $\rightarrow C_9(\mathbf{X}^0) = 0.11302$ $C_{10}(\mathbf{X}^0) = -0.27092$ $C_{11}(\mathbf{X}^0) = -0.27092$ $C_{12}(\mathbf{X}^0) = -0.08751$ $\rightarrow C_{13}(\mathbf{X}^0) = 0.11249$ $C_{14}(\mathbf{X}^0) = -0.03529$ $C_{15}(\mathbf{X}^0) = -0.05145$ $C_{16}(\mathbf{X}^0) = -0.02809$ $C_{17}(\mathbf{X}^0) = -0.04628$ $C_{18}(\mathbf{X}^0) = -0.05358$ $C_{19}(\mathbf{X}^0) = -0.05924$ $C_{20}(\mathbf{X}^0) = -0.08094$ $C_{21}(\mathbf{X}^0) = -0.08051$ $C_{22}(\mathbf{X}^0) = -0.05931$ \rightarrow constraint violation	$C_1(\mathbf{X}^*) = -0.23826$ $C_2(\mathbf{X}^*) = -0.11174$ $C_3(\mathbf{X}^*) = -0.16712$ $C_4(\mathbf{X}^*) = -0.18488$ $C_5(\mathbf{X}^*) = -0.08491$ $C_6(\mathbf{X}^*) = -0.07209$ $\Rightarrow C_7(\mathbf{X}^*) = -0.511 \times 10^{-5}$ $C_8(\mathbf{X}^*) = -0.05923$ $C_9(\mathbf{X}^*) = -0.06545$ $C_{10}(\mathbf{X}^*) = -0.05029$ $C_{11}(\mathbf{X}^*) = -0.05029$ $C_{12}(\mathbf{X}^*) = -0.16093$ $\Rightarrow C_{13}(\mathbf{X}^*) = 0.687 \times 10^{-5}$ $C_{14}(\mathbf{X}^*) = -0.00220$ $C_{15}(\mathbf{X}^*) = -0.05317$ $\Rightarrow C_{16}(\mathbf{X}^*) = 0.281 \times 10^{-6}$ $\Rightarrow C_{17}(\mathbf{X}^*) = -0.535 \times 10^{-5}$ $C_{18}(\mathbf{X}^*) = -0.02511$ $C_{19}(\mathbf{X}^*) = -0.01017$ $C_{20}(\mathbf{X}^*) = -0.02684$ $C_{21}(\mathbf{X}^*) = -0.03971$ $C_{22}(\mathbf{X}^*) = -0.10923$ \Rightarrow constraint active
Variation of actuator leg lengths along the spike tool path:	
 <p>Initial design</p>	 <p>Optimum design</p>
2(a)	2(b)

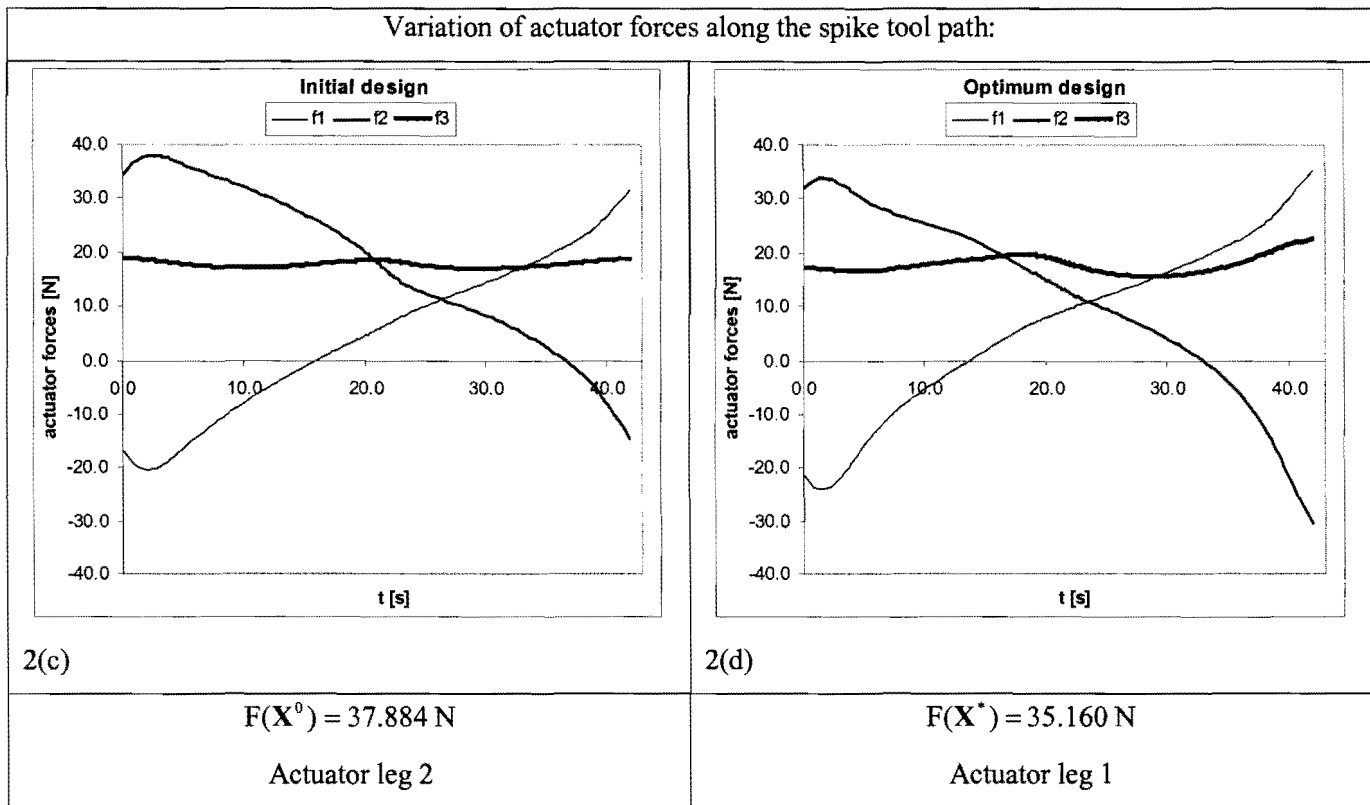


Table 5.3: Comparison between the initial and optimum designs for the spike tool path.

The violated inequality constraints associated with the *infeasible initial design* correspond to constraint functions C_7 , C_8 , C_9 and C_{13} (see expressions (D.11) and (D.14)). Again looking at figure inset 2(a), it is evident that all three actuator legs ℓ_1 , ℓ_2 and ℓ_3 will violate the maximum allowable actuator leg length if the spike tool path is to be traced with the initial design \mathbf{X}^0 , explaining why the inequality constraint function values $C_7(\mathbf{X}^0)$, $C_8(\mathbf{X}^0)$, $C_9(\mathbf{X}^0)$ are greater than zero. The inequality constraint corresponding to C_{13} prevents the excessive side way movement of the moving platform towards the right hand side as explained in Section D.3.3.4.

Figure inset 2(b) shows that in the case of the *feasible optimum design* \mathbf{X}^* , the variation in the actuator legs lies within the specified minimum and maximum allowable bounds. The active constraints correspond to C_7 , C_{13} , C_{16} and C_{17} (see respective expressions (D.11), (D.14), (D.17) and (D.18)). The optimum solution is found after 156 optimization iterations and utilizing 4 minutes and 53 seconds computational time on a Pentium IV 1.5GHz computer with 640 MB DDRAM. LFOPC again terminated on criterion 2 ($\epsilon_x \leq 10^{-5}$).

5.3.3 Analysis of convergence to optimum

Figure 5.11 shows the convergence history of the objective function.

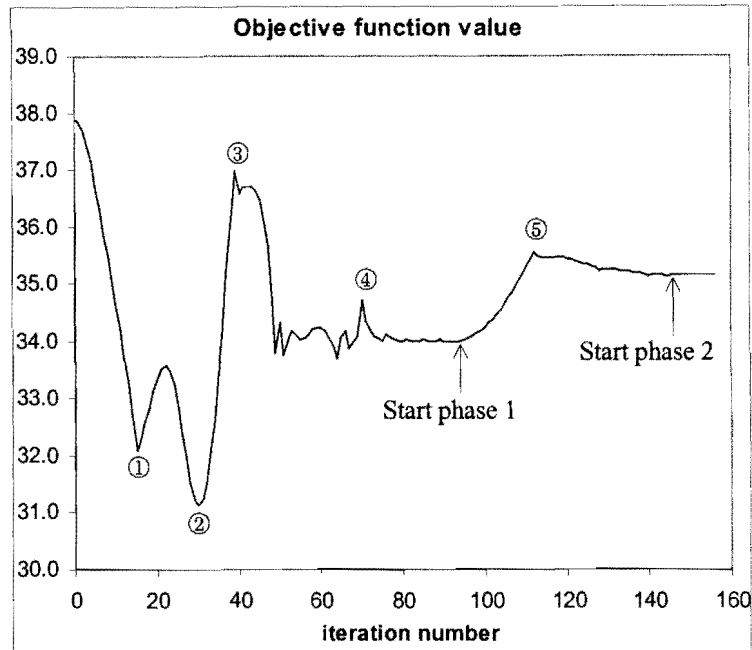


Figure 5.11: Convergence history of the objective function for the spike tool path.

Labels ① – ⑤ in Figure 5.11 are used in Table 5.4 to relate the *iteration number* and *phase* of the LFOPC-algorithm (see **Appendix C**) to the actuator leg responsible for the *maximum magnitude actuator force* (see Section 4.2.2) and the violated inequality constraints in the respectively indicated regions.

Labels	Iteration No.	LFOPC-Phase	Act. leg	Violated Inequality Constraints
X^0	0	0	l_2	C_7 C_8 C_9 C_{13}
①	15	0	l_2	C_7 C_8 C_9 C_{13}
	16	0	l_1	C_7 C_8 C_{13}
	17	0	l_1	C_7 C_8 C_{13}
②	30	0	l_1	C_7 C_{13} C_{16} C_{17}
	31	0	l_1	C_7 C_{13} C_{16}
③	39	0	l_1	C_7 C_{16}
	40	0	l_1	C_7 C_{16}
	41	0	l_1	C_7 C_{16}
	42	0	l_1	C_7

④	64	0	l_1	C_7	C_{13}	C_{16}	C_{17}
	65	0	l_2	C_7	C_{13}	C_{16}	C_{17}
	66	0	l_1	C_7	C_{16}	C_{17}	
	67	0	l_1	C_7	C_{13}	C_{16}	C_{17}
	68	0	l_1	C_7	C_{13}	C_{16}	C_{17}
	69	0	l_2	C_7	C_{13}	C_{16}	
	70	0	l_1	C_7	C_{16}	C_{17}	
LFOPC phase- change	87	0	l_1	C_7	C_{13}	C_{16}	C_{17}
	88	0	l_2	C_7	C_{13}	C_{16}	C_{17}
	89	0	l_1	C_7	C_{13}	C_{16}	C_{17}
	90	0	l_1	C_7	C_{13}	C_{16}	C_{17}
	91	0	l_1	C_7	C_{13}	C_{16}	C_{17}
	92	0	l_1	maximum violated constraint value: $C_7(\mathbf{X}^{92}) = 0.00436$			
	92	1	l_1	C_7	C_{13}	C_{16}	C_{17}
⑤	93	1	l_1	C_7	C_{13}	C_{16}	C_{17}
	112–114	1	l_1	none			
	115	1	l_1	C_7			
LFOPC phase- change	116	1	l_1	C_7			
	145	1	l_1	C_7	C_{13}	C_{17}	
	146	1	l_1	C_7	C_{13}	C_{16}	C_{17}
	146	2	l_1	C_7	C_{13}	C_{16}	C_{17}
\mathbf{X}^*	147	2	l_1	C_7	C_{13}	C_{16}	C_{17}
	156	2	l_1	C_7	C_{13}	C_{16}	C_{17} (active)

Table 5.4: Comparative table for the spike tool path objective function vs. iteration number curve (see Figure 5.11).

The first LFOPC phase-change from phase 0 to phase 1 occurs at iteration number 92, hence the resulting increase in the objective function value between labels ④ and ⑤ in Figure 5.11 as the penalty parameter is increased at the start of phase 1. The spiky behavior of the objective function value at labels ① and ④ can again be explained by the switch in the actuator leg responsible for the maximum magnitude actuator force, that occur in these regions.

The convergence histories of the respective design variables x_i , $i = 1, 2, \dots, 5$ are shown in Figure 5.12. Again effective convergence with respect to feasibility is obtained at the end of phase 0 after only 92 iterations with the maximum violated constraint value $C_7(\mathbf{X}^{92}) = 0.00436 \text{ m} = 4.36 \text{ mm}$. Note also, that there is a switch between actuator legs ℓ_1 and ℓ_2 responsible for the maximum magnitude actuator force at iteration number 88, just before the end of phase 0. This corresponds to the behavior of the actuator leg forces associated with the optimum design \mathbf{X}^* (figure inset 2(d)). The maximum magnitude of the force in actuator leg ℓ_1 , $f_1 = 35.160 \text{ N}$ occurring at time instant $t = 41.95 \text{ s}$, is only slightly larger than the maximum magnitude of the force in actuator leg ℓ_2 , $f_2 = 33.838 \text{ N}$ occurring at time instant $t = 1.71 \text{ s}$.

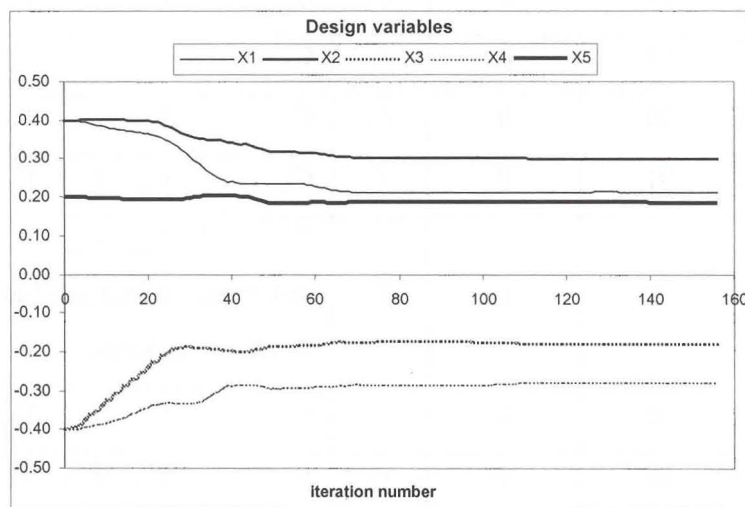
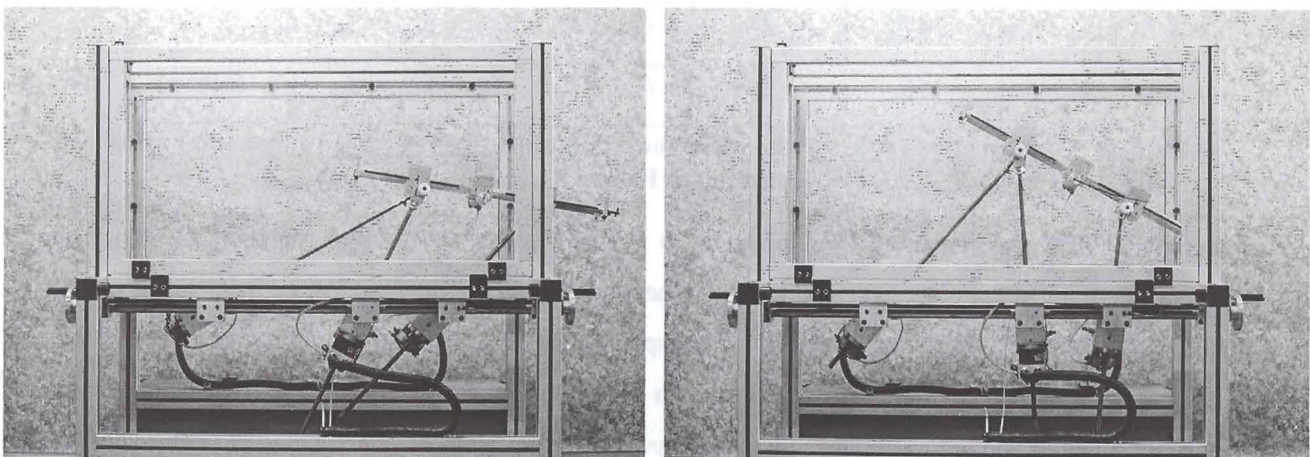


Figure 5.12: Convergence histories of design variables X_i , $i = 1, 2, \dots, 5$ for the spike tool path.

5.3.4 Execution of the spike tool path

Figure 5.13 shows a series of photographs taken at different time instants as the spike tool path is traced. Similarly to the parabolic tool path, the spike tool path is executed with a tangentially orientated moving platform (see Figure 5.10).



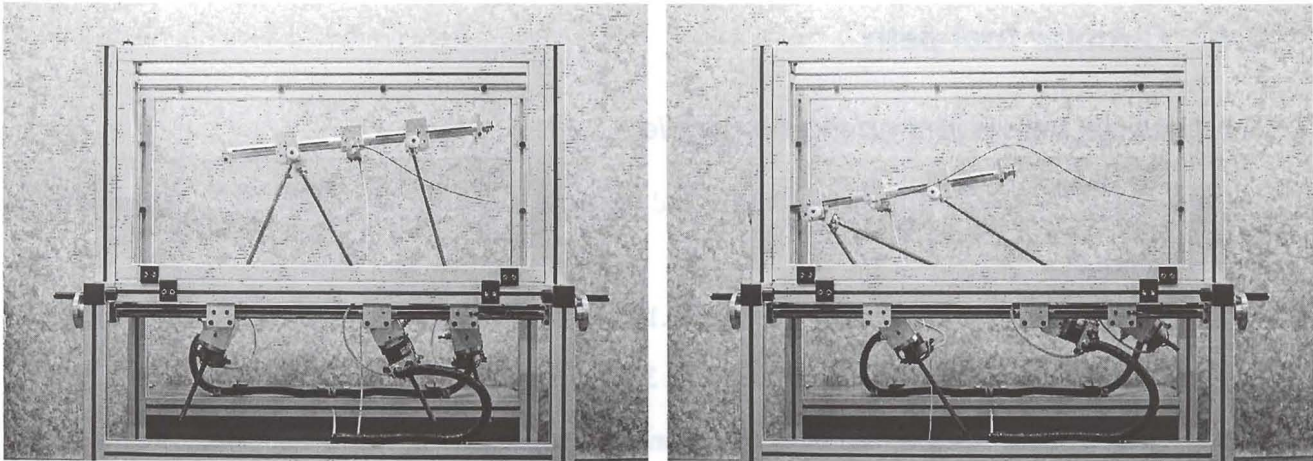


Figure 5.13: Execution of the spike tool path.

The close-up view of the executed spike tool path (Figure 5.14) shows that the traced spike tool path closely resembles the prescribed spike tool path specified by Figure 5.9.

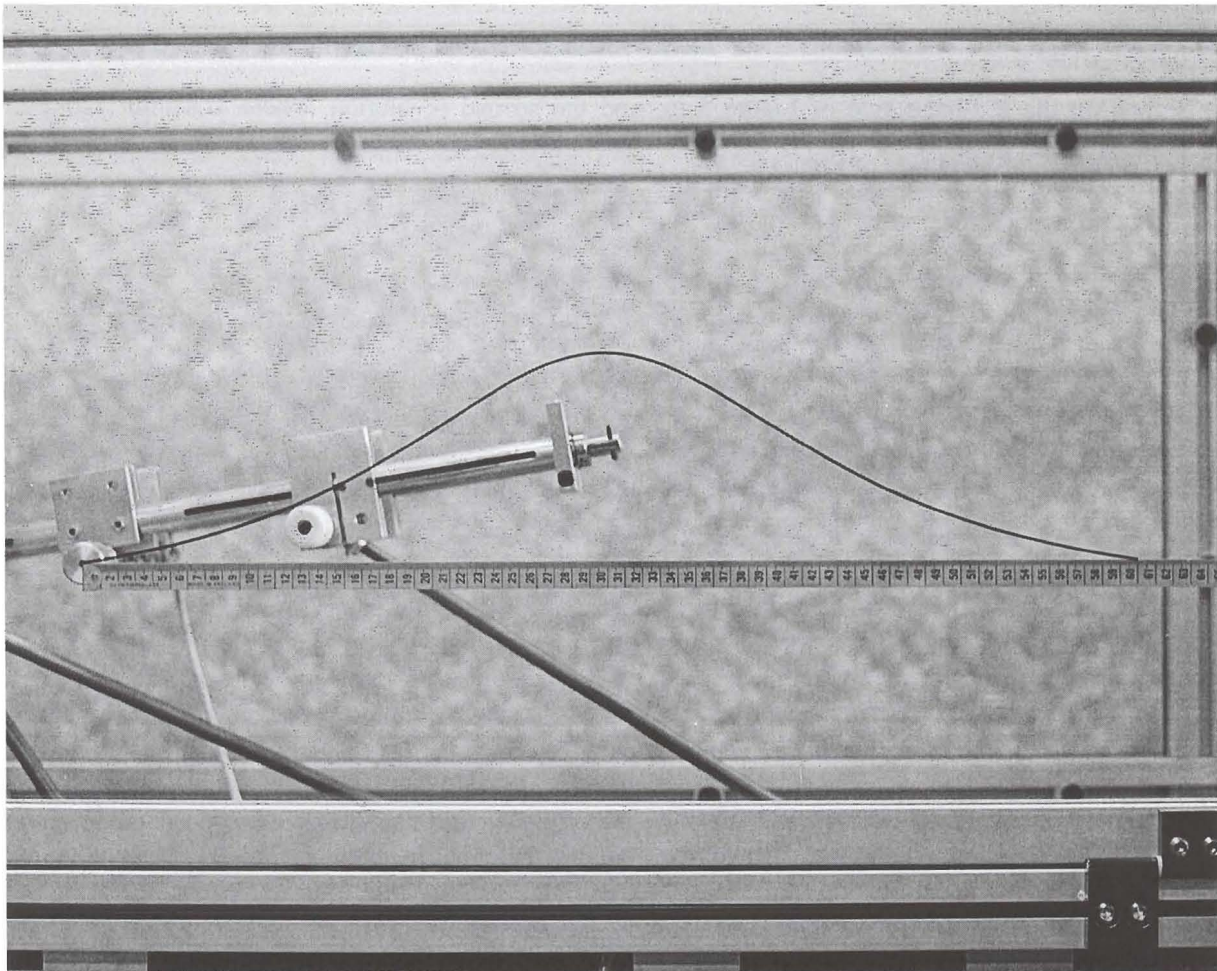


Figure 5.14: Close-up view of the executed spike tool path.

5.4 Circular tool path

5.4.1 Nodal points and orientation angle

The diameter of the circular tool path is 0.35 m and the circle is centered at $(x, y) = (0, 0)$. Hence the path is defined by

$$x^2 + y^2 = (0.175)^2 \quad (5.2)$$

In agreement with the circular *test curve* of Section 3.5.3, the nodal points $\{P_i = (x_i, y_i), i = 0, 1, 2, \dots, N\}$ of the circular *tool path* are specified using corresponding sweep angles $\beta_i \in [0^\circ, 720^\circ]$, where the sweep angle is measured clockwise from the positive x-axis. For any specific sweep angle $\beta_i, i = 0, 1, 2, \dots, N$, the corresponding x- and y-values are given by $x_i = 0.175 \cos \beta_i$, and $y_i = 0.175 \sin \beta_i$ respectively. The sequence of sweep angles $\{\beta_i\}$, is chosen such that starting at $\beta = 0^\circ$, two CCW revolutions are followed. A total of 79 nodal points cover the two revolutions. The first revolution where $\beta \in [0^\circ, 360^\circ]$ is shown on the left-hand side of Figure 5.15, and the second revolution, where $\beta \in [360^\circ, 720^\circ]$ is shown on the right-hand side of Figure 5.15.

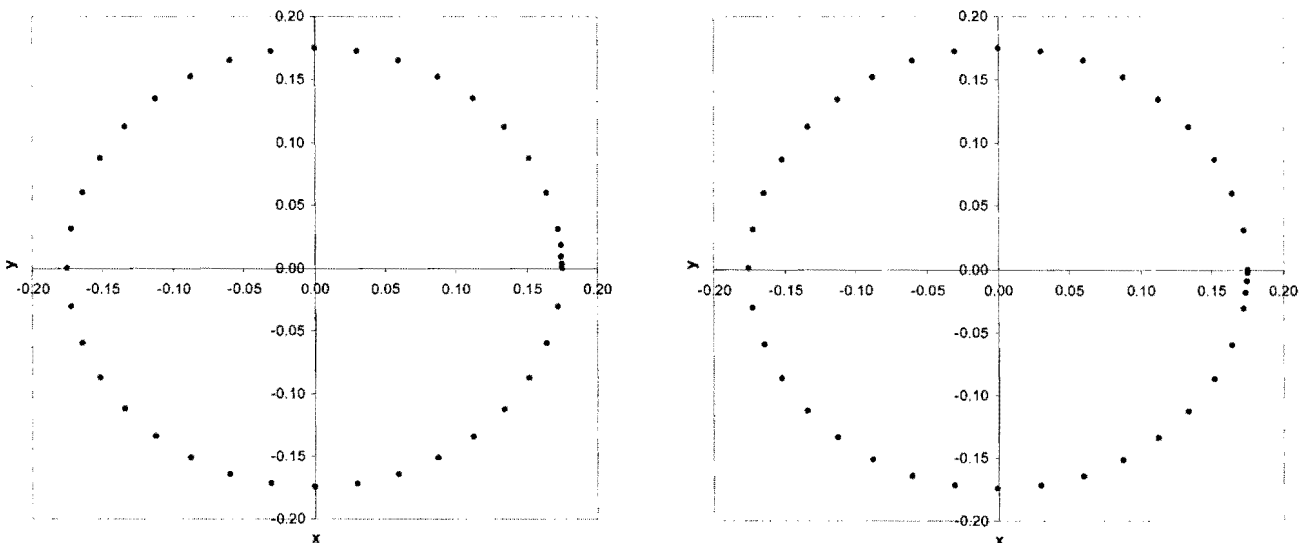


Figure 5.15: Nodal points used to approximate the two revolutions of the circular tool path.

The total time required to complete the two revolutions is 135.61 s, using the OCAS trajectory-planning methodology with $\ddot{s}_{\text{allow}} = 0.01 \text{ m/s}^2$, $v^* = 1.0 \text{ m/min}$ and $n_{\text{time}} = 5$.

Other than in the cases of the parabolic and spike tool paths, a fixed moving platform orientation $\phi_i \equiv 0$ is maintained as the circular tool path is traced.

5.4.2 Optimization results

A comparison between the initial and optimum test-model designs for the circular tool path is shown in Table 5.5, with figure insets 3(a) – 3(d).

Note that the kinematics and kinetics of the two revolutions are *not identical*. The distribution of the nodal points is specifically chosen to accommodate acceleration at the start of the first revolution, and deceleration at the end of the second revolution (see Figure 5.15). The effect of this on figure insets 3(a) – 3(d) are the slight differences between the respective curves at time instants $t = 0$ s and $t = 135.61$ s.

Initial design		Optimum design	
$\mathbf{X}^0 = [0.4, 0.4, -0.4, -0.4, 0.2]^T$		$\mathbf{X}^* = [0.34476, 0.39829, -0.28487, -0.36676, 0.25238]^T$	
Inequality constraint values (see Section D.3):			
$C_1(\mathbf{X}^0) = -0.05$	$C_2(\mathbf{X}^0) = -0.3$	$C_1(\mathbf{X}^*) = -0.10524$	$C_2(\mathbf{X}^*) = -0.24476$
$C_3(\mathbf{X}^0) = -0.065$	$C_4(\mathbf{X}^0) = -0.287$	$C_3(\mathbf{X}^*) = -0.06671$	$C_4(\mathbf{X}^*) = -0.28529$
$C_5(\mathbf{X}^0) = -0.07$	$C_6(\mathbf{X}^0) = -0.087$	$C_5(\mathbf{X}^*) = -0.01762$	$C_6(\mathbf{X}^*) = -0.13938$
$\rightarrow C_7(\mathbf{X}^0) = 0.09721$	$\rightarrow C_8(\mathbf{X}^0) = 0.09721$	$C_7(\mathbf{X}^*) = -0.00514$	$\Rightarrow C_8(\mathbf{X}^*) = 0.326 \times 10^{-3}$
$\rightarrow C_9(\mathbf{X}^0) = 0.05$	$C_{10}(\mathbf{X}^0) = -0.15$	$C_9(\mathbf{X}^*) = -0.04408$	$C_{10}(\mathbf{X}^*) = -0.03487$
$C_{11}(\mathbf{X}^0) = -0.15$	$C_{12}(\mathbf{X}^0) = -0.21$	$C_{11}(\mathbf{X}^*) = -0.03487$	$C_{12}(\mathbf{X}^*) = -0.20608$
$C_{13}(\mathbf{X}^0) = -0.01$	$C_{14}(\mathbf{X}^0) = -0.03130$	$C_{13}(\mathbf{X}^*) = -0.06916$	$C_{14}(\mathbf{X}^*) = -0.00157$
$C_{15}(\mathbf{X}^0) = -0.04642$	$C_{16}(\mathbf{X}^0) = -0.03130$	$C_{15}(\mathbf{X}^*) = -0.00911$	$\Rightarrow C_{16}(\mathbf{X}^*) = -0.114 \times 10^{-4}$
$C_{17}(\mathbf{X}^0) = -0.05081$	$C_{18}(\mathbf{X}^0) = -0.04334$	$C_{17}(\mathbf{X}^*) = -0.02786$	$C_{18}(\mathbf{X}^*) = -0.04462$
$C_{19}(\mathbf{X}^0) = -0.06975$	$C_{20}(\mathbf{X}^0) = -0.09344$	$C_{19}(\mathbf{X}^*) = -0.01857$	$C_{20}(\mathbf{X}^*) = -0.00119$
$C_{21}(\mathbf{X}^0) = -0.08546$	$C_{22}(\mathbf{X}^0) = -0.06502$	$C_{21}(\mathbf{X}^*) = -0.08240$	$C_{22}(\mathbf{X}^*) = -0.06527$
\rightarrow constraint violation		\Rightarrow constraint active	

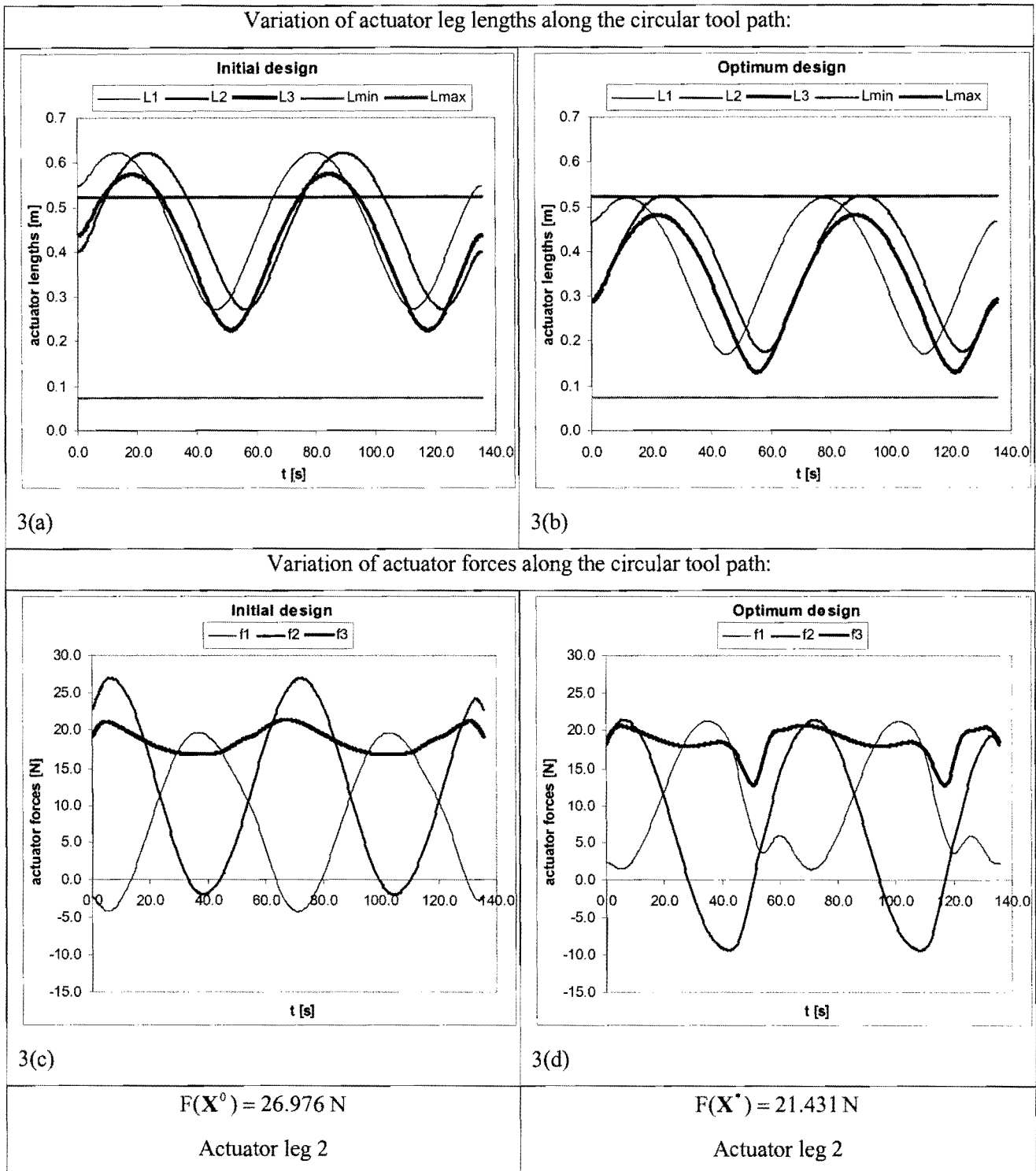


Table 5.5: Comparison between the initial and optimum designs for the circular tool path.

Starting with the infeasible initial design \mathbf{X}^0 (see the unallowable variation in actuator leg lengths in inset 3(a), and associated positive inequality constraint function values $C_7(\mathbf{X}^0)$, $C_8(\mathbf{X}^0)$ and $C_9(\mathbf{X}^0)$), the optimum design \mathbf{X}^* is found in 73 optimization iterations. This requires 6 minutes and 35 seconds computational time on a Pentium IV 1.5 GHz computer with 640 MB DDRAM. The LFOPC-algorithm again terminated on criterion 2 ($\epsilon_x \leq 10^{-5}$) listed in Section 4.4.

Note that the absolute values of the two active constraints, identified from the positive values of $C_8(\mathbf{X}^*)$ and $C_{16}(\mathbf{X}^*)$ (expressions (D.11) and (D.17)) are at least one order of magnitude larger than the absolute values of the active constraints for the optimization of the parabolic and spike test functions. In spite of the fact that inequality constraint C_8 is violated by 0.326×10^{-3} m (0.326 mm), this violation lies well within the minimum safety margin of 5 mm that was used during the formulation of the inequality constraints.

The effectiveness of the chosen “maximum magnitude actuator force” objective function (see Section 4.2.2) is borne out by comparing figure insets 3(c) and 3(d). In figure inset 3(c) showing the actuator force variations for the initial design \mathbf{X}^0 , actuator force f_2 is predominant with significant elevations at time instants $t = 6.23$ s, $t = 72.20$ s and $t = 132.45$ s. On the other hand, the actuator force variations associated with the optimum design \mathbf{X}^* in figure inset 3(d) shows a much more level distribution in terms of the maximum forces in all three actuator legs.

5.4.3 Analysis of convergence to optimum

Figure 5.16 shows the convergence history of the objective function.

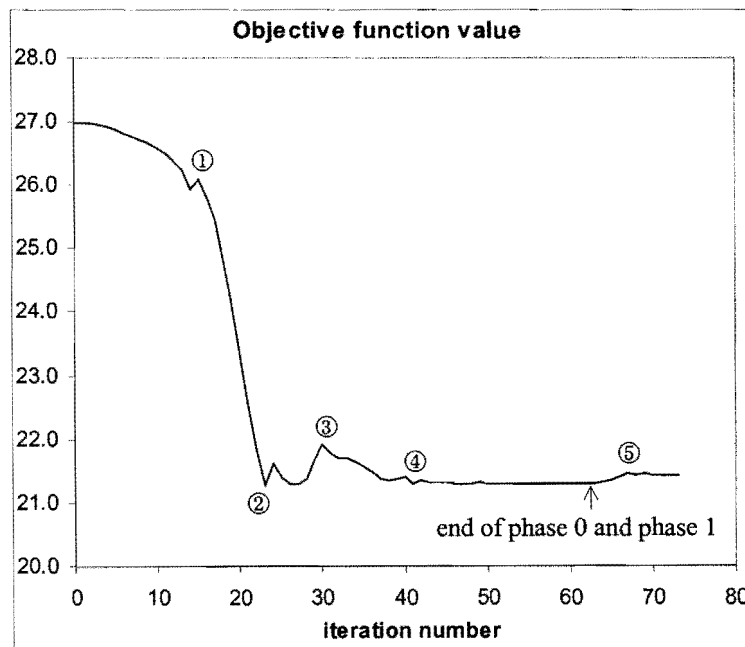


Figure 5.16: Convergence history of the objective function for the circular tool path.

Labels ① – ⑤ in Figure 5.16 are used in Table 5.6 to relate the behavior of the convergence curve of the objective function in the respective indicated regions to the iteration number and phase of the LFOPC-algorithm, the actuator leg responsible for the maximum magnitude actuator force and the violated inequality constraints.

Labels	Iteration No.	LFOPC-Phase	Act. leg	Violated Inequality Constraints
X^0	0	0	l_2	C_7 C_8 C_9
①	14	0	l_2	C_{18}
	15	0	l_2	C_{18}
	16	0	l_2	C_{18}
②	23	0	l_2	C_8 C_{16}
	24	0	l_1	C_8 C_{16} C_{20}
	25	0	l_1	C_8 C_{16} C_{20}
	26	0	l_1	C_8 C_{16}
	27	0	l_1	C_8 C_{16} C_{20}
	28	0	l_2	C_8 C_{16} C_{20}
	29	0	l_2	C_8 C_{16} C_{20}
③	30	0	l_2	C_8 C_{16} C_{20}
	31	0	l_2	C_8 C_{16} C_{20}
④	39	0	l_2	C_8 C_{16} C_{20}
	40	0	l_2	C_8 C_{16}
	41	0	l_1	C_8 C_{16} C_{20}
	42	0	l_2	C_8 C_{16} maximum violated constraint value $C_{16}(X^{42}) = 0.00110$
	43	0	l_1	C_{16}

LFOPC Phase- changes	60	0	l_2	C_{16}
	61	0	l_1	C_{16}
	62	0	l_2	C_{16} $C_{16}(\mathbf{X}^{62}) = 0.936 \times 10^{-3}$
	62	1	l_2	C_{16}
	63	1	l_2	C_{16} (only active constraint) see footnote [☆] at the end of Table 5.6
	63	2	l_2	C_{16}
	64	2	l_2	C_{16}
⑤	67	2	l_2	C_8
	68	2	l_2	C_8 C_{16}
	69	2	l_2	C_8
	70	2	l_2	C_8
	71	2	l_2	C_8
	72	2	l_2	C_8
\mathbf{X}^*	73	2	l_2	C_8 C_{16} (active) (only $C_{16} = 0$ enforced in LFOPC-phase 2)

[☆] Note that at the end of phase 1 only one constraint, corresponding to C_{16} , is identified to be active. In the subsequent stringent enforcement of this constraint in phase 2, the constraint corresponding to C_8 also incidentally becomes active. This explains the relative large value (but nevertheless of insignificant magnitude) of $C_8(\mathbf{X}^*)$ in Table 5.5. A diagrammatical representation of the situation that arises is sketched below

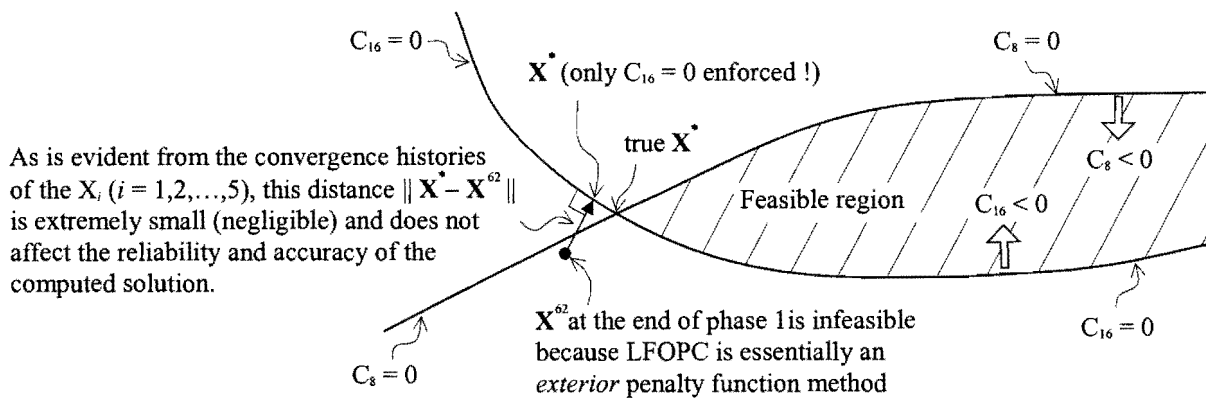


Table 5.6: Comparative table for the circular tool path objective function vs. iteration number curve (see Figure 5.16).

A switch in the actuator leg responsible for the maximum magnitude actuator force occurs in the vicinity of label ②. This again explains the non-smooth nature of the objective function vs. iteration number curve in this area (see Figure 5.16).

Note that since the initial design only violates the “allowable maximum leg length” inequality constraints (expression (D.11)), it may be possible to *intuitively* adjust the position of the prescribed tool path *relative* to the position of the planar machine in order to achieve feasibility. In terms of the set of design variables, this implies that *only* two design variables, X_3 and X_4 , need to be changed until the prescribed circular tool path is *feasibly* traced. Although this might seem to be an easier option, the inherent danger of this approach is the unknown occurrence of mechanical interference. This danger is evident from the fact that the optimum design \mathbf{X}^* found by LFOPC is associated with the two active constraints:

- C_8 an “allowable maximum leg length” inequality constraint (expression (D.11)), and
- C_{16} a “mechanical interference” inequality constraint (expression (D.17)).

The convergence histories of the respective design variables X_i , $i = 1, 2, \dots, 5$ are shown in Figure 5.17. Practical convergence (both with respect to feasibility and optimum objective function value), has already been achieved as early as iteration 42 with a maximum violated constraint function value of $C_{16}(\mathbf{X}^{42}) = 0.00110 \text{ m}$ (1.10 mm), and with the associated design vector given by $\mathbf{X}^{42} = [0.34901, 0.39819, -0.28277, -0.36638, 0.25303]^T$. Note that no significant changes in the values of the design variables occur after iteration 42 as can be seen from the optimum values of the design variables, $\mathbf{X}^* = [0.34476, 0.39829, -0.28487, -0.36676, 0.25238]^T$.

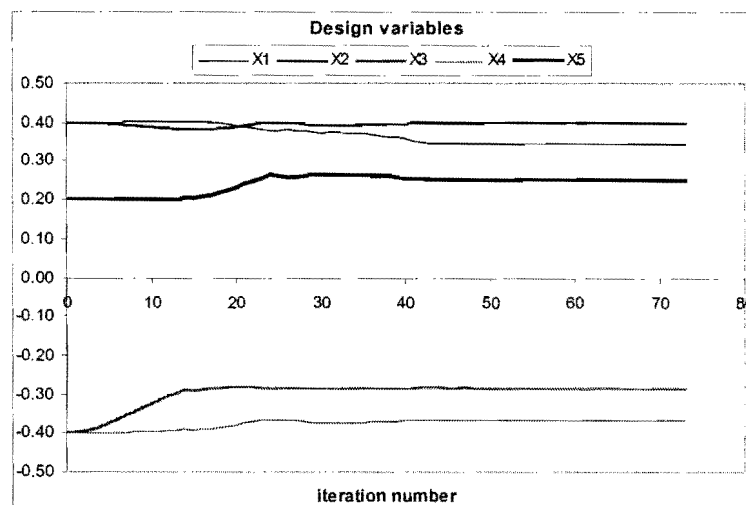


Figure 5.17: Convergence histories of design variables X_i , $i = 1, 2, \dots, 5$ for the circular tool path.

5.4.4 Execution of the circular tool path

The series of photographs shown in Figure 5.18 is of different instants during the execution of the first revolution of the circular tool path.

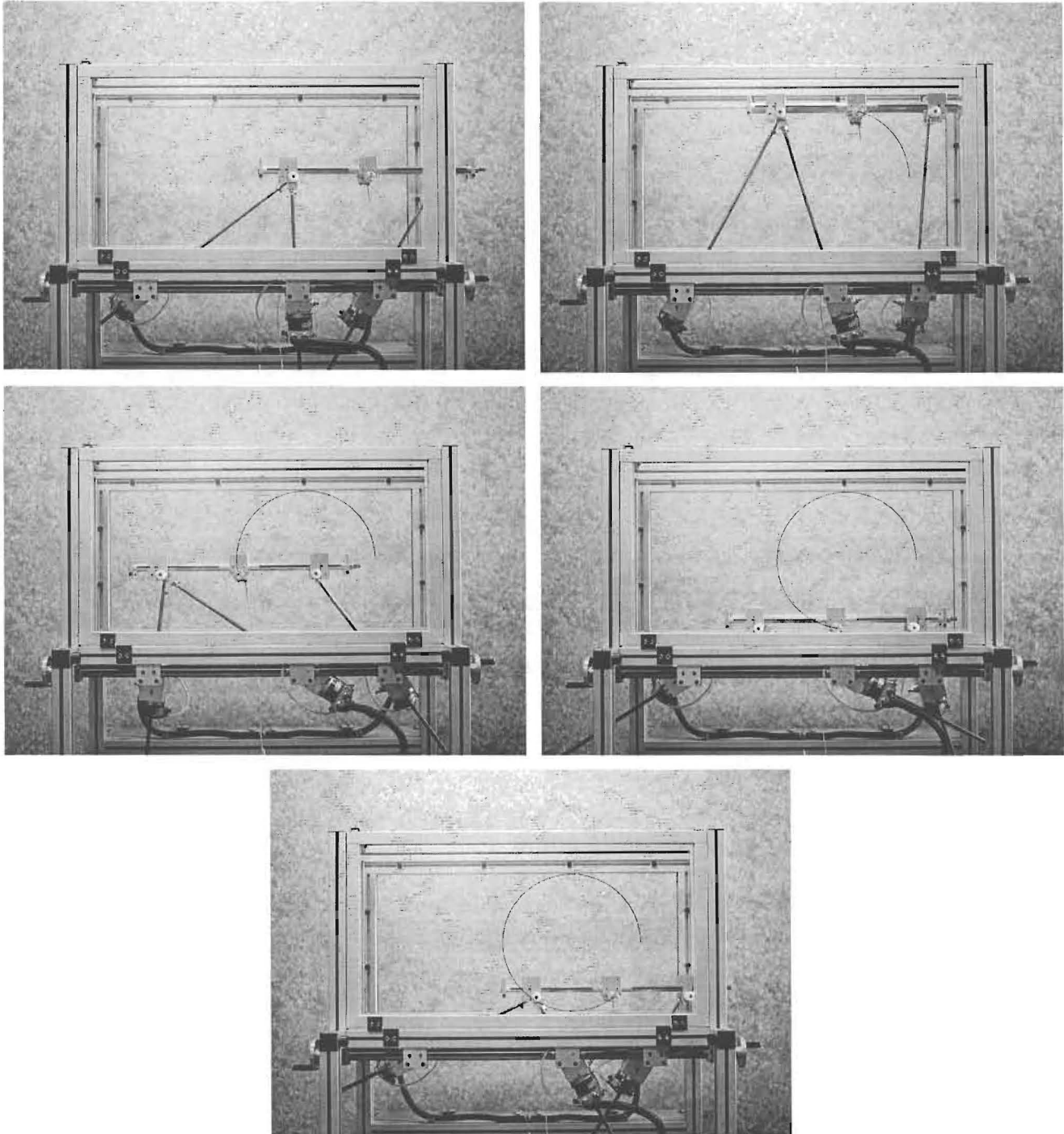


Figure 5.18: Execution of the circular tool path.

Figure 5.19 is a close-up of the traced circular tool path, showing that the diameter of the traced circle is approximately 350 mm (35 cm), and that the circle is smoothly traced.

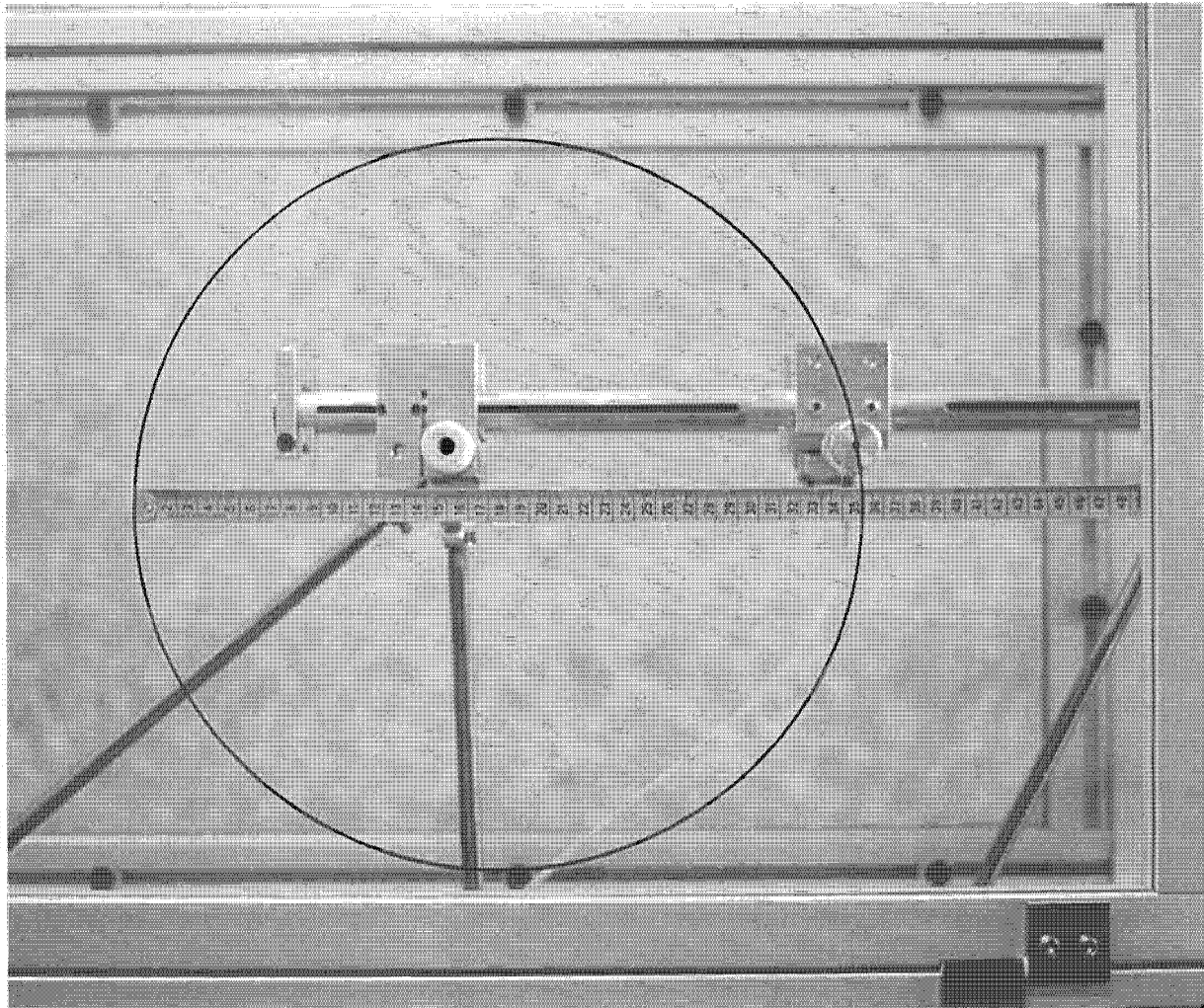


Figure 5.19: Close-up view of the executed circular tool path.

5.5 Spiral tool path

5.5.1 Nodal points and orientation angle

The spiral tool path is a scaled version of the logarithmic spiral test curve $\rho = e^{0.1\theta}$ of Section 3.5.4. Using a scale factor of 0.285, the 79 spiral tool path nodal points are as shown in Figure 5.20.

The motion time along the spiral tool path is 93.24 seconds with the specification of $\ddot{s}_{\text{ALLOW}} = 0.01 \text{ m/s}^2$, $v^* = 1.0 \text{ m/min}$ and $n_{\text{time}} = 5$ for the use of the OCAS trajectory-planning algorithm.

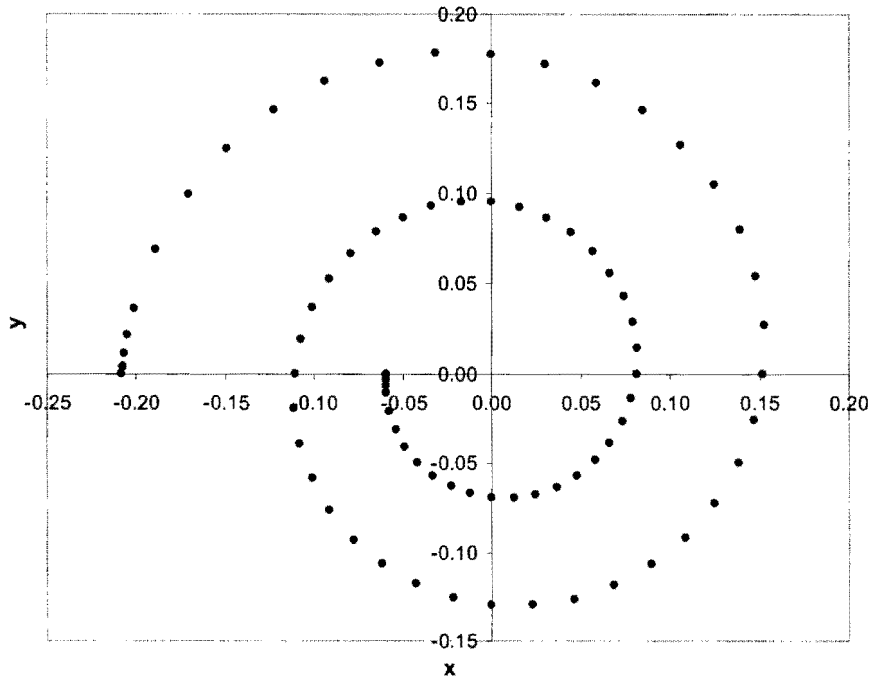


Figure 5.20: Nodal points used to approximate the spiral tool path.

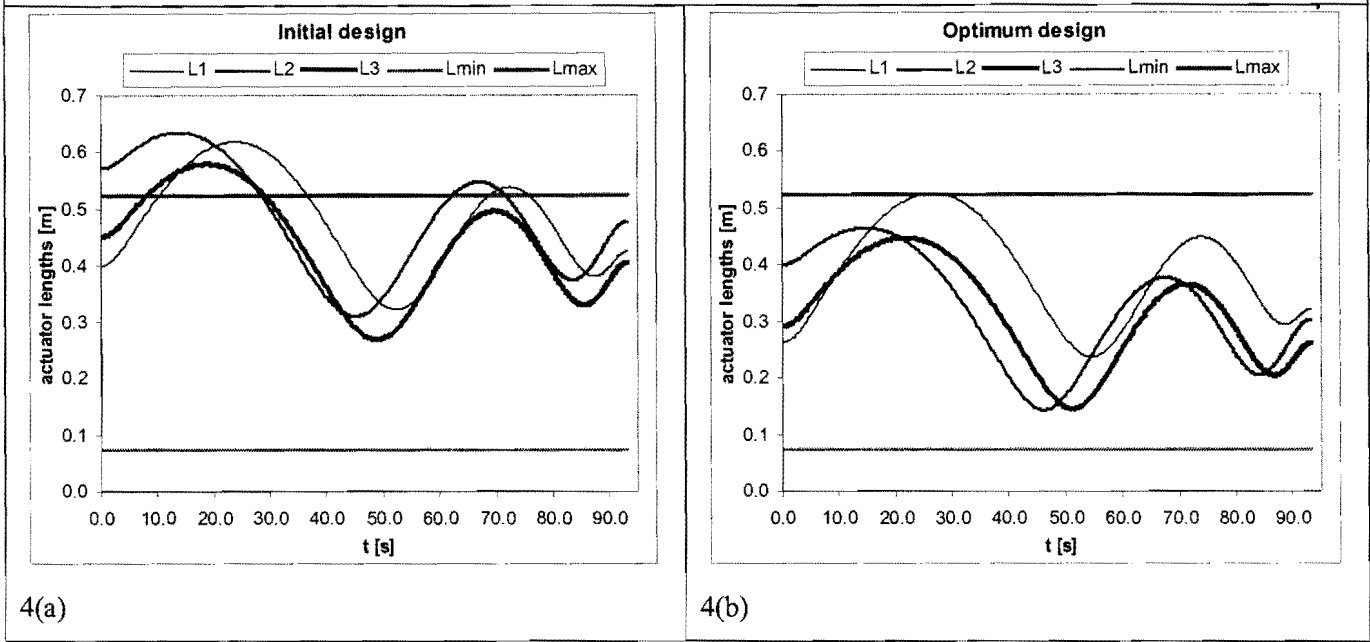
As for the circular tool path, the spiral tool path is traced with a fixed moving platform orientation $\phi_1 \equiv 0$.

5.5.2 Optimization results

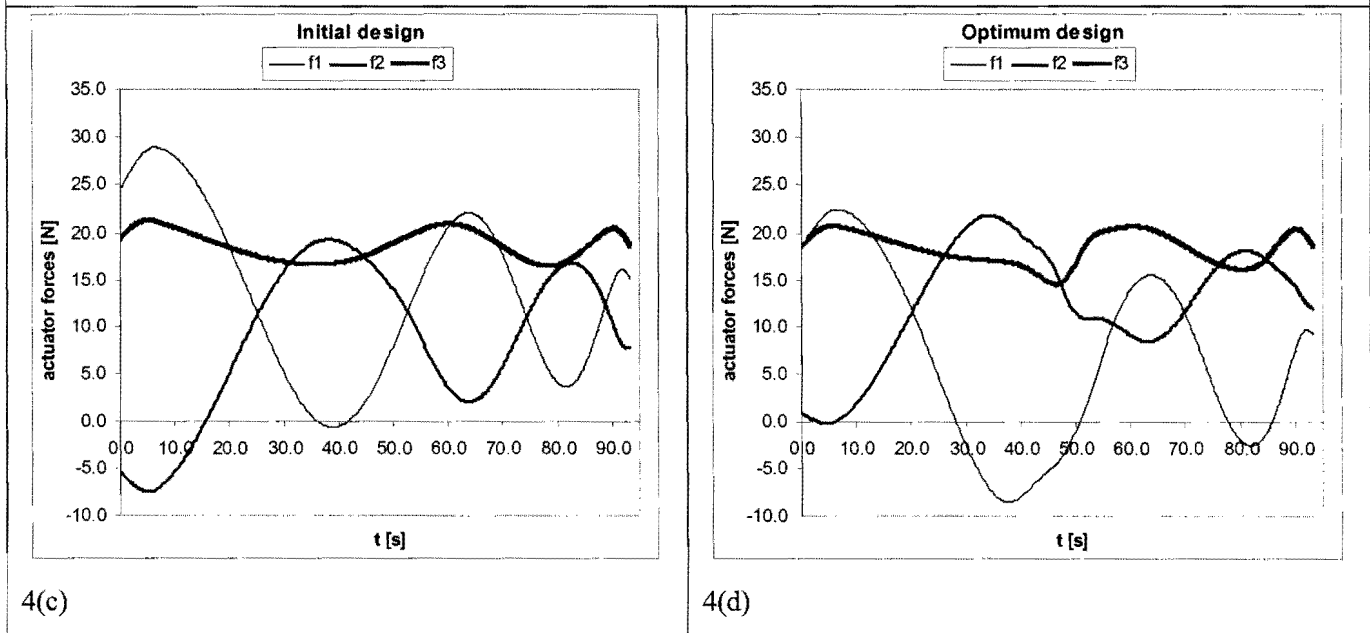
The initial and optimum test-model designs for the spiral tool path are compared in Table 5.7 (with figure insets 4(a) – 4(d)).

Initial design		Optimum design	
$\mathbf{X}^0 = [0.4, 0.4, -0.4, -0.4, 0.2]^T$		$\mathbf{X}^* = [0.32686, 0.34053, -0.26137, -0.40930, 0.15538]^T$	
Inequality constraint values (see Section D.3):			
$C_1(\mathbf{X}^0) = -0.05$	$C_2(\mathbf{X}^0) = -0.3$	$C_1(\mathbf{X}^*) = -0.12314$	$C_2(\mathbf{X}^*) = -0.22686$
$C_3(\mathbf{X}^0) = -0.065$	$C_4(\mathbf{X}^0) = -0.287$	$C_3(\mathbf{X}^*) = -0.12447$	$C_4(\mathbf{X}^*) = -0.22753$
$C_5(\mathbf{X}^0) = -0.07$	$C_6(\mathbf{X}^0) = -0.087$	$C_5(\mathbf{X}^*) = -0.11462$	$C_6(\mathbf{X}^*) = -0.04238$
$\rightarrow C_7(\mathbf{X}^0) = 0.09323$	$\rightarrow C_8(\mathbf{X}^0) = 0.10988$	$\Rightarrow C_7(\mathbf{X}^*) = 0.347 \times 10^{-6}$	$C_8(\mathbf{X}^*) = -0.06128$
$\rightarrow C_9(\mathbf{X}^0) = 0.05420$	$C_{10}(\mathbf{X}^0) = -0.19441$	$C_9(\mathbf{X}^*) = -0.07828$	$C_{10}(\mathbf{X}^*) = -0.05578$
$C_{11}(\mathbf{X}^0) = -0.19441$	$C_{12}(\mathbf{X}^0) = -0.17684$	$C_{11}(\mathbf{X}^*) = -0.05578$	$C_{12}(\mathbf{X}^*) = -0.28217$
$C_{13}(\mathbf{X}^0) = -0.03220$	$C_{14}(\mathbf{X}^0) = -0.03972$	$\Rightarrow C_{13}(\mathbf{X}^*) = 0.108 \times 10^{-5}$	$\Rightarrow C_{14}(\mathbf{X}^*) = 0.700 \times 10^{-6}$
$C_{15}(\mathbf{X}^0) = -0.05697$	$C_{16}(\mathbf{X}^0) = -0.03865$	$C_{15}(\mathbf{X}^*) = -0.03094$	$C_{16}(\mathbf{X}^*) = -0.03204$
$C_{17}(\mathbf{X}^0) = -0.06113$	$C_{18}(\mathbf{X}^0) = -0.06216$	$C_{17}(\mathbf{X}^*) = -0.02269$	$C_{18}(\mathbf{X}^*) = -0.00256$
$C_{19}(\mathbf{X}^0) = -0.06763$	$C_{20}(\mathbf{X}^0) = -0.09095$	$C_{19}(\mathbf{X}^*) = -0.06875$	$C_{20}(\mathbf{X}^*) = -0.11837$
$C_{21}(\mathbf{X}^0) = -0.09526$	$C_{22}(\mathbf{X}^0) = -0.06325$	$\Rightarrow C_{21}(\mathbf{X}^*) = 0.345 \times 10^{-5}$	$C_{22}(\mathbf{X}^*) = -0.06792$
\rightarrow constraint violation		\Rightarrow constraint active	

Variation of actuator leg lengths along the spiral tool path:



Variation of actuator forces along the spiral tool path:



$F(\mathbf{X}^0) = 28.914 \text{ N}$

Actuator leg 1

$F(\mathbf{X}^*) = 22.409 \text{ N}$

Actuator leg 1

Table 5.7: Comparison between the initial and optimum designs for the spiral tool path.

The initial design is *again infeasible* (see the variation in actuator leg lengths in inset 4(a) and the corresponding *positive* inequality constraint function values $C_7(\mathbf{X}^0)$, $C_8(\mathbf{X}^0)$ and $C_9(\mathbf{X}^0)$). The *feasible* optimum design (see figure inset 4(b)) is associated with active constraints corresponding to C_7 , C_{13} , C_{14} and C_{21} (see respective expressions (D.10), (D.14), (D.15) and (D.22)). Note that

corresponding to the circular tool path, the optimum variation in actuator forces of figure inset 4(d) shows a level distribution in terms of the maximum forces in all three actuator legs.

The optimum design, X^* , is found in 133 optimization iterations and utilizing 11 minutes and 46 seconds computational time on a Pentium IV 1.5 GHz computer with 640 MB DDRAM. As before, LFOPC terminated on criterion 2 ($\epsilon_x \leq 10^{-5}$) listed in Section 4.4.

5.5.3 Analysis of convergence to optimum

Figure 5.21 shows the convergence history of the objective function.

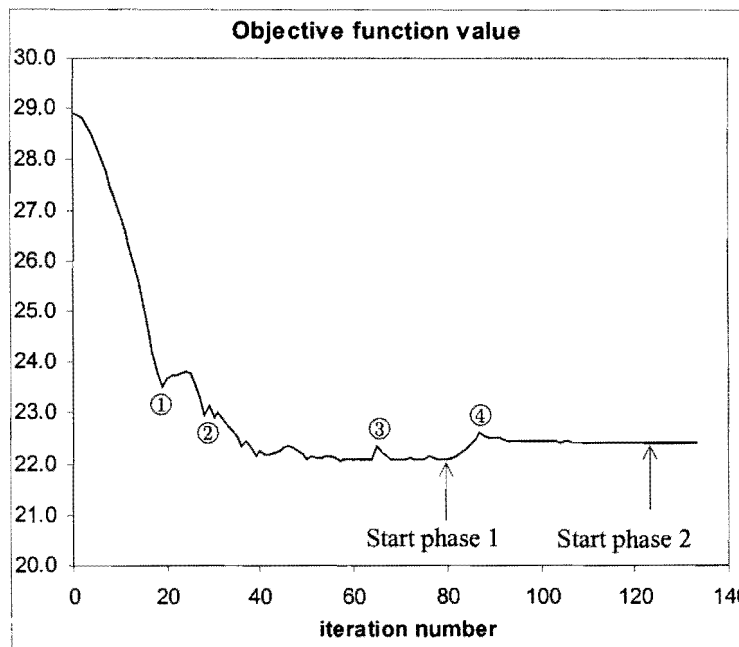


Figure 5.21: Convergence history of the objective function for the spiral tool path.

Table 5.8 with labels ① – ④ relate the behavior of the convergence curve of the objective function to iteration number, the LFOPC phases, the actuator leg responsible for the maximum magnitude actuator force, and the violated inequality constraints in the respectively indicated regions of the curve.

Labels	Iteration No.	LFOPC-Phase	Act. leg	Violated Inequality Constraints
X^0	0	0	l_1	C_7 C_8 C_9
①	18	0	l_1	C_{13} C_{18}
	19	0	l_1	C_{13} C_{14} C_{18}
	20	0	l_1	C_{13} C_{14} C_{18}
	21	0	l_1	C_{13} C_{18}
②	28-31	0	l_1	C_7 C_{13} C_{14}
③	63	0	l_1	C_7 C_{13} C_{14} C_{21}
	64	0	l_2	C_7 C_{13} C_{14} C_{21}
	65	0	l_1	C_7 C_{14} C_{21}
	66	0	l_1	C_7 C_{13} C_{14} C_{21}
LFOPC phase-change	78	0	l_1	C_7 C_{13} C_{14} C_{21}
	79	0	l_1	maximum violated constraint value $C_{21}(X^{79}) = 0.00316$
	79	1	l_1	C_7 C_{13} C_{14} C_{21}
	80	1	l_1	C_7 C_{13} C_{14} C_{21}
④	87-89	1	l_1	none
	90	1	l_1	C_7
LFOPC phase-change	125	1	l_1	C_7 C_{13} C_{14} C_{21}
	126	1	l_1	C_7 C_{13} C_{14} C_{21}
	126	2	l_1	C_7 C_{13} C_{14} C_{21}
	127	2	l_1	C_7 C_{14} C_{21}
X^*	133	2	l_1	C_7 C_{13} C_{14} C_{21} (active)

Table 5.8: Comparative table for the spiral tool path objective function vs. iteration number curve (see Figure 5.21)

Note that the actuator leg responsible for the maximum magnitude actuator force switches between l_1 and l_2 in the vicinity of label ③.

The convergence histories of the respective design variables $X_i, i = 1,2,\dots,5$ are shown in Figure 5.22. Again convergence (with respect to feasibility and objective function value), is effectively achieved at

the end of phase 0, after 79 iterations with the maximum violated constraint value $C_{21}(\mathbf{X}^{79}) = 0.00316 \text{ m}$ (3.16 mm).

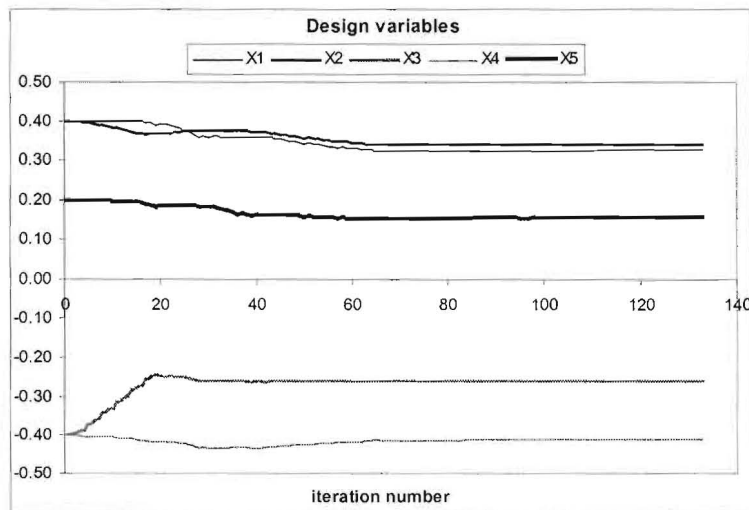
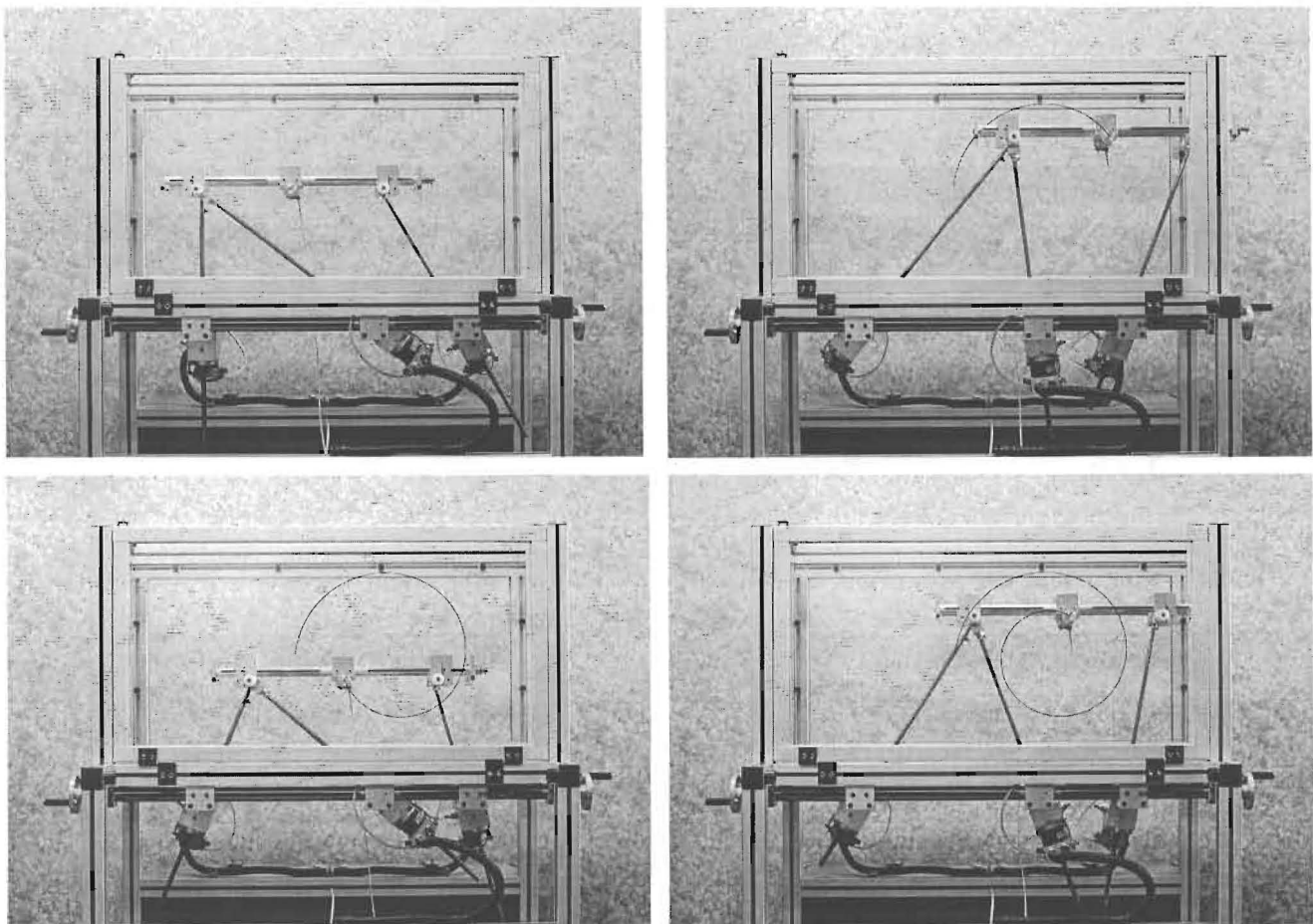


Figure 5.22: Convergence histories of design variables $X_i, i = 1, 2, \dots, 5$ for the spiral tool path.

5.5.4 Execution of the spiral tool path

The series of five photographs in Figure 5.23 depicts the tracing of the spiral tool path with a horizontally orientated moving platform ($\phi_1 = 0$).



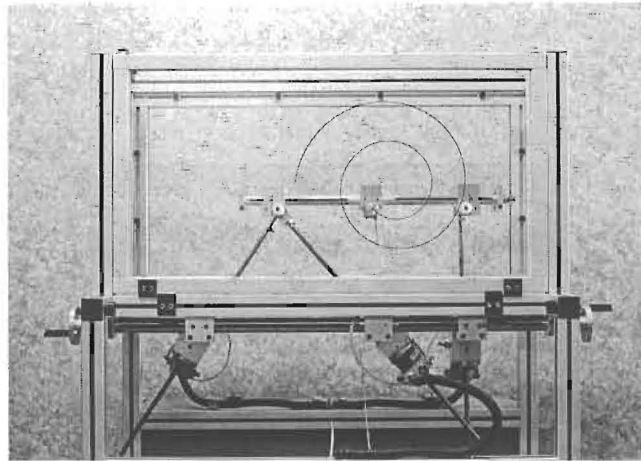


Figure 5.23: Execution of the spiral tool path.

The close-up view of the executed spiral tool path in Figure 5.24 shows its relative size and proportional shape. For all practical purposes the executed path corresponds accurately and smoothly to the spiral tool path prescribed by Figure 5.20.

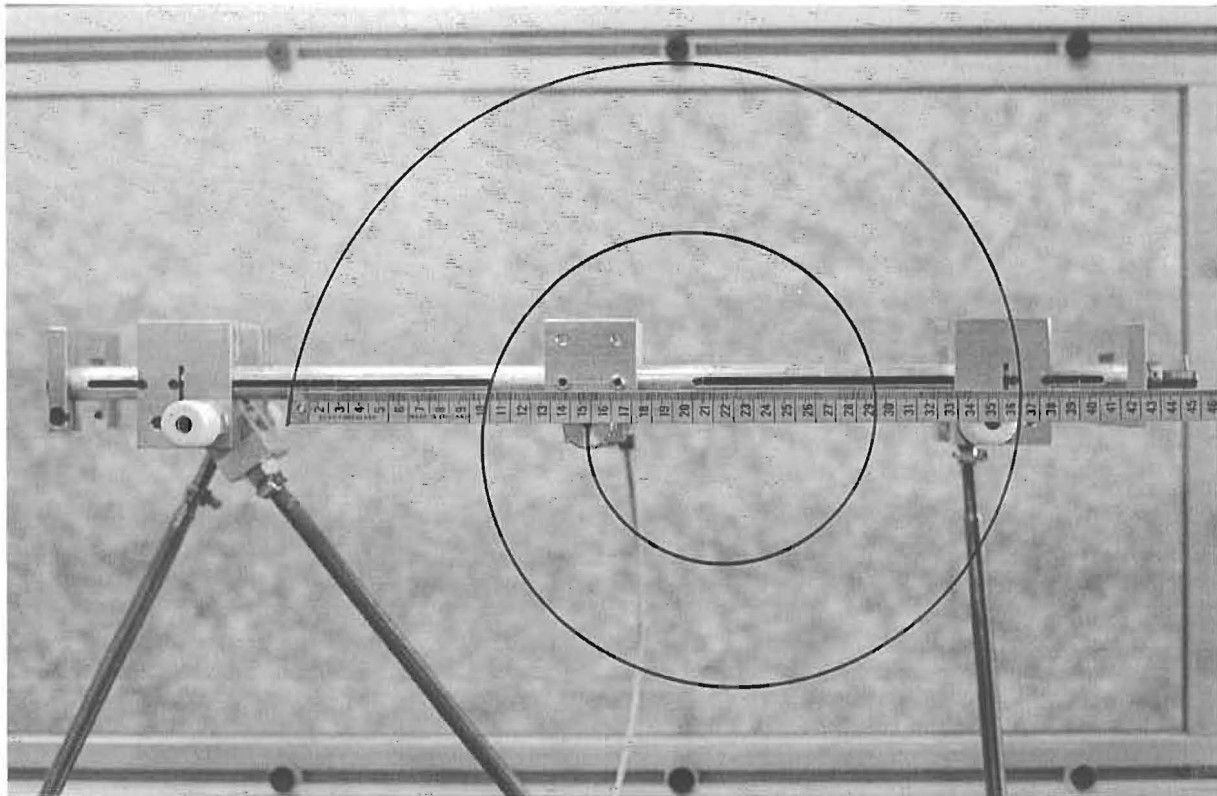


Figure 5.24: Close-up view of the executed spiral tool path.

5.6 Treble clef tool path

5.6.1 Nodal points and orientation angle

The treble clef tool path used here is a scaled version of the treble clef test curve of Section 3.5.5. Figure 5.25 shows the 49 scaled nodal points generated with a scale factor of 0.00285.

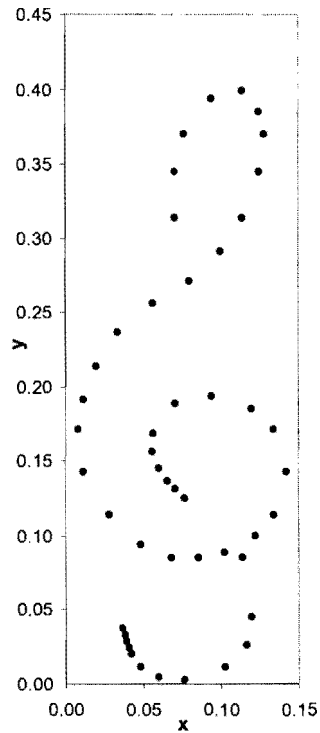


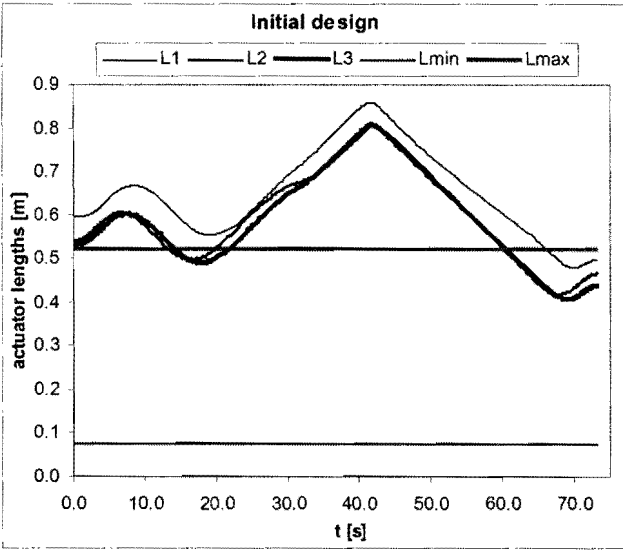
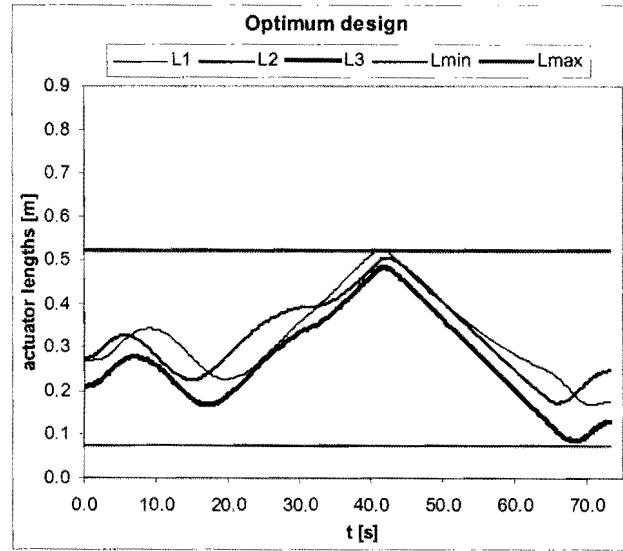
Figure 5.25: Nodal points used to approximate the treble clef tool path.

The OCAS trajectory-planning methodology is again utilized here with the specification of $\ddot{s}_{\text{ALLOW}} = 0.01 \text{ m/s}^2$, $v^* = 1.0 \text{ m/min}$ and $n_{\text{time}} = 5$, resulting in a total motion time along the treble clef tool path of 73.28 seconds.

The treble clef tool path is also traced with a fixed moving platform orientation $\phi_1 \equiv 0$.

5.6.2 Optimization results

The initial and optimum test-model designs for the treble clef tool path are compared in Table 5.9.

Initial design		Optimum design	
$\mathbf{X}^0 = [0.4, 0.4, -0.4, -0.4, 0.2]^T$		$\mathbf{X}^* = [0.42327, 0.34561, -0.08380, -0.30386, 0.25886]^T$	
Inequality constraint values (see Section D.3):			
$C_1(\mathbf{X}^0) = -0.05$ $C_3(\mathbf{X}^0) = -0.065$ $C_5(\mathbf{X}^0) = -0.07$ $\rightarrow C_7(\mathbf{X}^0) = 0.33349$ $\rightarrow C_9(\mathbf{X}^0) = 0.28228$ $C_{11}(\mathbf{X}^0) = -0.32755$ $C_{13}(\mathbf{X}^0) = -0.0425$ $C_{15}(\mathbf{X}^0) = -0.07431$ $C_{17}(\mathbf{X}^0) = -0.11291$ $C_{19}(\mathbf{X}^0) = -0.09483$ $C_{21}(\mathbf{X}^0) = -0.11013$	$C_2(\mathbf{X}^0) = -0.3$ $C_4(\mathbf{X}^0) = -0.287$ $C_6(\mathbf{X}^0) = -0.087$ $\rightarrow C_8(\mathbf{X}^0) = 0.27978$ $C_{10}(\mathbf{X}^0) = -0.32755$ $C_{12}(\mathbf{X}^0) = -0.39335$ $C_{14}(\mathbf{X}^0) = -0.05377$ $C_{16}(\mathbf{X}^0) = -0.07656$ $C_{18}(\mathbf{X}^0) = -0.10447$ $C_{20}(\mathbf{X}^0) = -0.12035$ $C_{22}(\mathbf{X}^0) = -0.07064$	$C_1(\mathbf{X}^*) = -0.02673$ $C_3(\mathbf{X}^*) = -0.11939$ $C_5(\mathbf{X}^*) = -0.01114$ $\Rightarrow C_7(\mathbf{X}^*) = 0.221 \times 10^{-5}$ $C_9(\mathbf{X}^*) = -0.04101$ $C_{11}(\mathbf{X}^*) = -0.01136$ $C_{13}(\mathbf{X}^*) = -0.07261$ $C_{15}(\mathbf{X}^*) = -0.03426$ $C_{17}(\mathbf{X}^*) = -0.03052$ $C_{19}(\mathbf{X}^*) = -0.07222$ $C_{21}(\mathbf{X}^*) = -0.13874$	$C_2(\mathbf{X}^*) = -0.32327$ $C_4(\mathbf{X}^*) = -0.23261$ $C_6(\mathbf{X}^*) = -0.14586$ $C_8(\mathbf{X}^*) = -0.01996$ $C_{10}(\mathbf{X}^*) = -0.01136$ $C_{12}(\mathbf{X}^*) = -0.33997$ $C_{14}(\mathbf{X}^*) = -0.00315$ $\Rightarrow C_{16}(\mathbf{X}^*) = -0.774 \times 10^{-6}$ $C_{18}(\mathbf{X}^*) = -0.00305$ $C_{20}(\mathbf{X}^*) = -0.04259$ $C_{22}(\mathbf{X}^*) = -0.04912$
\rightarrow constraint violation		\Rightarrow constraint active	
Variation of actuator leg lengths along the treble clef tool path:			
<p style="text-align: center;">Initial design</p> 		<p style="text-align: center;">Optimum design</p> 	
5(a)		5(b)	

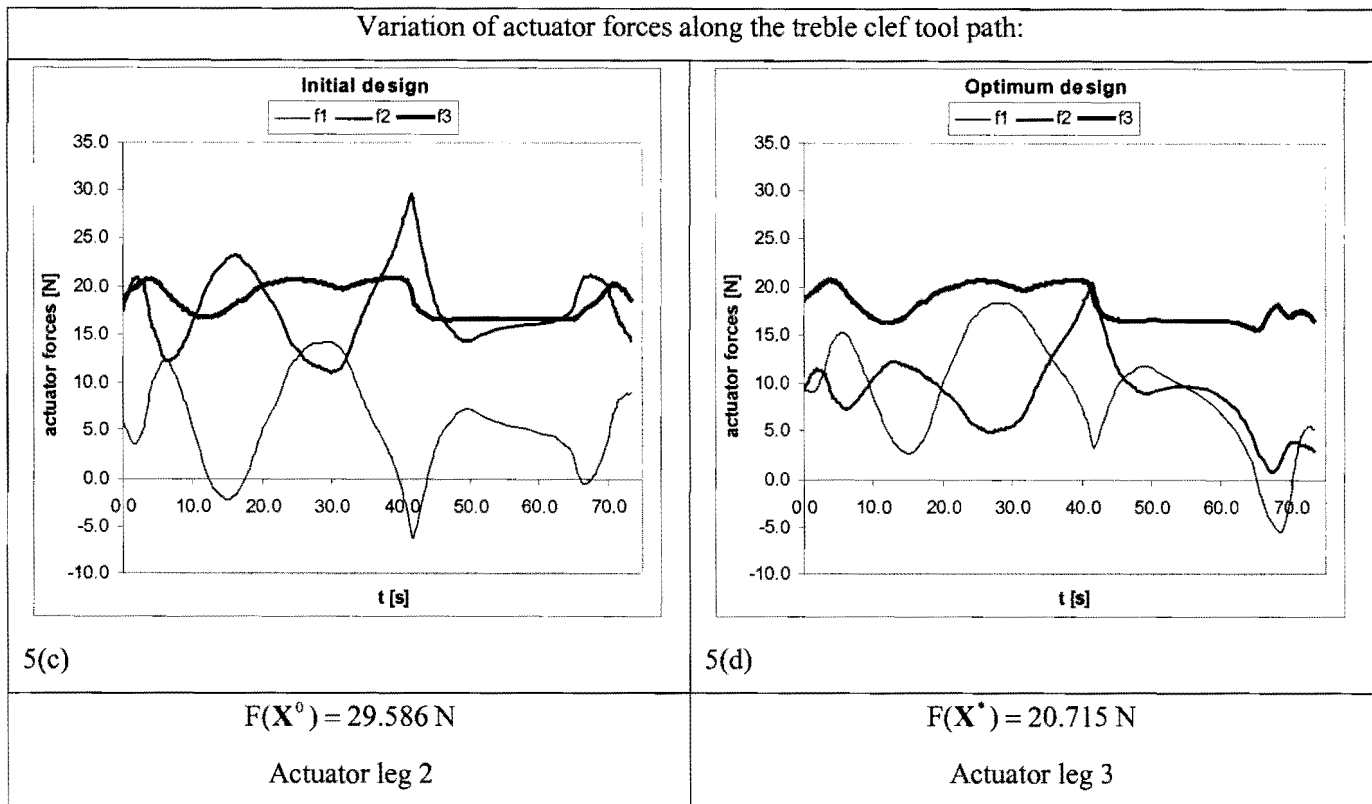


Table 5.9: Comparison between the initial and optimum designs for the treble clef tool path.

The initial design is *severely infeasible* (see the unallowable variations in actuator leg lengths shown in inset 5(a) and which correspond to the positive inequality constraint function values $C_7(\mathbf{X}^0)$, $C_8(\mathbf{X}^0)$ and $C_9(\mathbf{X}^0)$). The optimum and *feasible* (see inset 5(b)) design \mathbf{X}^* with *active* inequality constraints corresponding to C_7 and C_{16} , and a level maximum magnitude actuator force distribution (see inset 5(d)) is found in 127 optimization iterations and utilizing 6 minutes and 57 seconds computational time on a Pentium IV 1.5 GHz computer with 640 MB DDRAM. Once again, LFOPC terminated on criterion 2 ($\epsilon_x \leq 10^{-5}$) listed in Section 4.4.

5.6.3 Analysis of convergence to optimum

Figure 5.26 shows the convergence history of the objective function.

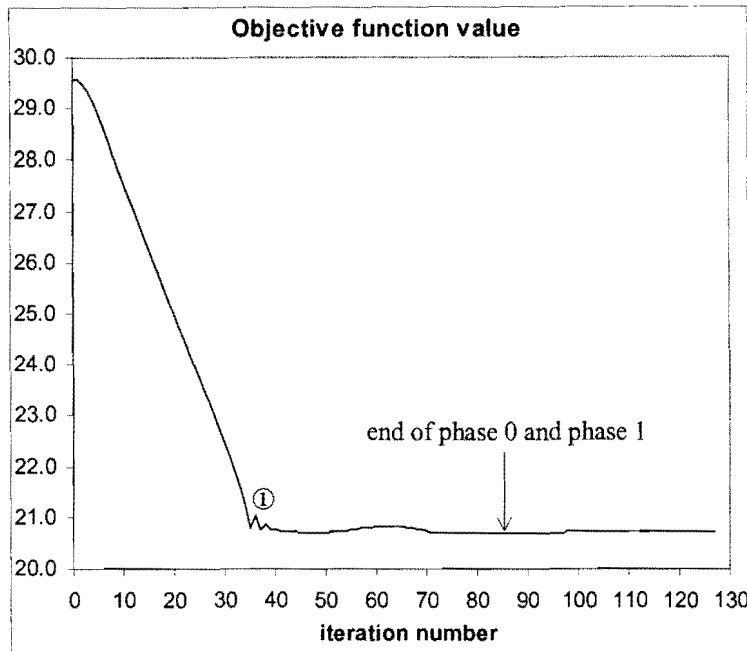


Figure 5.26: Convergence history of the objective function for the treble clef tool path.

The relatively smooth convergence graph of the objective function value shown in Figure 5.26 relates the LFOPC phases, actuator leg responsible for the maximum magnitude actuator force, and violated inequality constraints as indicated in Table 5.10.

Labels	Iteration No.	LFOPC-Phase	Act. leg	Violated Inequality Constraints
X^0	0	0	ℓ_2	C_7 C_8 C_9
①	35	0	ℓ_2	C_7 C_{14} C_{15} C_{16} C_{18}
	36	0	ℓ_2	C_7 C_{14} C_{16} C_{18}
	37	0	ℓ_3	C_7 C_{14} C_{15} C_{16} C_{18}
	38	0	ℓ_2	C_7 C_{14} C_{15} C_{16} C_{18}
	39	0	ℓ_3	C_7 C_{14} C_{15} C_{16} C_{18}
	40	0	ℓ_3	C_7 C_{14} C_{16} C_{18} maximum violated constraint value $C_{18}(X^{40}) = 0.02568$
	41	0	ℓ_3	C_7 C_{14} C_{16} C_{18}

LFOPC phase- changes	84	0	ℓ_3	C_7	C_{16}
	85	0	ℓ_3	C_7	C_{16}
	85	1	ℓ_3	maximum violated constraint value $C_{16}(\mathbf{X}^{85}) = 0.00220$	
	86	1	ℓ_3	C_7	C_{16}
	86	2	ℓ_3	C_7	C_{16}
	87	2	ℓ_3	C_7	C_{16}
\mathbf{X}^*	127	2	ℓ_3	C_7	C_{16} (active)

Table 5.10: Comparative table for the treble clef tool path objective function vs. iteration number curve (see Figure 5.26).

Note that a switch from ℓ_2 to ℓ_3 as the actuator leg responsible for the maximum magnitude actuator force occurs in the vicinity of label ①.

The convergence histories of the respective design variables X_i , $i = 1, 2, \dots, 5$ are shown in Figure 5.27. Here the convergence of the design variables is significantly more sluggish, requiring about 100 iterations to converge, compared to the relatively fast and sharp convergence of the objective function value within 40 iterations. Even though, after 40 iterations the objective function value ($F(\mathbf{X}^{40}) = 20.747 \text{ N}$) is close to the optimum objective function value ($F(\mathbf{X}^*) = 20.715 \text{ N}$), the maximum violated constraint function value, $C_{18}(\mathbf{X}^{40}) = 0.02568 \text{ m}$, shows that this is still an infeasible design due to the occurrence of mechanical interference (see expression (D.19)). The corresponding values of the design variables are $\mathbf{X}^{40} = [0.41543, 0.39816, -0.08308, -0.33817, 0.21923]^T$. Significant further changes occur in the values of design variables X_2 , X_4 and X_5 between iterations 40 and 100 ($\mathbf{X}^{100} = [0.42319, 0.34551, -0.08406, -0.30402, 0.25886]^T$). However, after phase 0 of the LFOPC-algorithm has terminated (iteration number 85), the maximum violated constraint function value is only 2.20 mm ($C_{16}(\mathbf{X}^{85}) = 0.00220 \text{ m}$), which is negligible for all practical purposes and \mathbf{X}^{85} may be taken as an effective optimum design.

LFOPC phase- changes	84	0	ℓ_3	C_7	C_{16}
	85	0	ℓ_3	C_7	C_{16}
	85	1	ℓ_3	C_7	C_{16}
	86	1	ℓ_3	C_7	C_{16}
	86	2	ℓ_3	C_7	C_{16}
	87	2	ℓ_3	C_7	C_{16}
\mathbf{X}^*	127	2	ℓ_3	C_7	C_{16} (active)

Table 5.10: Comparative table for the treble clef tool path objective function vs. iteration number curve (see Figure 5.26).

Note that a switch from ℓ_2 to ℓ_3 as the actuator leg responsible for the maximum magnitude actuator force occurs in the vicinity of label ①.

The convergence histories of the respective design variables X_i , $i = 1, 2, \dots, 5$ are shown in Figure 5.27. Here the convergence of the design variables is significantly more sluggish, requiring about 100 iterations to converge, compared to the relatively fast and sharp convergence of the objective function value within 40 iterations. Even though, after 40 iterations the objective function value ($F(\mathbf{X}^{40}) = 20.747 \text{ N}$) is close to the optimum objective function value ($F(\mathbf{X}^*) = 20.715 \text{ N}$), the maximum violated constraint function value, $C_{18}(\mathbf{X}^{40}) = 0.02568 \text{ m}$, shows that this is still an infeasible design due to the occurrence of mechanical interference (see expression (D.19)). The corresponding values of the design variables are $\mathbf{X}^{40} = [0.41543, 0.39816, -0.08308, -0.33817, 0.21923]^T$. Significant further changes occur in the values of design variables X_2 , X_4 and X_5 between iterations 40 and 100 ($\mathbf{X}^{100} = [0.42319, 0.34551, -0.08406, -0.30402, 0.25886]^T$). However, after phase 0 of the LFOPC-algorithm has terminated (iteration number 85), the maximum violated constraint function value is only 2.20 mm ($C_{16}(\mathbf{X}^{85}) = 0.00220 \text{ m}$), which is negligible for all practical purposes and \mathbf{X}^{85} may be taken as an effective optimum design.

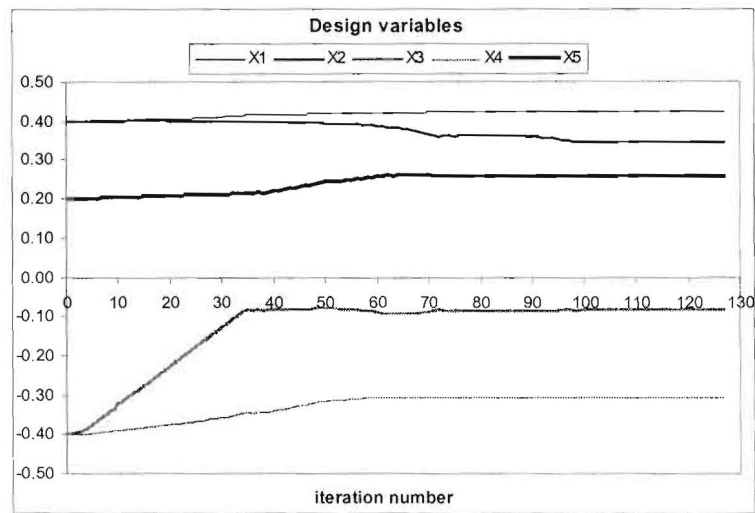


Figure 5.27: Convergence histories of design variables X_i , $i = 1, 2, \dots, 5$ for the treble clef tool path.

5.6.4 Execution of the treble clef tool path.

The four photographs grouped in Figure 5.28 were taken at different time instants along the actually traced treble clef tool path. Note that the moving platform remains horizontal ($\phi_1 \equiv 0$) during the execution of the path.

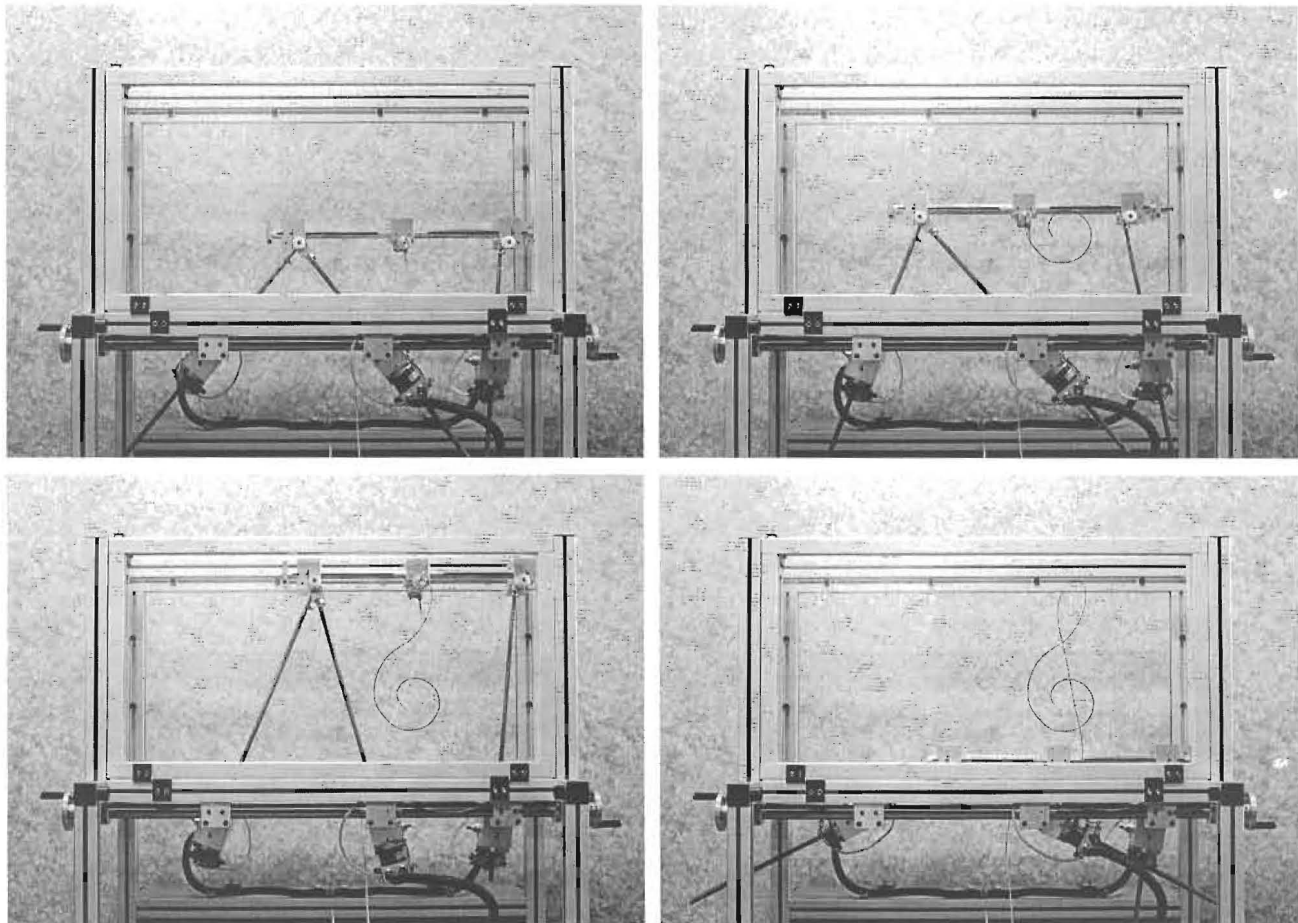


Figure 5.28: Execution of the treble clef tool path.

A close-up view of the executed treble clef tool path is shown in Figure 5.29, for comparison with the prescribed nodal points shown in Figure 5.25. Clearly the path is accurately traced with no practically significant differences in size and proportion between the executed and prescribed tool paths.

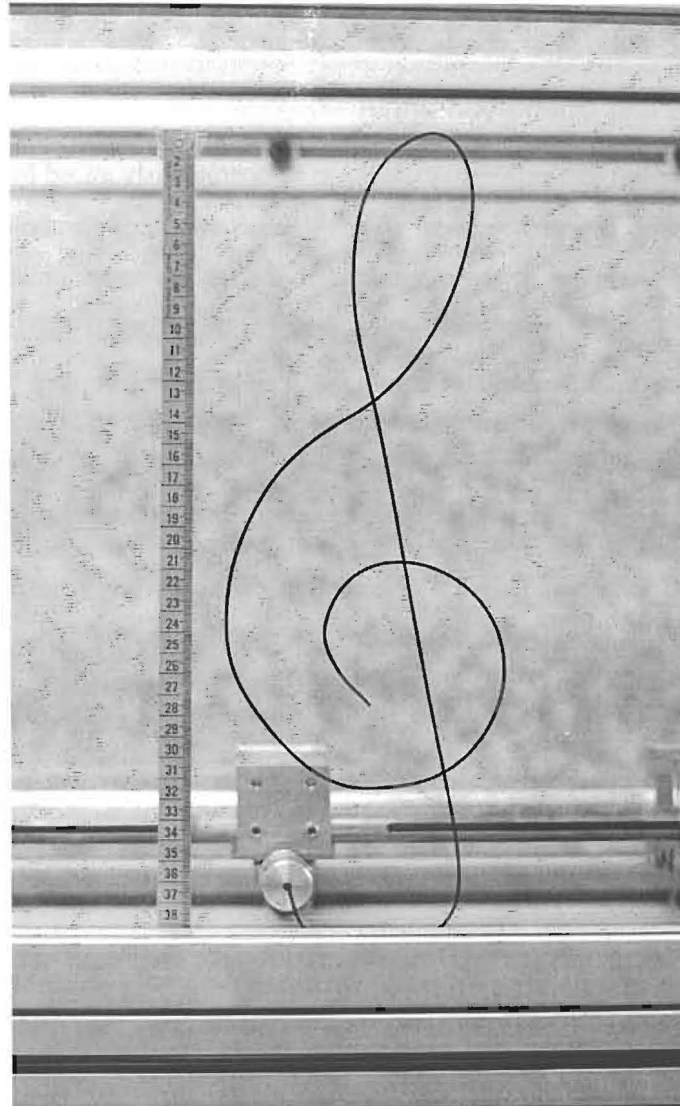


Figure 5.29: Close-up view of the executed treble clef tool path.

5.7 Bigger parabolic tool path

All of the above tool paths are scaled down versions of those represented by the original test functions discussed in Section 3.5. In each instance, the proposed optimization approach determined a feasible design of the adjustable planar machine, with which the (scaled) prescribed tool path could be *continuously* traced. In general, however, a feasible design may not exist for a particular prescribed path, and thus it cannot be continuously traced. In this event, *user intervention* is required to divide the

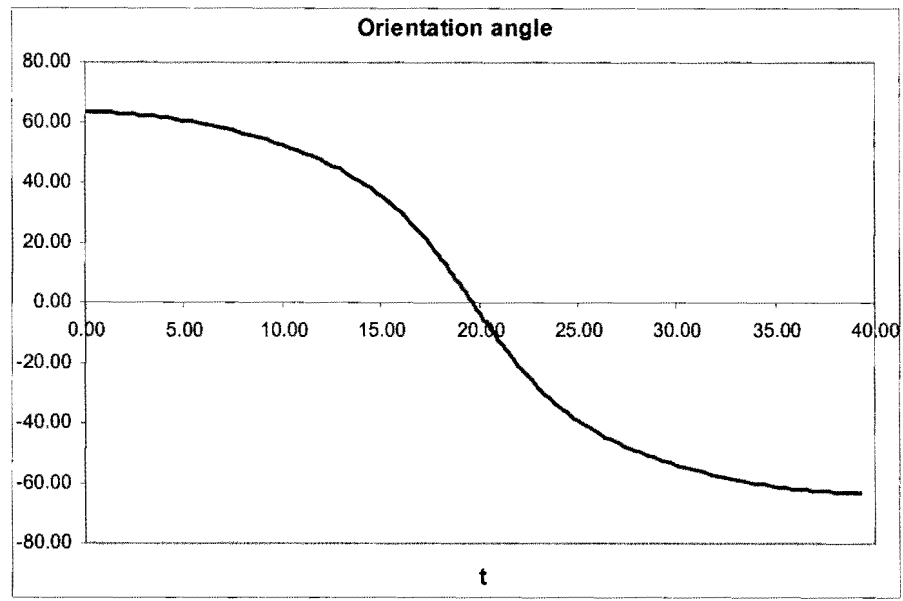


Figure 5.31: Variation in the orientation angle for the bigger parabolic tool path.

5.7.1.2 Optimization results

Whenever the LFOPC-algorithm cannot find an optimum design that is feasible, it computes a “best” *compromised* design corresponding to that with least possible constraint violation, and presents it as the optimum solution. A comparison between the initial test-model design and the compromised optimum test-model design for the bigger parabolic prescribed tool path is given in Table 5.11, with figure insets 6(a) – 6(d).

Initial design		Optimum compromised design	
$\mathbf{X}^0 = [0.4, 0.4, -0.4, -0.4, 0.2]^T$		$\mathbf{X}^* = [0.09643, 0.11018, -0.51561, -0.10841, 0.11015]^T$	
Inequality constraint values (see Section D.3):			
$C_1(\mathbf{X}^0) = -0.05$	$C_2(\mathbf{X}^0) = -0.3$	$C_1(\mathbf{X}^*) = -0.35357$	$\rightarrow C_2(\mathbf{X}^*) = 0.00357$
$C_3(\mathbf{X}^0) = -0.065$	$C_4(\mathbf{X}^0) = -0.287$	$C_3(\mathbf{X}^*) = -0.35482$	$\rightarrow C_4(\mathbf{X}^*) = 0.00282$
$C_5(\mathbf{X}^0) = -0.07$	$C_6(\mathbf{X}^0) = -0.087$	$C_5(\mathbf{X}^*) = -0.15985$	$\rightarrow C_6(\mathbf{X}^*) = 0.00285$
$\rightarrow C_7(\mathbf{X}^0) = 0.11077$	$C_8(\mathbf{X}^0) = -0.02581$	$\rightarrow C_7(\mathbf{X}^*) = 0.01264$	$\rightarrow C_8(\mathbf{X}^*) = 0.591 \times 10^{-3}$
$C_9(\mathbf{X}^0) = -0.00648$	$\rightarrow C_{10}(\mathbf{X}^0) = 0.12769$	$\rightarrow C_9(\mathbf{X}^*) = 0.01347$	$\rightarrow C_{10}(\mathbf{X}^*) = 0.01208$
$\rightarrow C_{11}(\mathbf{X}^0) = 0.12769$	$C_{12}(\mathbf{X}^0) = -0.29548$	$\rightarrow C_{11}(\mathbf{X}^*) = 0.01208$	$C_{12}(\mathbf{X}^*) = -0.36166$
$C_{13}(\mathbf{X}^0) = -0.09548$	$\rightarrow C_{14}(\mathbf{X}^0) = 0.02800$	$C_{13}(\mathbf{X}^*) = -0.16520$	$C_{14}(\mathbf{X}^*) = -0.05061$
$\rightarrow C_{15}(\mathbf{X}^0) = 0.03046$	$\rightarrow C_{16}(\mathbf{X}^0) = 0.04159$	$C_{15}(\mathbf{X}^*) = -0.29681$	$C_{16}(\mathbf{X}^*) = -0.04946$
$\rightarrow C_{17}(\mathbf{X}^0) = 0.05454$	$\rightarrow C_{18}(\mathbf{X}^0) = 0.08839$	$C_{17}(\mathbf{X}^*) = -0.00670$	$C_{18}(\mathbf{X}^*) = -0.04160$
$C_{19}(\mathbf{X}^0) = -0.03549$	$C_{20}(\mathbf{X}^0) = -0.02495$	$C_{19}(\mathbf{X}^*) = -0.05005$	$C_{20}(\mathbf{X}^*) = -0.13960$
$\rightarrow C_{21}(\mathbf{X}^0) = 0.06468$	$\rightarrow C_{22}(\mathbf{X}^0) = 0.04873$	$C_{21}(\mathbf{X}^*) = -0.04202$	$C_{22}(\mathbf{X}^*) = -0.17053$
\rightarrow constraint violation		\rightarrow constraint violation	

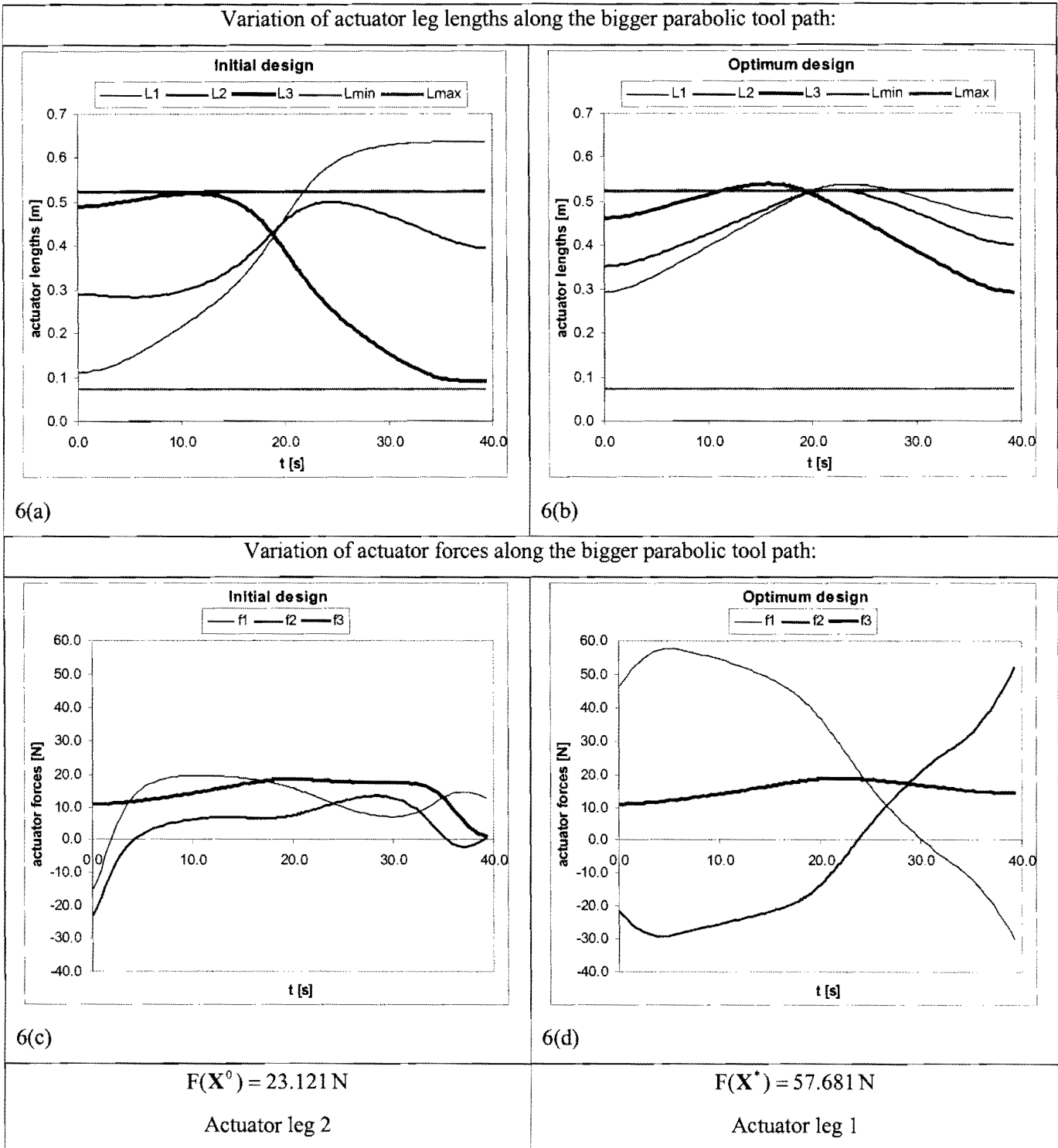


Table 5.11: Comparison between the initial and optimum designs for the bigger parabolic tool path.

The infeasibility of the initial design \mathbf{X}^0 is evident from figure inset 6(a), as well as from the violated inequality constraints corresponding to $C_7, C_{10}, C_{11}, C_{14}, C_{15}, C_{16}, C_{17}, C_{18}, C_{21}$ and C_{22} . Figure inset 6(c) shows the variation in actuator forces for this initial design with an objective function value of $F(\mathbf{X}^0) = 23.121 \text{ N}$, with actuator leg 2 responsible for the maximum magnitude actuator force.

Considering the compromised optimum design \mathbf{X}^* , the constraints corresponding to C_2 , C_4 , C_6 , C_7 , C_8 , C_9 , C_{10} and C_{11} are violated by the LFOPC-algorithm in its search for a best compromised solution. The variation of the actuator legs for this compromised optimum solution is shown in figure inset 6(b), where the violation of the maximum allowable actuator leg length by actuator legs ℓ_1 and ℓ_3 is clearly visible. In correspondence with Section 5.4.2, the magnitude of constraint function value $C_8(\mathbf{X}^*) = 0.591 \times 10^{-3} \text{ m}$ (0.591 mm) is indeed negligibly small, and from a practical point of view, the inequality constraint associated with C_8 can be considered *active* rather than *violated* (see expression (D.11)).

The violated inequality constraints associated with C_2 , C_4 and C_6 (expression (D.10)) imply that the linearly adjustable revolute joints are positioned outside their allowable ranges. In particular, C_2 has the largest constraint function magnitude of the three with $C_2(\mathbf{X}^*) = 0.00357 \text{ m} = 3.57 \text{ mm}$. Although substantial, these violations are not critical, since they lie within the minimum safety margin of 5 mm that was used during the formulation of the inequality constraints (see **Appendix D**).

Apart from the critically violated actuator leg length inequality constraints C_7 and C_9 (expression (D.11)), violated constraints C_{10} and C_{11} resulting from the tangential orientation of the moving platform, cannot be ignored. More specifically, of these four inequality constraint functions, the smallest magnitude is $C_{10}(\mathbf{X}^*) = C_{11}(\mathbf{X}^*) = 0.0121 \text{ m}$ (12.1 mm) and the largest magnitude is $C_9(\mathbf{X}^*) = 0.0135 \text{ m}$ (13.5 mm).

The above analysis of the violated inequality constraints is used in the next subsection where the prescribed parabolic tool path is rationally divided into different segments. For the sake of completeness, however, the convergence histories of the objective function (Figure 5.32) and design variables (Figure 5.33) in arriving at the compromised solution, are also included here.

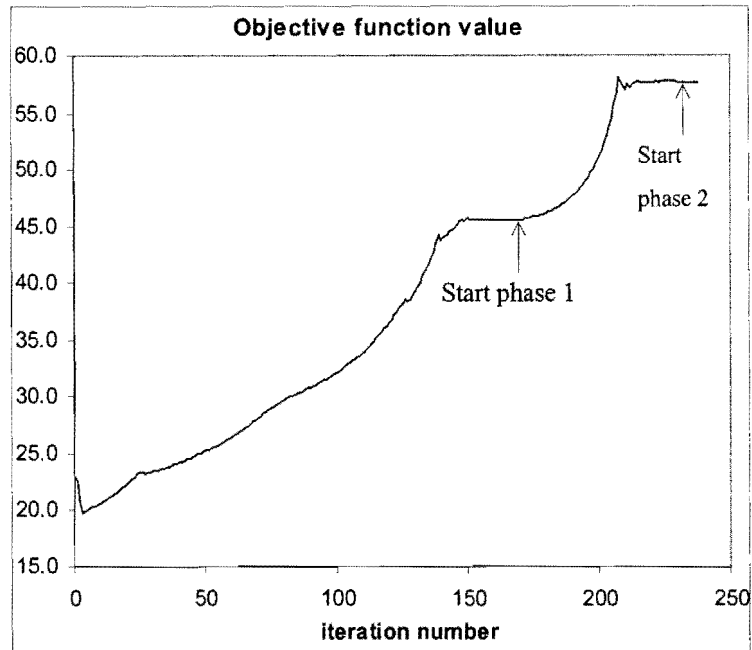


Figure 5.32: Convergence history of the objective function for the bigger parabolic tool path.

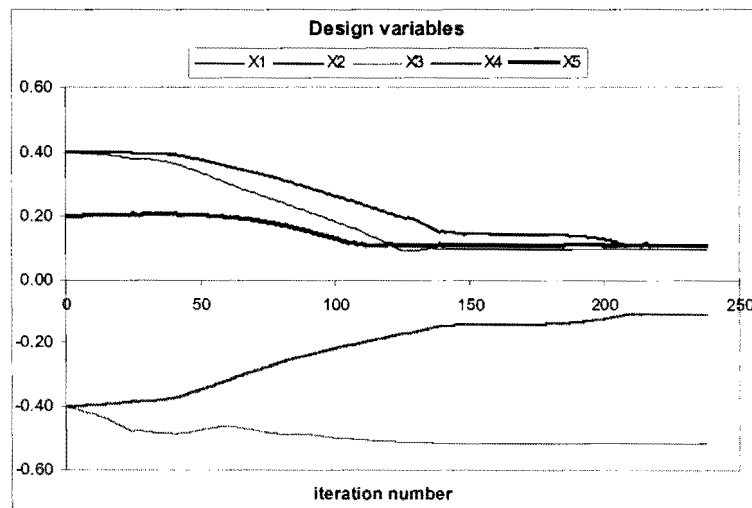


Figure 5.33: Convergence histories of design variables X_i , $i = 1, 2, \dots, 5$ for the bigger parabolic tool path.

Note that the compromised optimum solution \mathbf{X}^* is found in 238 optimization iterations requiring 7 minutes and 29 seconds computational time on a Pentium IV 1.5GHz computer with 640 MB DDRAM. The LFOPC-algorithm here also terminated on criterion 2 ($\epsilon_x \leq 10^{-5}$) listed in Section 4.4.

5.7.2 Dividing the prescribed path into segments

5.7.2.1 Nodal points and orientation angle

In the case of a compromised solution the user may intervene in a rational manner in order to execute the path. This is done by firstly analyzing the constraints violated by the compromised design. Note that for the example under consideration, the critically violated inequality constraints are the maximum allowable actuator leg lengths ℓ_1 and ℓ_3 (C_7 and C_9 , given by expression (D.11)) and the lower frame boundary constraints C_{10} and C_{11} as explained in Section D.3.3.2. This implies that the “vertical motion” of the moving platform that is required for the complete continuous tracing of the prescribed parabolic tool path shown in Figure 5.30, cannot be accommodated.

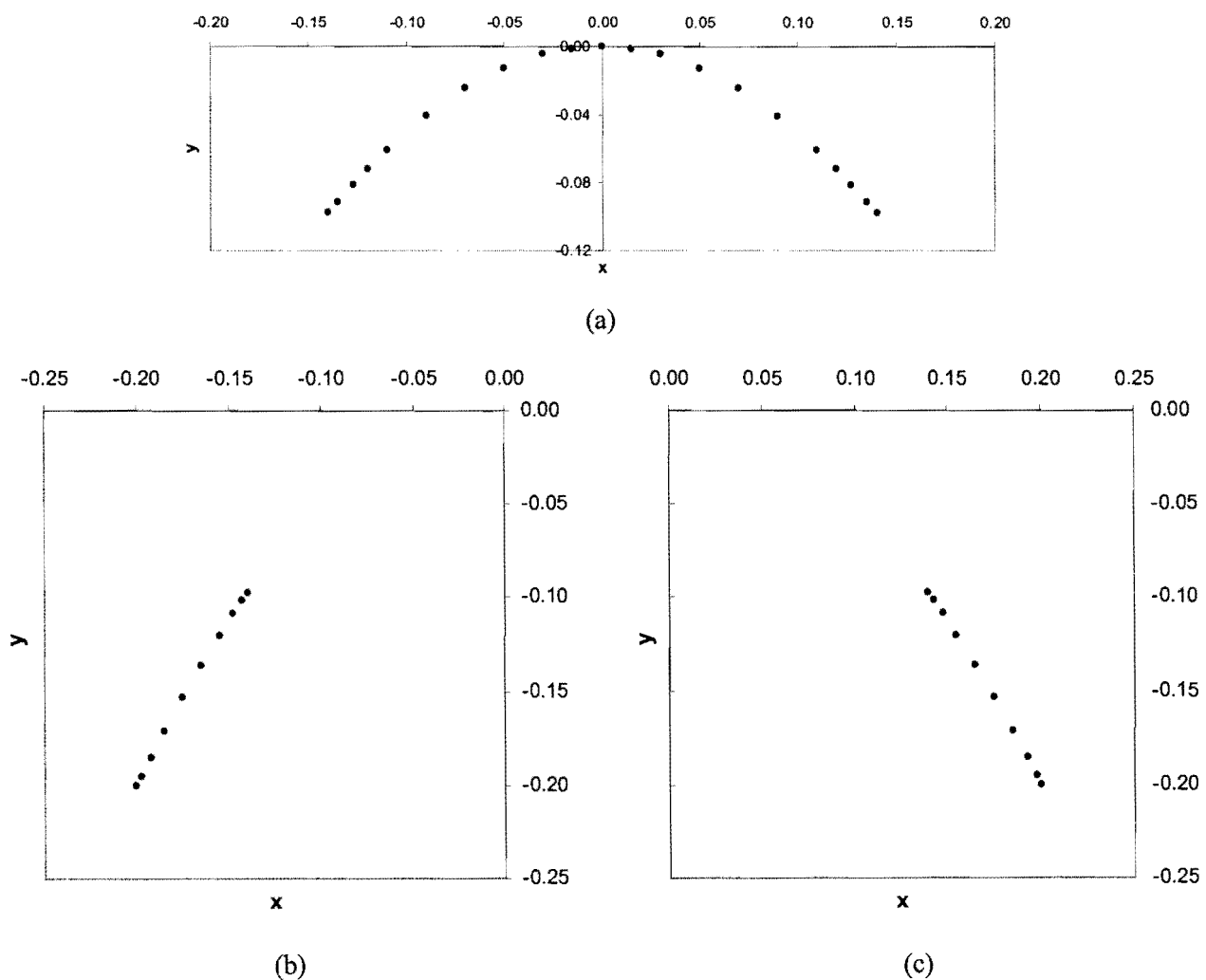


Figure 5.34: Three sets of nodal points used to approximate the bigger parabolic tool path: (a) upper middle segment, (b) bottom left segment and (c) bottom right segment.

The prescribed parabolic tool path is symmetric about the y-axis, hence the “bounds of vertical motion”, associated with the execution of the left-hand side of the tool path correspond exactly to the “bounds of vertical motion” associated with the execution of the right-hand side of the tool path. This implies that

dividing the prescribed parabolic tool path into two symmetric segments, will not remedy the problem. An alternative strategy is to divide the prescribed tool path into three separate segments as shown in Figure 5.34 (a) – (c).

The sequential execution of firstly segment (b), then segment (a) and finally segment (c), is one possible strategy that can be followed to execute the prescribed bigger parabolic tool path. The assumption is made here that the workpiece can be repositioned after each segment is executed. This assumption is justified not only because repositioning is common practice in the machining of larger workpieces, but also because the two “repositioning parameters” correspond to chosen design variables of the constrained optimization problem. In particular, design variables X_3 and X_4 determine the position of the workpiece relative to the base of the planar Gough-Stewart machining platform (see Figure 5.5).

For demonstration purposes it is further assumed that the planar “workpiece” on which the prescribed tool path is to be traced, can be rotated through 180° about the vertical y-axis of the prescribed parabola. This assumption implies that a second possible strategy for the execution of the prescribed bigger parabolic tool path, is to sequentially trace segments (b) and (a) of Figure 5.34, then rotate the workpiece through 180° about its vertical symmetry axis, and finally trace segment (b) of Figure 5.34 once more.

The advantage of the latter strategy is that for the optimization based operating system of the planar Gough-Stewart platform as proposed in this study, only two of the three segments shown in Figure 5.34 have to be optimized for. In practice segments (b) and (a) are treated as two separate tool paths, each requiring its own optimization run. The subsequent optimization results of the respective prescribed tool paths are presented in sub-sections 5.7.2.2 and 5.7.2.3.

For both prescribed tool paths, the OCAS trajectory-planning methodology (**Chapter 3**) is applied with the maximum allowable acceleration limited to 0.01 meter per second square ($\ddot{s}_{\text{allow}} = 0.01 \text{ m/s}^2$), and a specified cutting speed of 1.0 m/min ($v^* = 1.0 \text{ m/min}$). With these specifications, the *simulated* prescribed motion along segment (b) in Figure 5.34 is completed in 10.07 s, and the *simulated* prescribed motion along segment (a) in Figure 5.34 is completed in 24.16 s.

The original specification that the moving platform of the test-model be tangentially orientated with respect to the prescribed curve, is also incorporated here. In particular, the moving platform orientation angle now varies from 63.4° at the starting point $(-0.2, -0.2)$ of segment (b) to 54.5° at the end point $(-0.14, -0.098)$ of segment (b) as shown in Figure 5.35.

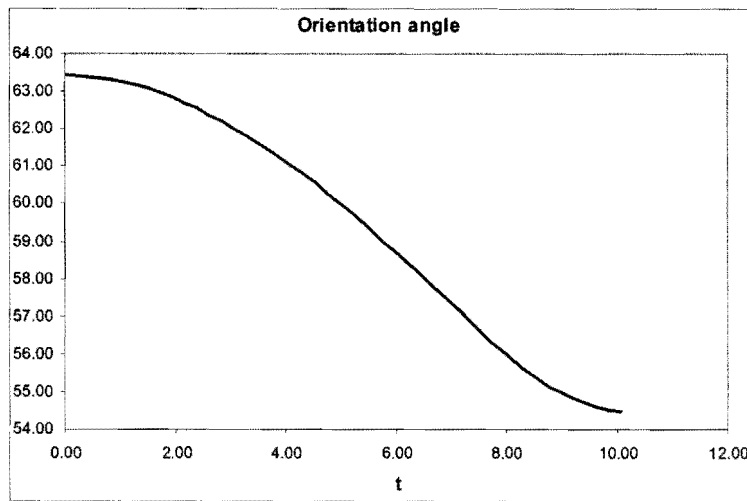


Figure 5.35: Variation in the orientation angle for segment (b) of the bigger parabolic tool path (see Figure 5.34).

For segment (a) in Figure 5.34, the moving platform orientation angle varies from 54.5° at the start point $(-0.14, -0.098)$, to -54.5° at the end point $(0.14, -0.098)$ (see Figure 5.36).

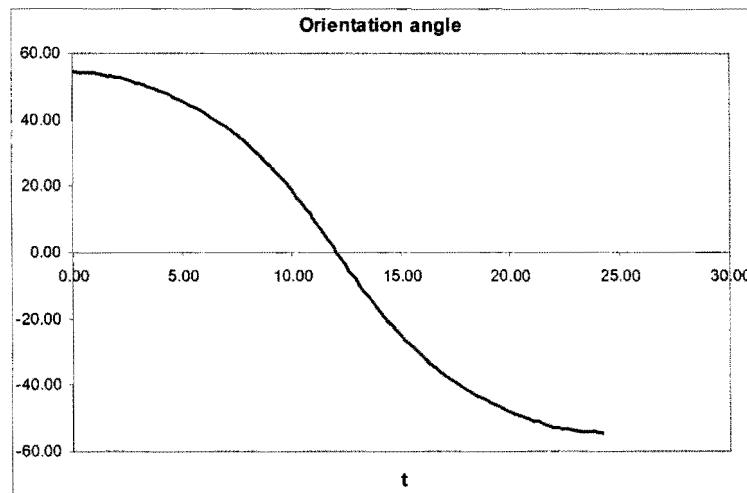


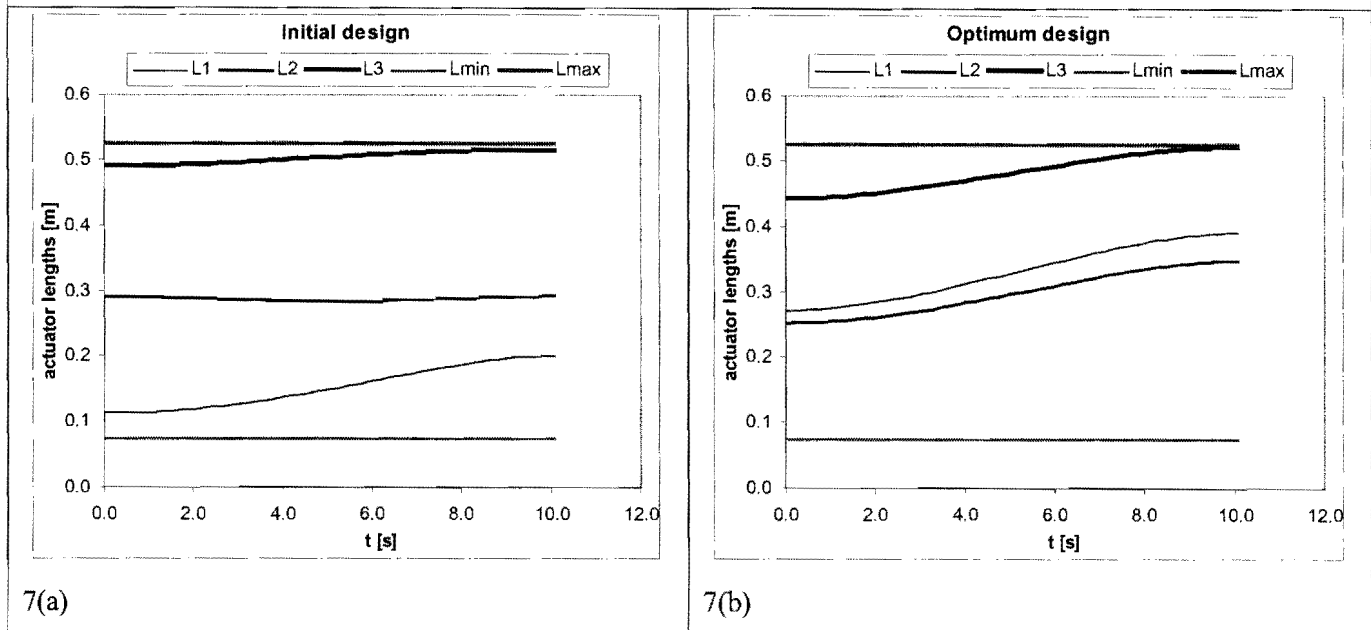
Figure 5.36: Variation in the orientation angle for segment (a) of the bigger parabolic tool path (see Figure 5.34).

5.7.2.2 Optimization results for segment (b) of Figure 5.34.

A comparison between the initial test-model design and the optimum test-model design for segment (b) of the bigger parabolic tool path (see Figure 5.34) is given in Table 5.12 with figure insets 7(a) – 7(d).

Initial design		Optimum compromised design	
$\mathbf{X}^0 = [0.4, 0.4, -0.4, -0.4, 0.2]^T$		$\mathbf{X}^* = [0.21606, 0.23581, -0.52924, -0.38758, 0.11917]^T$	
Inequality constraint values (see Section D.3):			
$C_1(\mathbf{X}^0) = -0.05$	$C_2(\mathbf{X}^0) = -0.3$	$C_1(\mathbf{X}^*) = -0.23394$	$C_2(\mathbf{X}^*) = -0.11606$
$C_3(\mathbf{X}^0) = -0.065$	$C_4(\mathbf{X}^0) = -0.287$	$C_3(\mathbf{X}^*) = -0.22919$	$C_4(\mathbf{X}^*) = -0.12281$
$C_5(\mathbf{X}^0) = -0.07$	$C_6(\mathbf{X}^0) = -0.087$	$C_5(\mathbf{X}^*) = -0.15083$	$C_6(\mathbf{X}^*) = -0.00617$
$C_7(\mathbf{X}^0) = -0.32486$	$C_8(\mathbf{X}^0) = -0.23336$	$C_7(\mathbf{X}^*) = -0.13510$	$C_8(\mathbf{X}^*) = -0.17790$
$C_9(\mathbf{X}^0) = -0.00911$	$\rightarrow C_{10}(\mathbf{X}^0) = 0.12770$	$C_9(\mathbf{X}^*) = -0.00394$	$C_{10}(\mathbf{X}^*) = -0.00154$
$C_{11}(\mathbf{X}^0) = -0.38212$	$C_{12}(\mathbf{X}^0) = -0.29556$	$C_{11}(\mathbf{X}^*) = -0.51136$	$C_{12}(\mathbf{X}^*) = -0.48845$
$C_{13}(\mathbf{X}^0) = -0.40876$	$\rightarrow C_{14}(\mathbf{X}^0) = 0.02801$	$C_{13}(\mathbf{X}^*) = -0.31045$	$C_{14}(\mathbf{X}^*) = -0.06274$
$\rightarrow C_{15}(\mathbf{X}^0) = 0.03048$	$\rightarrow C_{16}(\mathbf{X}^0) = 0.04160$	$C_{15}(\mathbf{X}^*) = -0.22601$	$C_{16}(\mathbf{X}^*) = -0.07416$
$\rightarrow C_{17}(\mathbf{X}^0) = 0.05455$	$\rightarrow C_{18}(\mathbf{X}^0) = 0.08839$	$C_{17}(\mathbf{X}^*) = -0.03509$	$C_{18}(\mathbf{X}^*) = -0.05569$
$C_{19}(\mathbf{X}^0) = -0.04946$	$C_{20}(\mathbf{X}^0) = -0.06903$	$C_{19}(\mathbf{X}^*) = -0.08209$	$C_{20}(\mathbf{X}^*) = -0.18538$
$C_{21}(\mathbf{X}^0) = -0.05174$	$C_{22}(\mathbf{X}^0) = 0.04874$	$C_{21}(\mathbf{X}^*) = -0.06039$	$C_{22}(\mathbf{X}^*) = -0.01225$
\rightarrow constraint violation			

Variation of actuator leg lengths along segment (b) of the bigger parabolic tool path (see Figure 5.34):



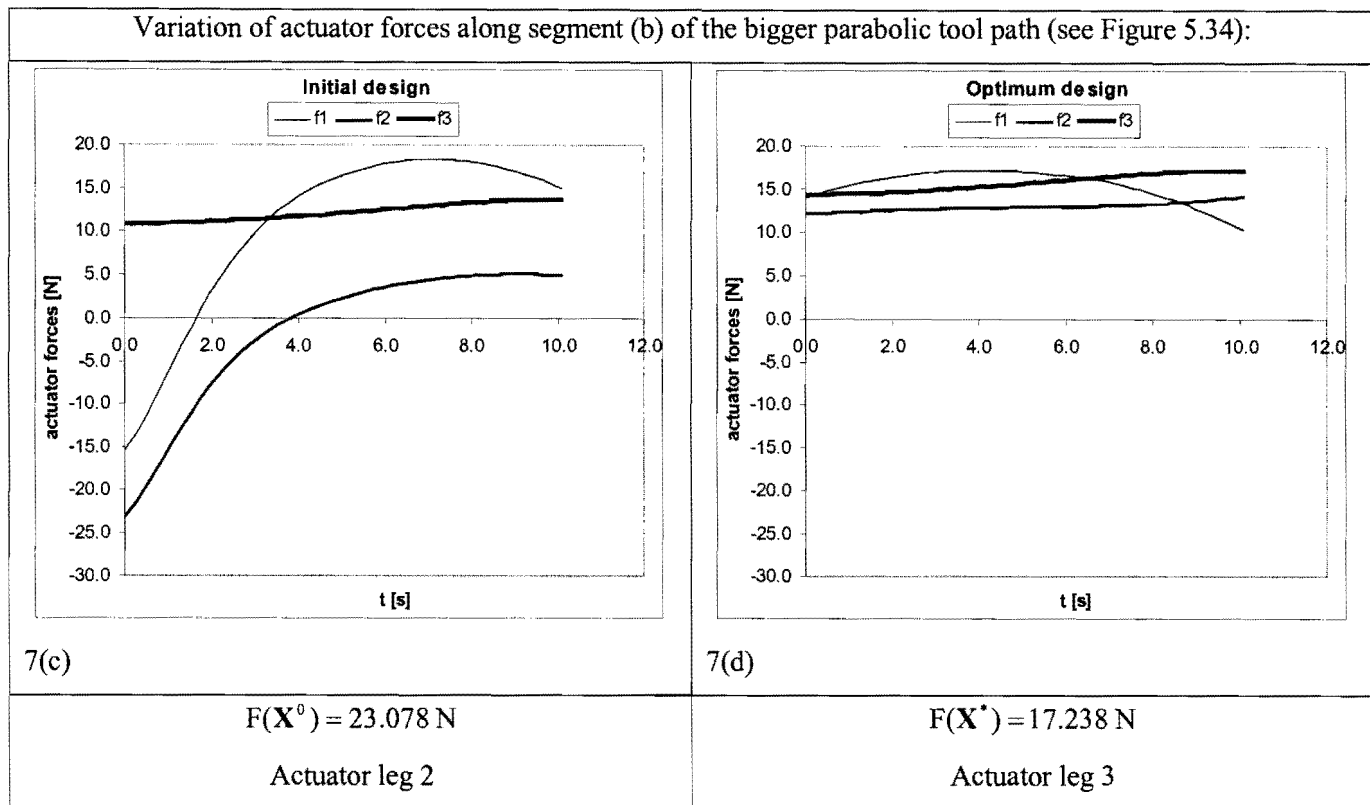


Table 5.12: Comparison between the initial and optimum designs for segment (b) of the bigger parabolic tool path (see Figure 5.34).

The initial design \mathbf{X}^0 is infeasible as can be seen from the positive inequality constraint function values $C_{10}(\mathbf{X}^0)$, $C_{14}(\mathbf{X}^0)$, $C_{15}(\mathbf{X}^0)$, $C_{16}(\mathbf{X}^0)$, $C_{17}(\mathbf{X}^0)$ and $C_{18}(\mathbf{X}^0)$ in Table 5.12. The (allowable) initial variation of the actuator leg lengths along segment (b) of the bigger parabolic tool path (see Figure 5.34) is shown in figure inset 7(a).

The LFOPC-optimization algorithm finds the feasible optimum design \mathbf{X}^* in 122 optimization iterations requiring 1 minute and 32 seconds computational time on a Pentium IV 1.5 GHz computer with 640 MB DDRAM.

The optimum design \mathbf{X}^* found is an *unconstrained* optimum as can be seen from the *negative* inequality constraint function values $C_i(\mathbf{X}^*)$, $i = 1, 2, 3, \dots, 22$ listed in Table 5.12, and the optimum variation of the actuator leg lengths shown in figure inset 7(b). The optimum variation of the actuator forces along segment (b) of the bigger parabolic tool path shown in figure inset 7(d) is significantly different when compared to the initial variation shown in figure inset 7(c). In particular, the initial objective function value is $F(\mathbf{X}^0) = 23.078 \text{ N}$ in actuator leg ℓ_2 , while the optimum objective function value is $F(\mathbf{X}^*) = 17.238 \text{ N}$ in actuator leg ℓ_3 .

The convergence histories of the objective function (Figure 5.37) and design variables (Figure 5.38) are shown below. Note that since no active constraints were identified as the LFOPC-algorithm progressed along phase 0 (see **Appendix C**), the iterative search terminated on criterion 2 ($\epsilon_x \leq 10^{-5}$) listed in Section 4.4 before the end of phase 0.

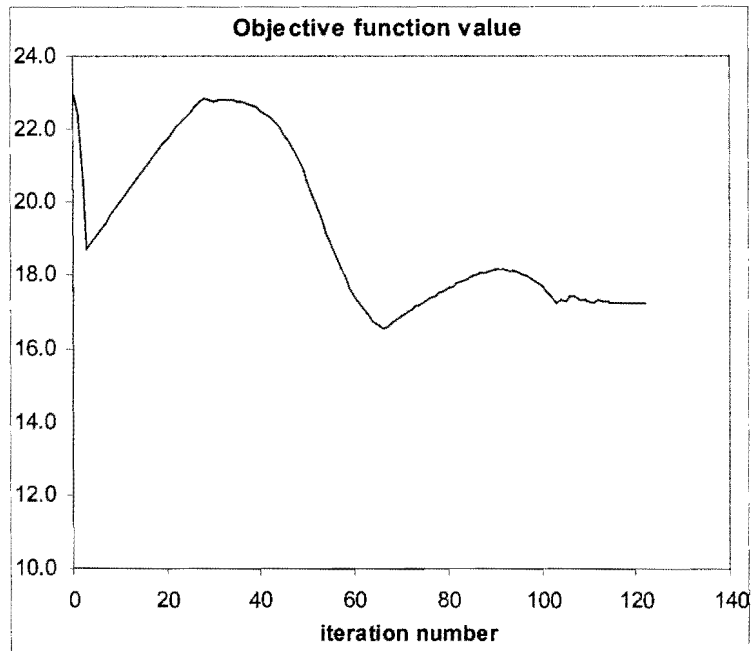


Figure 5.37: Convergence history of the objective function for segment (b) of the bigger parabolic tool path (see Figure 5.34).

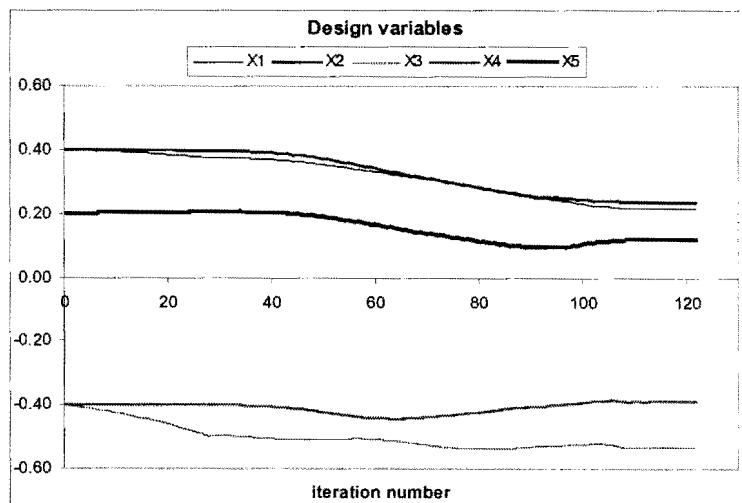
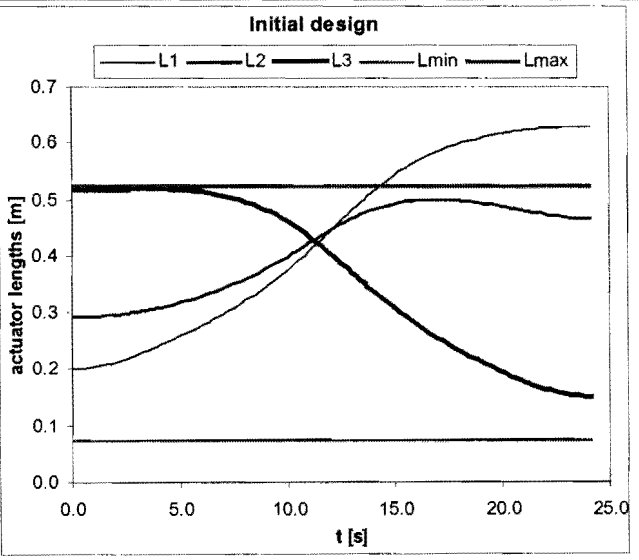
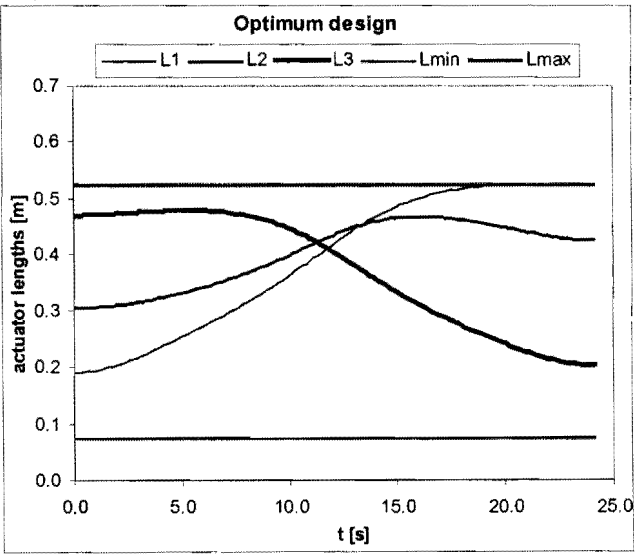


Figure 5.38: Convergence histories of design variables X_i , $i=1,2,\dots,5$ for segment (b) of the bigger parabolic tool path (see Figure 5.34).

5.7.2.3 Optimization results for segment (a) of Figure 5.34.

A comparison between the initial test-model design and the optimum test-model design for segment (a) of the bigger parabolic tool path (see Figure 5.34) is given in Table 5.13 with figure insets 8(a) – 8(d).

Initial design	Optimum compromised design
$\mathbf{X}^0 = [0.4, 0.4, -0.4, -0.4, 0.2]^T$	$\mathbf{X}^* = [0.28698, 0.27183, -0.40319, -0.25524, 0.13241]^T$
Inequality constraint values (see Section D.3):	
$C_1(\mathbf{X}^0) = -0.05$ $C_2(\mathbf{X}^0) = -0.3$ $C_3(\mathbf{X}^0) = -0.065$ $C_4(\mathbf{X}^0) = -0.287$ $C_5(\mathbf{X}^0) = -0.07$ $C_6(\mathbf{X}^0) = -0.087$ $\rightarrow C_7(\mathbf{X}^0) = 0.10390$ $C_8(\mathbf{X}^0) = -0.02582$ $C_9(\mathbf{X}^0) = -0.00651$ $\rightarrow C_{10}(\mathbf{X}^0) = 0.00321$ $\rightarrow C_{11}(\mathbf{X}^0) = 0.00321$ $C_{12}(\mathbf{X}^0) = -0.32872$ $C_{13}(\mathbf{X}^0) = -0.12872$ $C_{14}(\mathbf{X}^0) = -0.03807$ $C_{15}(\mathbf{X}^0) = -0.05491$ $C_{16}(\mathbf{X}^0) = -0.00827$ $C_{17}(\mathbf{X}^0) = -0.01806$ $C_{18}(\mathbf{X}^0) = -0.00218$ $C_{19}(\mathbf{X}^0) = -0.07006$ $C_{20}(\mathbf{X}^0) = -0.09382$ $C_{21}(\mathbf{X}^0) = -0.08689$ $C_{22}(\mathbf{X}^0) = -0.01093$ \rightarrow constraint violation	$C_1(\mathbf{X}^*) = -0.16302$ $C_2(\mathbf{X}^*) = -0.18698$ $C_3(\mathbf{X}^*) = -0.19317$ $C_4(\mathbf{X}^*) = -0.15883$ $C_5(\mathbf{X}^*) = -0.13759$ $C_6(\mathbf{X}^*) = -0.01941$ $\Rightarrow C_7(\mathbf{X}^*) = 0.375 \times 10^{-4}$ $C_8(\mathbf{X}^*) = -0.05909$ $C_9(\mathbf{X}^*) = -0.04699$ $\Rightarrow C_{10}(\mathbf{X}^*) = 0.158 \times 10^{-4}$ $\Rightarrow C_{11}(\mathbf{X}^*) = 0.158 \times 10^{-4}$ $C_{12}(\mathbf{X}^*) = -0.34499$ $C_{13}(\mathbf{X}^*) = -0.17817$ $C_{14}(\mathbf{X}^*) = -0.05417$ $C_{15}(\mathbf{X}^*) = -0.17787$ $C_{16}(\mathbf{X}^*) = -0.02705$ $C_{17}(\mathbf{X}^*) = -0.00307$ $\Rightarrow C_{18}(\mathbf{X}^*) = 0.108 \times 10^{-3}$ $C_{19}(\mathbf{X}^*) = -0.06970$ $C_{20}(\mathbf{X}^*) = -0.15416$ $C_{21}(\mathbf{X}^*) = -0.03715$ $C_{22}(\mathbf{X}^*) = -0.07894$ \Rightarrow constraint active
Variation of actuator leg lengths along segment (a) of the bigger parabolic tool path (see Figure 5.34):	
	
8(a)	8(b)

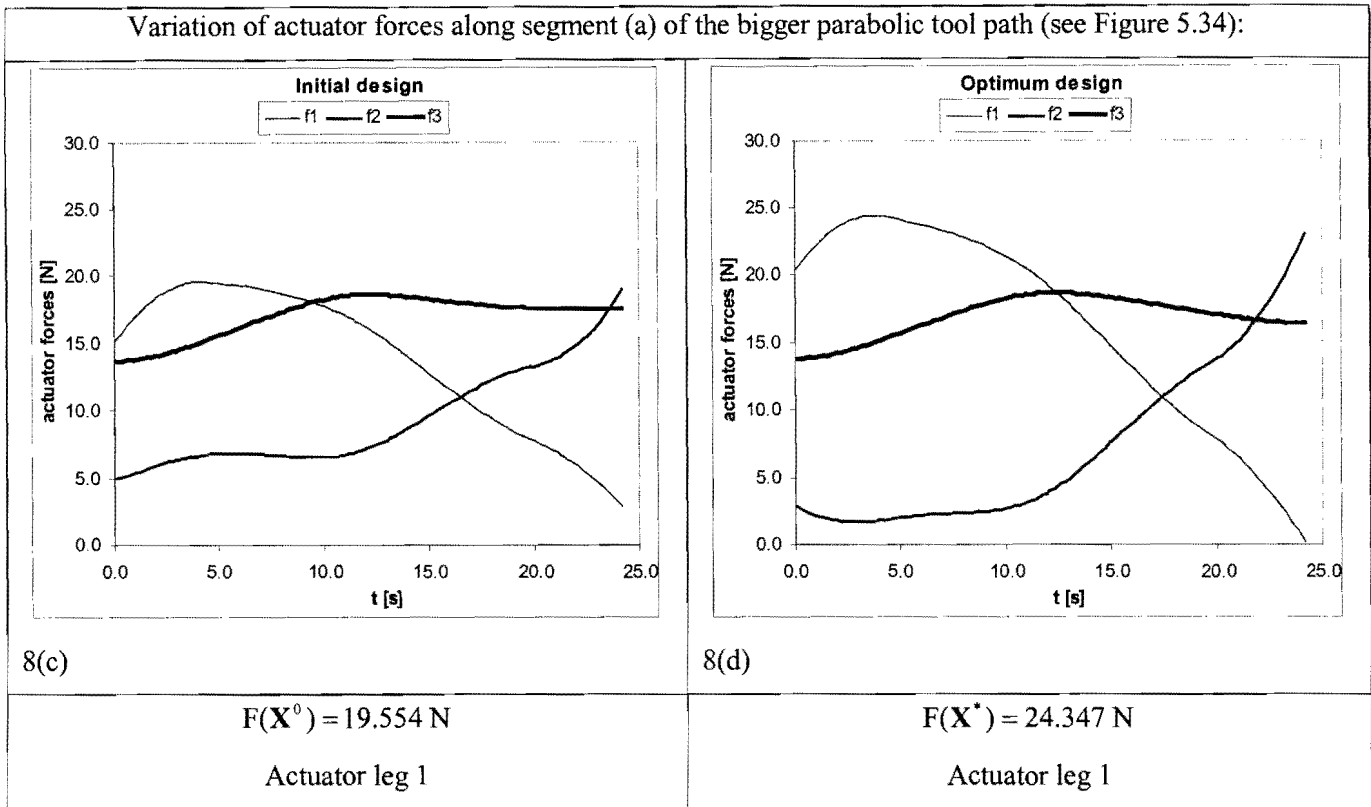


Table 5.13: Comparison between the initial and optimum designs for segment (a) of the bigger parabolic tool path (see Figure 5.34).

To start off with, the initial design \mathbf{X}^0 is again infeasible as can be seen from the positive inequality constraint function values $C_7(\mathbf{X}^0)$, $C_{10}(\mathbf{X}^0)$ and $C_{11}(\mathbf{X}^0)$ in Table 5.13. Figure inset 8(a) also shows that actuator leg ℓ_1 violates the maximum allowable actuator leg length (inequality constraint C_7) as segment (a) of the bigger parabolic tool path (see Figure 5.34) is traced with the initial design. The lower frame boundary inequality constraints C_{10} and C_{11} (expression (D.12)) are also slightly violated by the initial design.

For the feasible optimum design \mathbf{X}^* , the active inequality constraints corresponding to C_7 , C_{10} , C_{11} and C_{18} (see Table 5.13) exhibit a behavior similar to that detected for the circular tool path of Section 5.4, and explained in detail with reference to Table 5.6. The LFOPC-optimization terminated on criterion 2 ($\epsilon_x \leq 10^{-5}$) listed in Section 4.4 after 144 optimization iterations requiring 3 minutes and 40 seconds computational time on a Pentium IV 1.5 GHz computer with 640 MB DDRAM.

The optimum variation of the actuator forces along segment (a) of the bigger parabolic tool path shown in figure inset 8(d) is fairly similar to the initial variation shown in figure inset 8(c). In particular, the

initial objective function value is $F(\mathbf{X}^0) = 19.554 \text{ N}$ in actuator leg ℓ_1 , while the optimum objective function value is $F(\mathbf{X}^*) = 24.347 \text{ N}$, also in actuator leg ℓ_1 .

The convergence histories of the objective function (Figure 5.39) and design variables (Figure 5.40) are shown below. Note that both these graphs indicate that in this case, effective convergence is only reached after only 120 iterations.

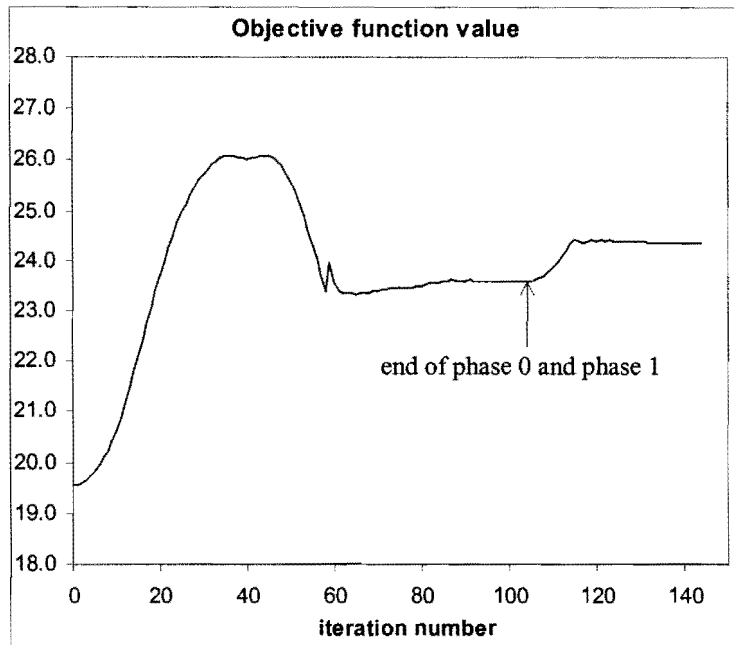


Figure 5.39: Convergence history of the objective function for segment (a) of the bigger parabolic tool path (see Figure 5.34).

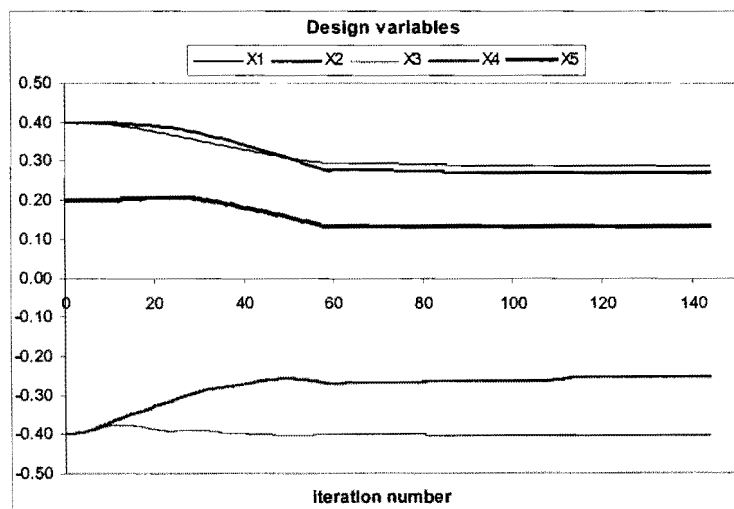


Figure 5.40: Convergence histories of design variables X_i , $i = 1, 2, \dots, 5$ for segment (a) of the bigger parabolic tool path (see Figure 5.34).

5.7.3 Execution of the prescribed bigger parabolic tool path

5.7.3.1 First execution of segment (b) (see Figure 5.34)

The series of photographs grouped in Figure 5.41 shows the initial and final time instants during the *first* (“upward”) execution of segment (b) of the prescribed bigger parabolic curve (see Figure 5.34). The tangential orientation of the moving platform is clearly visible from these photographs.

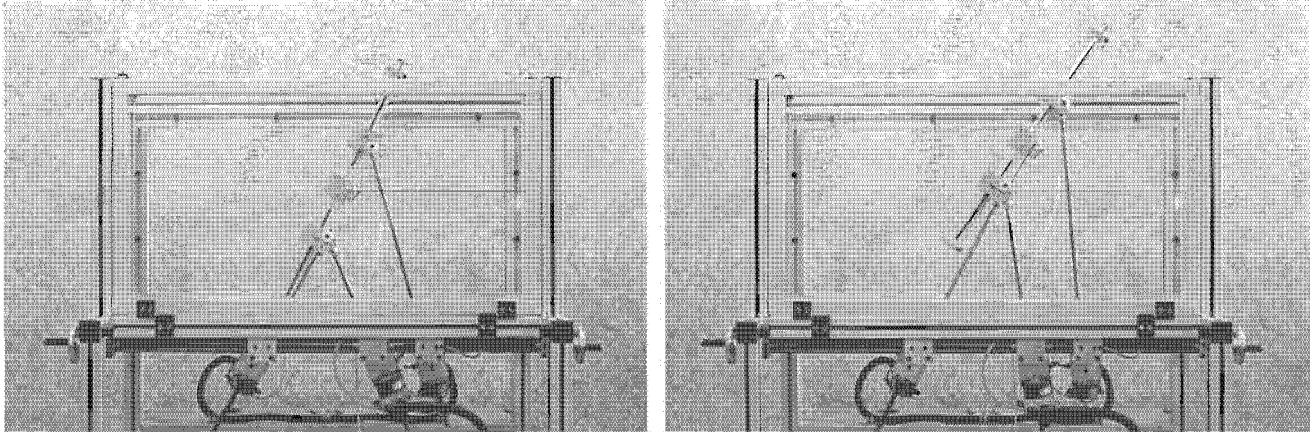


Figure 5.41: First execution of segment (b) of the bigger parabolic tool path (see Figure 5.34).

A close-up view of the executed segment (including a horizontal reference base-line) is shown in Figure 5.42.

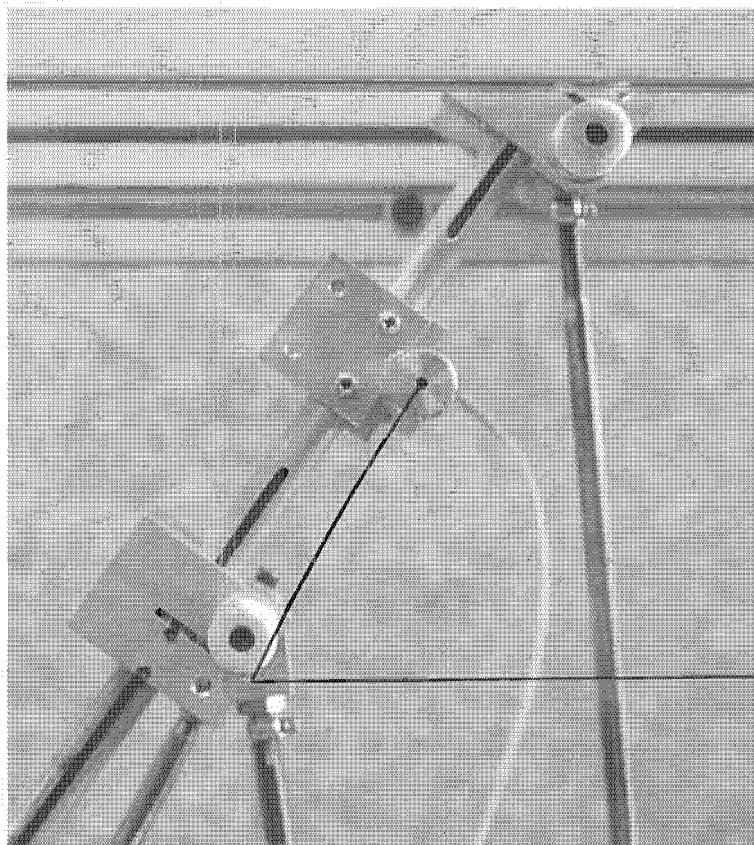


Figure 5.42: Close-up view of the executed segment (b) of the bigger parabolic tool path (see Figure 5.34).

5.7.3.2 Execution of segment (a) (see Figure 5.34)

Once segment (b) has been traced, the “workpiece” is repositioned as explained in Section 5.7.2.1. The series of photographs grouped in Figure 5.43 shows the positioning of the platform at different time instants during the execution of segment (a) of the prescribed bigger parabolic curve (see Figure 5.34). These photographs clearly show that the tangential orientation of the moving platform is maintained as segment (a) is traced.

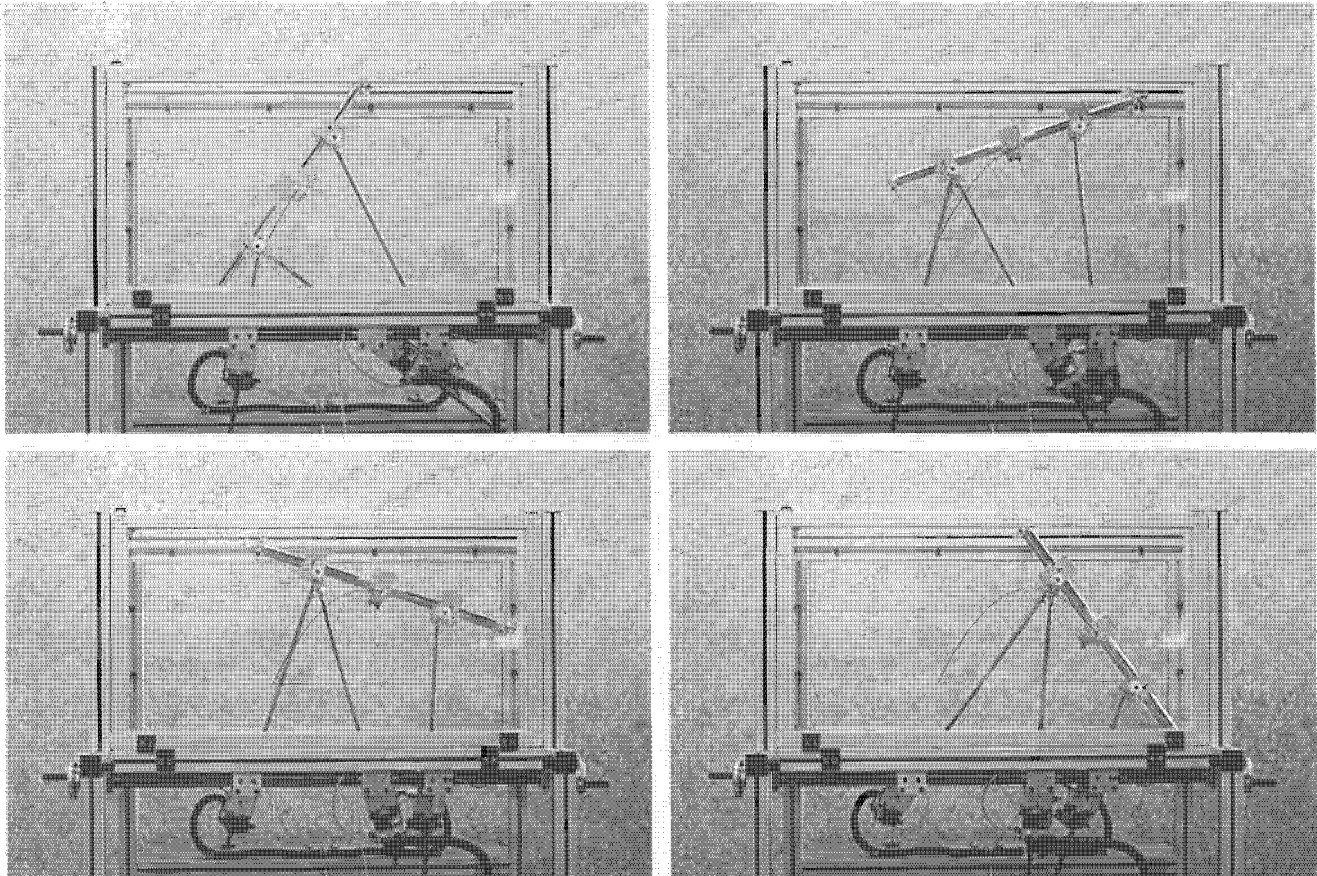


Figure 5.43: Execution of segment (a) of the bigger parabolic tool path (see Figure 5.34).

The close-up view of the executed segments (b) and (a) shown in Figure 5.44, emphasizes the smooth transition between consecutive segments.

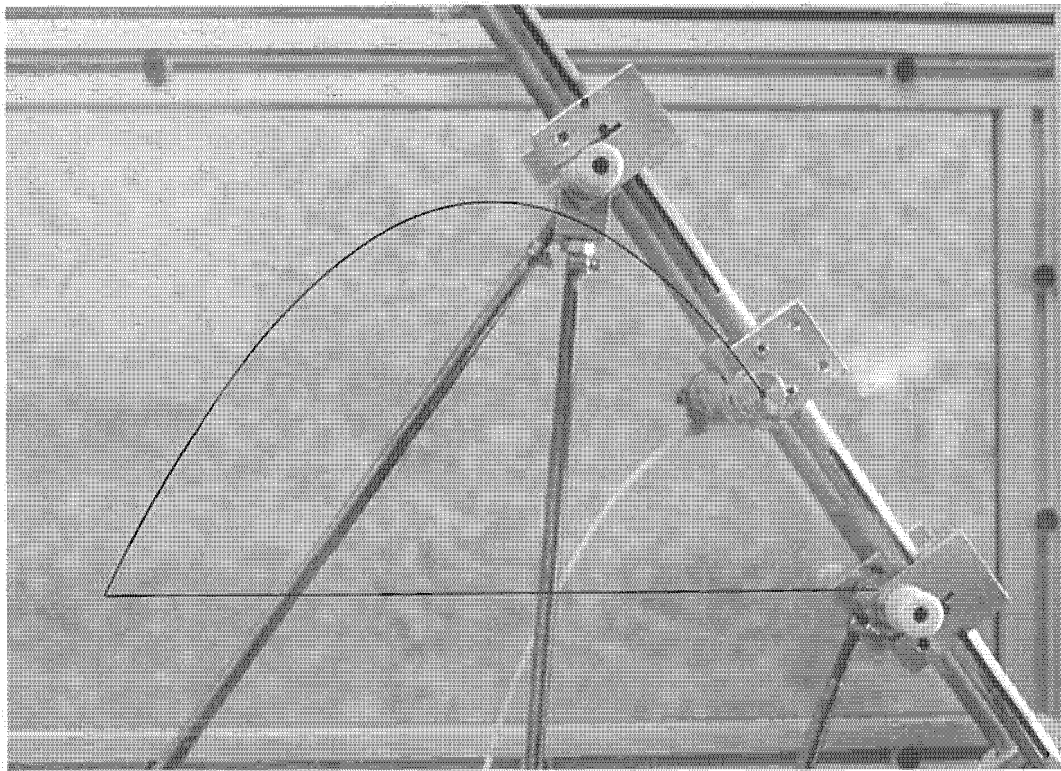


Figure 5.44: Close-up view of the executed segments (b) and (a) of the bigger parabolic tool path (see Figure 5.34).

5.7.3.3 Second execution of segment (b) (see Figure 5.34)

Corresponding to the second possible strategy for the piece-wise execution of the prescribed bigger parabolic tool path (see Section 5.7.2.1), the planar “workpiece” is now rotated through 180° about its vertical symmetry-axis, and repositioned so that segment (b) of Figure 5.34 can be traced for the second time, also “upwards”.

The series of photographs grouped in Figure 5.45 shows the initial and final time instants, as well as an intermediate time instant during the *second* execution of segment (b) (see Figure 5.34). The tangential orientation of the moving platform is again clearly visible from these photographs.

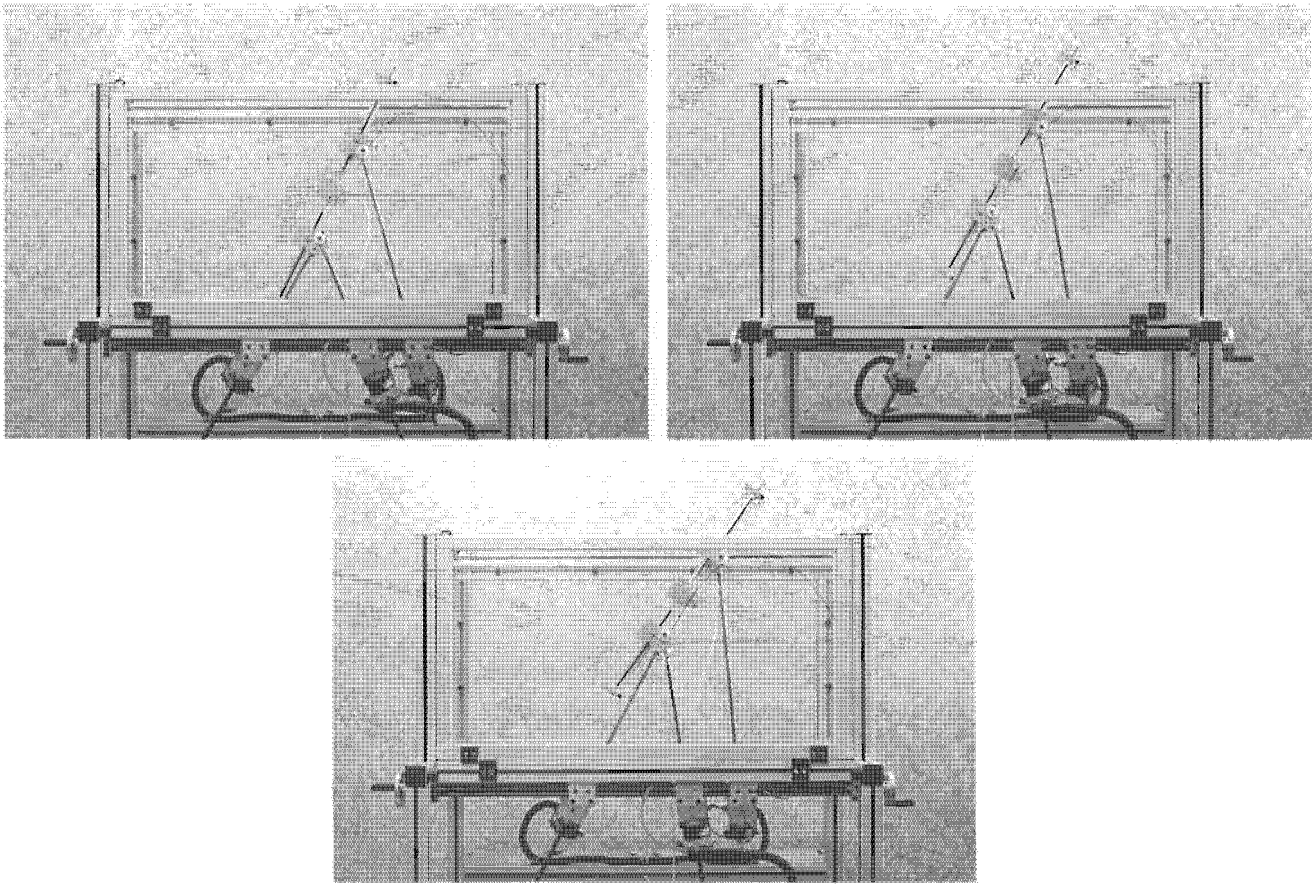


Figure 5.45: Second execution of segment (b) of the bigger parabolic tool path (see Figure 5.34).

A close-up view of the completely executed bigger parabolic tool path is shown in Figure 5.42. In spite of the piece-wise execution of this tool path, it is proportionally shaped and smooth, in agreement with the continuous prescribed tool path specified by Figure 5.30.

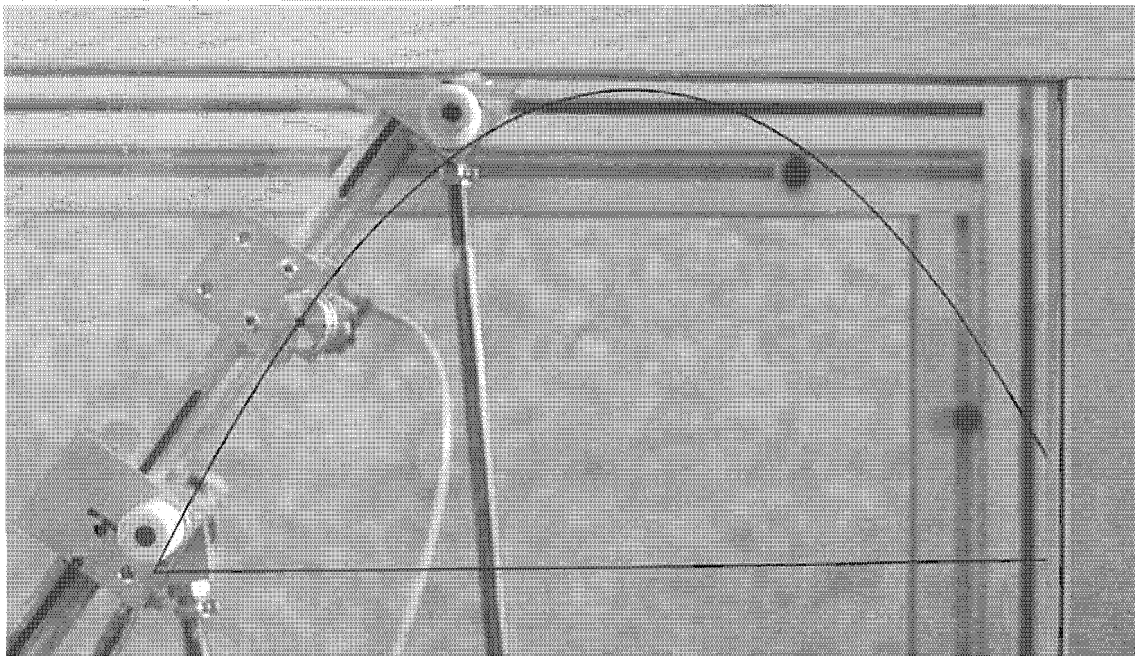


Figure 5.46: Close-up view of the completely executed bigger parabolic tool path (see Figure 5.30).

